The Pennsylvania State University

The Graduate School

REAXFF AND eREAXFF REACTIVE FORCE FIELD DEVELOPMENT AND APPLICATIONS TO ENERGY STORAGE INTERFACES

A Dissertation in

Mechanical Engineering

by

Md Jamil Hossain

Submitted in Partial Fulfillment
of the Requirements
for the Degree of

Doctor of Philosophy

December 2021

The dissertation of Md Jamil Hossain was reviewed and approved by the following:

Adri C. T. van Duin
Distinguished Professor of the Department of Mechanical Engineering
Dissertation Advisor
Chair of Committee

Chao-Yang Wang
Professor of the Department of Mechanical Engineering

Donghai Wang
Professor of the Department of Mechanical Engineering

Michael J. Janik
Professor of the Department of Chemical Engineering

Daniel Haworth
Professor of the Department of Mechanical Engineering
Associate Head for Graduate Programs of the Department of Mechanical Engineering

ABSTRACT

The depletion of fossil fuels necessitates alternate and clean energy sources. Lithium-ion batteries and solid oxide electrocatalysis devices are some of the most popular candidates. However, further improvements of these energy storage devices are essential in order to meet the ever-increasing global energy demand. Improvement of the performance of these high energy chemical systems is directly linked to the understanding and improving the complex physical and chemical phenomena and exchanges that take place at their different interfaces. Surfaces or interfaces, structures created between dissimilar media, such as liquids and solids, and interphases, structures arising in between these dissimilar media, present great challenges for their study and understanding since these are the regions where myriad events such as electron transfer, ion transfer and migration, reactions, and solvation/desolvation processes take place and significantly alter their landscape. In order to investigate the physical and chemical interactions at the interfaces of energy storage devices such as Li-ion batteries and solid oxide electrocatalysis devices, we used ReaxFF and eReaxFF reactive molecular dynamics simulations in the following research areas:

1) In the electrode/electrolyte interface of a typical lithium-ion battery a solid electrolyte interphase layer is formed as a result of electrolyte decomposition during the initial charge/discharge cycles. Electron leakage from anode to the electrolyte reduces the Li^+-ion and makes them more reactive resulting in decomposition of the organic electrolyte. To study the Li-electrolyte solvation, solvent exchange and subsequent solvent decomposition reactions at the anode/electrolyte interface, we have extended existing ReaxFF reactive force field parameter sets to organic electrolyte species such as ethylene carbonate, ethyl methyl carbonate, vinylene carbonate and $LiPF_6$ salt. Density Functional Theory (DFT) data describing Li-associated initiation reactions for the organic electrolytes and binding energies of Li-electrolyte solvation structures were generated and added to existing ReaxFF training data and subsequently, we trained the

ReaxFF parameters with the aim to find the optimal reproduction of the DFT data. In order to discern the characteristics of Li neutral and cation, we have introduced a second Li parameter set to describe Li^+-ion. ReaxFF is trained for Li-neutral and Li^+-cation to have similar solvation energies but unlike the neutral Li, Li^+ will not induce reactivity in the organic electrolyte. Solvent decomposition reactions are presumed to happen once Li^+-ions are reduced to Li-atoms, which can be simulated using a Monte-Carlo type atom modification within ReaxFF. This newly developed force field is capable of distinguishing between a Li-atom and a Li^+-ion properly. Moreover, it is found that the solvent decomposition reaction barrier is a function of the number of EC molecules solvating the Li-atom.

2) Graphene, a 2D material arranged in an sp^2-bonded hexagonal network, is one of the most promising materials for lithium-ion battery anodes due to its superior electronic conductivity, high surface area for lithium intercalation, fast ionic diffusivity and enhanced specific capacity. A detailed atomistic modeling of electronic conduction and non-zero voltage simulations of graphitic materials require the inclusion of an explicit electronic degree of freedom. To enable large length and time scale simulations of electron conduction in graphitic anodes, we developed an eReaxFF force field describing graphitic materials with an explicit electron concept. The newly developed force field, verified against quantum chemistry-based data describing, amongst others, electron affinities and equation of states, reasonably reproduces the behavior of electron conductivity in pristine and imperfect graphitic materials at different applied temperatures and voltages. Our eReaxFF description is capable of simulating leakage of excess electrons from graphene which are captured by exposed lithium ions; a common behavior at the anode/electrolyte interface of a lithium-ion battery. Finally, the initiation of Li-metal-plating observed at the graphene surface reveals the eReaxFF force field's potential for the future development of Li-graphene interactions with explicit electrons.

3) Electrocatalysis results in the change of the rate of an electrochemical reaction occurring on an electrode surface by varying the electrical potential. Electrocatalysis can be used in hydrogen generation and the generated hydrogen can be stored for future use in fuel cells for clean electricity. The use of solid oxide in electrocatalysis specially in hydrogen evolution reaction is promising. To enable large length and time scale atomistic simulations of solid oxide electrocatalysis for hydrogen generation, we developed an eReaxFF force field for barium zirconate doped with 20 mol% of yttrium (BZY20). All parameters for the eReaxFF were optimized to reproduce quantum mechanical (QM) calculations on relevant condensed phase and cluster systems describing oxygen vacancies, vacancy migrations, water adsorption, water splitting and hydrogen generation on the surfaces of the BZY20 solid oxide. Using the developed force field, we performed zero-voltage molecular dynamics simulations to observe water adsorption and the eventual hydrogen production. Based on our simulation results, we conclude that this force field sets a stage for the introduction of explicit electron concept in order to simulate electron conductivity and non-zero voltage effects on hydrogen generation.

Overall, the work described in this dissertation demonstrate how atomistic-scale simulations can enhance our understanding of processes at interfaces in energy storage materials.

TABLE OF CONTENTS

LIST OF FIGURES

LIST OF TABLES

ACKNOWLEDGEMENTS

I am indebted to so many for their support and guidance throughout this long and laborious journey to a Ph.D. First, I would like to extend my deepest heartfelt thanks to my advisor, Dr. Adri van Duin. Needless to say, his constant support, inspiration and remarkable scientific input throughout the course of this research work were invaluable. Working with him has always been an honor and pleasure for me. I am thankful for his kind patience over the period and for putting his trust on me when it was most needed.

I would like to thank my Ph.D. committee members Dr. Chao-Yang Wang, Dr. Donghai Wang and Dr. Mike Janik for their time and valuable insights to help augment the quality of this work. I also like to acknowledge my collaborators Dr. Oleg Borodin and Dr. Dmitri Bedrov and my funding agency the U.S. Army Research Laboratory (ARL) through the Collaborative Research Alliance (CRA) for Multi-Scale Multidisciplinary Modeling of Electronic Materials (MSME) for their continuous support during the course of my PhD. I gratefully thank my two-time intern mentor Dr. Gorakh Pawar from Idaho National Laboratory (INL) for his valuable insights and opportunities to engage in high quality research, during and post internship periods, that was funded through the INL Laboratory Directed Research & Development (LDRD) Program under the Department of Energy (DOE), Idaho. [Disclaimer: Any opinions, findings, and conclusions or recommendations expressed in this dissertation are those of the author's and do not necessarily reflect the views of the awarding agencies]. I would also like to thank Dr. Mitsunori Nakamoto, Dr. Wataru Sekine and Dr. Kikou Yamaguchi from MuRata Manufacturing Co., Ltd., Japan for their valuable research insights that helped my projects advance.

Additionally, I would like to thank my fellow group members for their countless helpful scientific discussions. In particular, I would like to thank Karthik Ganeshan for his guidance,

collaborations on the multiple work as well as encouragement during the past few years as a friend and colleague.

Most importantly, I wish to thank my wonderful wife, Umme Hani, who provided unending inspiration and unconditional support, without whom this journey would have been very difficult; I am glad to have her in my life. Finally, I would like to thank my siblings and parents for their endless care, love, prayers and inspiration.

Chapter 1

Introduction

Sustainable energy is essential to human societies. Currently, the major source of energy is fossil fuels. As world population continues to grow and the amount of fossil fuels begins to diminish, it may not be possible to provide the amount of energy demanded by the human population by only using fossil fuels to generate energy. Moreover, energy extraction from carbon-burning has a detrimental impact on the environment. It has long been discussed that the ascent of batteries, electrocatalysis devices and similar energy storage devices would mark the beginning of the end of the fossil-fuel age. Batteries, once relegated to powering small devices like remote controls and watches, are now poised to energize the things most central to daily life, from smartphones to cars to entire homes and offices. The shortcomings of the current state of technology in batteries have restricted their applications to small scale. Batteries with higher energy density, enhanced safety and longer cycling life than the existing lithium-ion technology are essential for large-scale applications. As the availability of renewable electricity increases, electrochemical devices, such as fuel cells and electrocatalysis devices, can help facilitate conversion between electrical and chemical forms, allowing for storage of electrical energy in chemical form, or electricity-driven conversions to generate useful chemical compounds.

Battery

A battery is an electrochemical device that transforms stored chemical energy into electrical energy and used as a power source. It is built up of electrochemical cells which consists of a positive (cathode) and a negative (anode) electrode, separated by an electrolyte solution (an

ionic conductor which is also an electronically insulating medium) containing dissociated salts [1]. The electrical energy stored in a battery is the product of capacity and voltage and is determined by the cell electrochemistry and electrode material properties [2]. Their energy density is governed primarily by the active mass in the electrodes of the device, whereas the power density is governed by the rate of the redox reactions and the strength of diffusion within the electrolyte. Key components of a typical battery are shown in Figure **1-1**. During discharging, electrons are released from the anode and flow towards the cathode through the external circuit, while at the same time, ion transport across the electrolyte from the anode to the cathode ensures electro-neutrality. In general, batteries are classified into two broad categories: primary batteries that irreversibly transform chemical energy to electrical energy, which are used once and disposed, and secondary batteries are rechargeable and can be used multiple times.

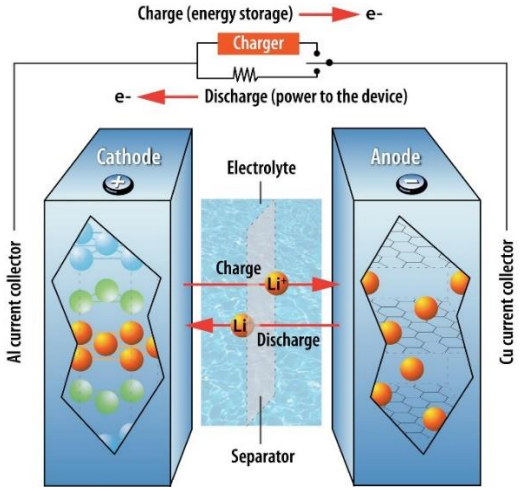

Figure **1-1**: Schematic of the components of a Li rechargeable battery. (cdn.arstechnica.net/wp-content/uploads/2021/05/argonne_national_lab_battery_diagram.jpg)

History of Rechargeable Batteries

The earliest commercial non-rechargeable lithium batteries were introduced in the 1970s with a 3V lithium metal as an anode [3]. Li metal was favored as an anode material because it is

the most electropositive (–3.04 V versus standard hydrogen electrode), lightest (equivalent weight=6.94 $gmol^{-1}$, and specific gravity =0.53 gcm^{-3}) metal. In 1972, Whittingham at Exxon launched a rechargeable battery project using layered TiS_2 and Li metal as a positive, and a negative electrode, respectively, and lithium perchlorate in dioxolane as electrolytes. Despite a superior performance of the layered cathode material, the battery encountered severe shortcomings from a Li-metal/liquid electrolyte combination because of the deleterious Li-dendrite growth at the lithium metal anode during electrodeposition, which led to the hazard of catastrophic fire [3]. A breakthrough in the Li-battery technology has been achieved in the late 1970s with the discovery of a passivating layer at the anode-electrolyte interface. When Li- metal comes in contact with the organic solvents, it forms a thin film, which is a primary reason for the stability of the batteries. In 1979, Peled [4] coined the term 'Solid Electrolyte Interphase' (SEI) and emphasized that the rate limiting step is the migration of lithium ions through this interfacial film. To overcome the issues of dendrite growth and safety hazard, alternate approaches for the negative electrode were investigated and which led to various other types of secondary batteries.

In the mid-1980s NiCd secondary batteries became widespread, and they began to supplant earlier generation primary and Li-metal based batteries for small electric appliances [5]. However, due to the detrimental impact of Cadmium on the environment, NiMH secondary batteries were gradually favored over NiCd batteries in the late 1980s. Over the same period, extensive research efforts performed by Goodenough et al. [6] on layered cathode materials (Li_xMO_2, where M is Co, Ni, or Mn) and Scrosati et al. [7], Murphy et al. [8] on insertion anode materials laid the foundation of modern Li-ion batteries. Finally, in June 1991, Sony Corporation commercialized the first modern $C/LiCoO_2$ Li-ion cell by exploiting the developed technology for the high-performance layered cathode material and the highly reversible, low voltage Li intercalation–deintercalation based carbonaceous material [3]. Since then, compact and lightweight Li-ion batteries have been ubiquitously used in consumer electronics such as mobile phones, cameras, and laptop computers

[9]. A comparison of the energy densities of commonly available rechargeable batteries is shown in Figure **1-2**. Battery technologies beyond the Li-ion batteries, for example, Na-ion, Li-air, and Zn-air are also being considered as potential candidates to meet the demand of future energy storage.

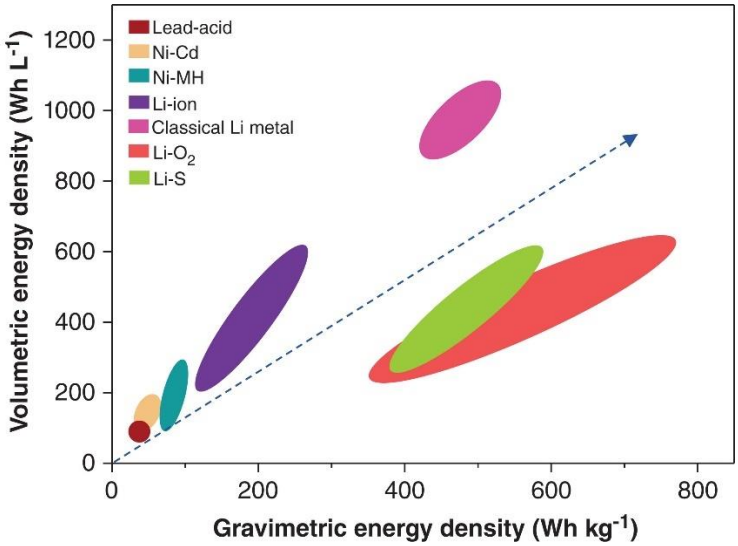

Figure **1-2**: Comparison of various rechargeable battery technologies in terms of volumetric and gravimetric energy density [10].

Li-ion Batteries

The advancement in the Li-ion batteries achieved in the last two decades allowed their large-scale applications, such as electrification of transportation, micro grids for storing electricity generated from various renewable energy sources. The novel characteristics of the Li-metal such as (i) the lowest reduction potential of any elements yields the highest cell potential, (ii) the lightest metal available in the periodic table, enables high gravimetric and volumetric capacities for Li-based batteries. A typical commercial Li-ion battery is comprised of a transition metal oxide cathode, a graphitic anode, and carbonate-based electrolytes. The electrochemical reactions in Li-ion batteries are based on the intercalation and deintercalation of Li ions, in which Li ions move

from the anode to the cathode during the discharge process and come back during the charge process. Figure **1-3** represents a schematic of a Li-ion battery system. Different subsystems of a Li-ion battery are briefly described in the following sections.

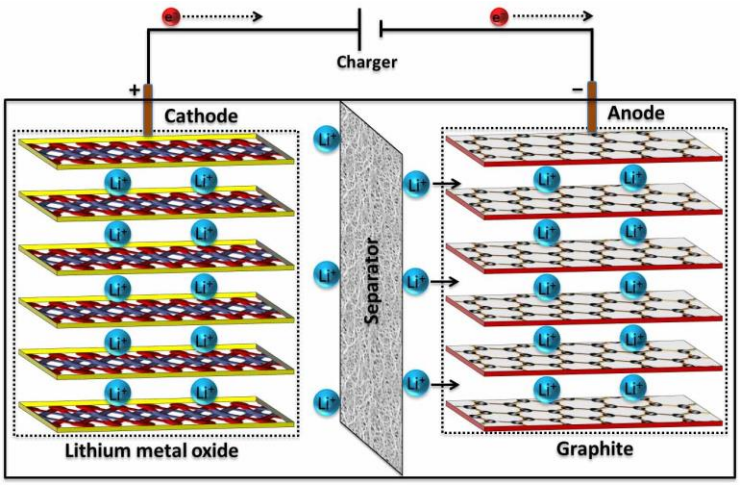

Figure **1-3**: Schematic of a Li-ion battery system.
(https://engineering.purdue.edu/ViPER/pics/res/Li_1.jpg)

Anode Materials

Li-ion batteries were designed, initially, using Li-metal anodes. However, the usage of Li-metal was ceased rapidly because of the safety concerns. The carbon-based materials are the most ubiquitously used anode materials for the commercial Li-ion batteries. The process of Li-intercalation and deintercalation into graphitic material maintains its two dimensional (2D) mechanical stability. Carbon possesses attractive properties of low cost, abundance in nature and low de-lithiation potential vs. Li, and high Li diffusivity [11]. In the graphite anode, 1 Li atom per 6 carbon atoms can be stored, which results in a theoretical capacity of 372 $mAhg^{-1}$. During Li intercalation, graphite undergoes around 10% increase in its interlayer spacing. Such a volume change may cause a fracture in the anode-SEI, thus degrades cell performance.

Graphene, a two-dimensional sp^2-carbon based material, has attracted a very high level of attention since its successful isolation in 2004 [12], [13]. Graphene's high electrical conductivity and its electrochemical properties like large reversible specific capacity, high rate capability and cyclability makes it promising for use in energy storage applications such as lithium ion batteries [14]–[16]. Though many studies have focused on its electronic properties, graphene also has exciting mechanical properties, such as an exceptionally high tensile strength (130 GPa) and Young's modulus (1 TPa) [17], [18]. Furthermore, novel electronic states can be realized in graphene by mechanical manipulation, granting it a versatility not possible in traditional materials [19]. In particular, studies have shown that rippled and wrinkled graphene has enhanced energy storage capabilities [18] as stretching of the C-C bonds due to corrugations changes the electronic structure and transport properties.

Cathode Materials

Intercalation materials exhibit a wide variety of thermodynamic and kinetic properties depending on their crystal structures, host chemistries, etc. and are the most widely used cathode materials in Li-ion batteries. Intercalation is a process where guest atoms can be inserted into and removed from the host material reversibly without a change in the crystal structure. The intercalation compounds can be divided into several categories based on their crystal structures, such as layered, olivine, spinel and tavorite. The layered structures are the earliest and the most popular form of intercalation compounds for the cathode materials. Layered $LiCoO_2$ (LCO), with an R3m rhombohedral structure, has been widely used in Li-ion batteries over the last two decades, because of its relatively high theoretical specific capacity of 274 $mAhg^{-1}$, high theoretical volumetric capacity of 1363 mAh cm^{-3}, high discharge voltage, and good cycling performance [20]. LCO also possesses a number of shortcomings, including high cost, low thermal stability, and rapid

capacity fade at a high discharge rate. The higher discharge rate induces crystal distortion from the hexagonal to monoclinic symmetry leading to performance deterioration.

$LiMnO_2$ (LMO) has been studied as a potential alternative to the LCO cathode owing to its relatively lower cost and lesser toxicity. However, the application of LMO cathode has been plagued because of (i) during Li-extraction the layered structure has a tendency to convert into spinel structure and (ii) dissolution of Mn into the electrolyte solvents causes loss of Mn. Mn_2^+ is soluble in electrolytes and degrades anode SEI stability. The orthorhombic LMO with a rock salt crystal structure has a capacity of 274 $mAhg^{-1}$ in the voltage range of 2.0-4.5 V [21]. Crystal structures of the various cathode materials are shown in Figure **1-4**.

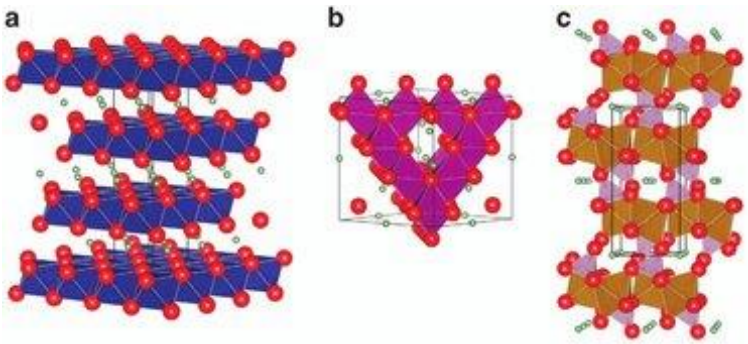

Figure **1-4**: Crystal structures of representative intercalation cathodes: structure of (a) layered ($LiCoO_2$), (b) spinel ($LiMn_2O_4$), (c) olivine ($LiFePO_4$) [22]

The three-component Ni-Co-Mn system $Li[Ni_xCo_xMn_x]O_2$ (NCM) demonstrates excellent electrochemical properties because of the synergetic contributions from the stable electrochemical characteristics of $LiCoO_2$, high capacity of $LiNiO_2$ and the thermal stability and low cost of manganese in $LiMnO_2$. The $LiNi_{1/3}Co_{1/3}Mn_{1/3}O_2$ is the common form of NCM and is widely used in Li-ion batteries. It exhibits superior charge/discharge characteristics that can produce batteries with a long life and enhanced safety. Although this material has a capacity similar to the $LiCoO_2$, this combination is promising because of minimal volume change during charging-discharging, good performance, safety, and lower cost [21].

$LiMn_2O_4$ (LMO) is a representative spinel cathode material. The LMO has received attention due to the benefits of a reduced cost, availability, and environmental friendliness of Mn. However, the long-term cyclability of LMO is hindered because of the irreversible side reactions with electrolytes, oxygen loss from the de-lithiated LMO, Mn dissolution, and phase transformation to the tetragonal $Li_2Mn_2O_4$ at the surface [23]–[26]. The dissolution problem can be suppressed with a surface coating of ZnO [27], metal doping [28], Mn-rich layered coating, and by forming a stable SEI [29].

$LiFePO_4$ (LFP) has an olivine-type of structure with a symmetry group of Pmnb. Iron is one of the most abundant metal in the earth crust, cheaper and more environmentally friendly than cobalt. LFP is known for its thermal and chemical stability and high power capability. The gravimetric and volumetric capacity of LFP is 170 mAh g^{-1}, and 589 mAh cm^{-3}, respectively [11]. The disadvantage of the LFP is a low electronic conductivity and slow diffusion of Li-ions, and a relatively low average voltage of 3.4 V. The lower ionic and electronic conductivity can be improved by reducing LFP particle size and coating with various conducting agents such as carbon or silver nanoparticles. The lower operating cell potential is advantageous to prevent electrolyte decomposition, thus maintains high energy density and stable cycling. The charging (delithiation) reduces the volume of LFP by approximately 6.8%, which is compatible with the increase in the volume of the graphitic anode material [21]. The capacity of the available cathode and anode materials is shown in Figure **1-5**.

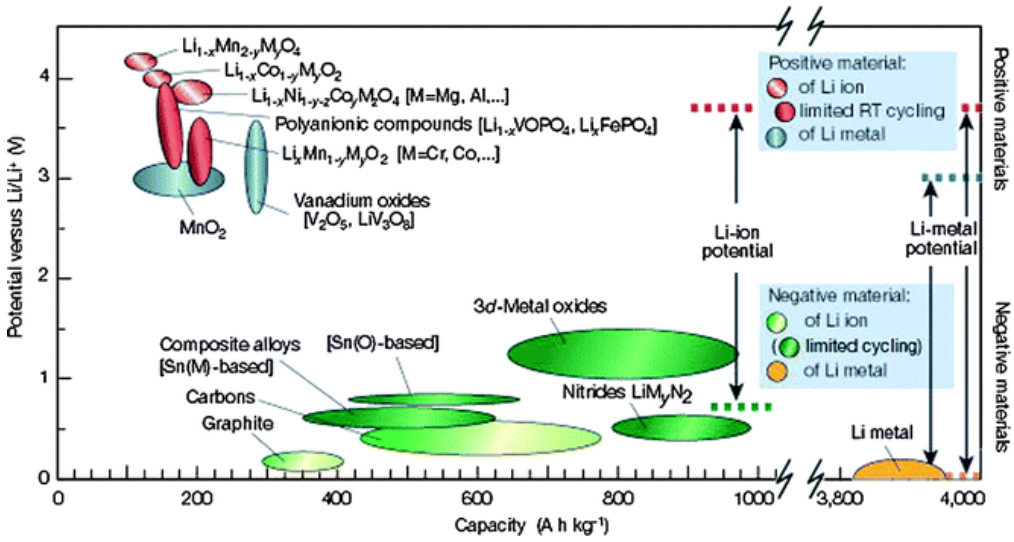

Figure **1-5**: Capacity and the operating potential of various electrode materials [30].

Electrolytes

The electrolyte of a Li-ion battery serves as a medium to transport positively charged ions between the cathode and anode terminals. Typical compositions of Li-ion battery electrolytes are based on the mixture of two or more organic solvents and solutions of one or more lithium salts. The mixed solvent formulation is required because of the diverse and often contradicting requirements of the electrolyte properties which can hardly be satisfied by any individual compound, for example, high dielectric constant versus high fluidity. Therefore, to obtain various properties simultaneously, solvents of very different physical and chemical natures are often used together. [31] The proper mixture can influence the overall performance of the Li-ion battery. A suitable electrolyte should have characteristics of good ionic conductivity, high chemical stability, low cost, and safety. Solvents with low melting point, high boiling point, low vapor pressure, low viscosity, and ability to dissolve salts to sufficient concentration are highly desirable for an efficient performance of a Li-ion cell. [32]

The most commonly used electrolytes are a mixture of one or more alkyl carbonates, such

as ethylene, dimethyl, diethyl, and ethyl methyl carbonates (EC, DMC, DEC, EMC, respectively), and $LiPF_6$ salt [33]–[36]. The alkyl carbonate solvents are chosen for their high oxidative/reductive stability at the operating potential of the transition metal oxide cathode, as well as graphitic anode. They also possess other properties, such as high polarity, a reasonable operating temperature range, low toxicity, and adequate safety features [36]. Especially, EC has an excellent dielectric property, its dielectric constant (ε =89) is even higher than water (~ε=79). However, a relatively high melting point of EC (~36 ºC) makes it unfavorable as a room temperature electrolyte solvent. Linear carbonates (such as DMC) differ from their cyclic cousins by their low melting points, low viscosity, and low dielectric constant. However, their ability to form homogeneous mixtures with EC at any ratio makes them an excellent co-solvent to be used with the EC to obtain the desirable properties of low-melting-temperature, low viscosity, and higher ionic conductivity.

The anion in the salt can participate in electrolyte reduction reactions and impact the SEI formation. A recent DFT study [37] showed that anion PF_6^- − reduction in the presence of LiF, formed due to anion defluorination, occurs at much higher potentials than the reduction of EC, DMC, and PC. Interestingly, $LiBF_4$ reduction occurs at much lower potentials than EC, DMC, and PC. This is supported by the experimentally measured reduction potential, which is 1.7 V and 0.8 V for $LiPF_6^-$ and $LiBF_4^-$ based electrolytes (EC/ EMC mixture), respectively [37]. Therefore, $LiPF_6$ influences the passivation layer formation more significantly than $LiBF_4$. In this example, the DFT calculations provided important insight into the reasons behind different SEI composition in $LiPF_6^-$ and $LiBF_4^-$ based electrolytes [37].

Ionic liquid based electrolytes have received attention in recent years due to their negligible vapor pressure, excellent thermal and electrochemical stability, dissolution with many organic and inorganic compounds, and low flammability [38]. For high voltage spinel cathodes, tetramethylene sulfone (TMS or sulfolane)-based electrolytes were reported to have a high oxidative stability and a good cycling ability [39].

Working Principles of a Li-ion Battery

The operating mechanism of a Li-ion battery can be explained as follows: during battery charging, transition metal oxide based cathode material oxidizes, for example, in $LiCoO_2$, the oxidation number of Cobalt increases from +3 to +4, and releases Li^+. The Li^+ transports through the electrolyte towards the graphitic anode. In the anode, in the presence of superfluous electrons, Li^+ ions get reduced and intercalates into the graphite layer as a Li-metal. The discharging process operates in an opposite way. When battery electrodes are connected through an external circuit, Li atom in the anode oxidizes to give up its electron and convert to Li^+. The electron flows through the outer circuits and arrives at the cathode. The Li^+ again diffuses back to the cathode, where it gets reduced, and transition metal restores its oxidation state, as such the oxidation number of Cobalt in $LiCoO_2$ decreases from +4 to +3.

Solid Electrolyte Interphase

During the initial charge/discharge cycles of Li-ion batteries, anodic reduction of the electrolytes creates a complex thin passivation layer consisting different organic and inorganic compounds which prevents decomposition of the electrolytes in the subsequent cycles. It also leads to the irreversible loss of Li, therefore, detrimentally affect the capacity of the battery [40]. In an ideal case, this layer has an electron transference number, t_e=0, and high ionic conductivity so that during battery operation, lithium ions can easily migrate through the layer to intercalate into and deintercalate from the graphitic anode. This essential passivation layer was named as a Solid Electrolyte Interphase (SEI) layer by Peled [4]. The properties of the SEI layer significantly affect the Li-ion batteries cycling ability, lifetime, capacity retention, high power density, rate capability, and safety [31], [41], [42]. The SEI should have an excellent mechanical strength and flexibility so

that it allows the expansion and contraction of the graphite lattice during the reversible intercalation/deintercalation process. The lower solubility of the SEI to the electrolytes is desirable to limit continuous consumption of the lithium. The SEI formation is significantly contingent upon the organic solvents used in a battery. For example, SEI is formed in an EC solvent, however, no such layer has been observed when propylene carbonate (PC) is used unless suitable additives like vinylene carbonates (VC) are added in it. At an overcharged condition, SEI formation is also possible at the cathode-electrolyte interface due to the cathodic oxidation of the electrolytes [43].

Given the high technological importance, extensive research efforts have been devoted to study the SEI formation mechanism as well as its chemical compositions using a wide variety of advanced computational and experimental techniques, but detailed chemistry remains elusive [3], [44]. Major difficulty in studying the SEI is the lack of computational facilities to meet the required length and time scale for molecular modeling and devoid of proper in-situ characterization techniques [45] while the battery is in operation.

During battery cycling, electrolyte reduction and oxidation occur at the anode and cathode surfaces, respectively. In the current Li-ion battery technology, cathode materials operate at an average potential of 4V versus Li/Li^+, while commonly used electrolytes reduction and oxidation potentials are below 2V and around 6V, respectively [21]. Thus, anodic reduction of the electrolytes causes SEI formation at the anode-electrolyte interfaces. However, application of high voltage cathodes invoke oxidative decomposition of electrolytes; therefore, SEI may form at the cathode-electrolyte interface as well [24], [26], [46]. Numerous mechanisms have been proposed in literature for explaining the intricate chemistry of the SEI formation. Besenhard et al. [47], [48] proposed that an electrolyte solvent can co-intercalate into the graphitic anode to form a graphitic intercalation compound, and the decomposition products determine further reaction behavior. Aurbach et al. [49] claimed that the initial surface film controls the nature of subsequent reactions.

However, a detailed mechanistic picture is still under debate. Understanding of the electrolyte decomposition reactions is the key aspect of studying the SEI formation mechanism.

Electrocatalysis Device

Electrocatalysis is a type of catalysis that results in the change of the rate of an electrochemical reaction occurring on an electrode surface by varying the electrical potential. Electrocatalytic processes occur at both fuel cells and electrolysis devices. To face the depletion of fossil fuels and the reduction of the greenhouse gas emission, decarbonized hydrogen production pathways based on renewable energy sources (i.e., wind energy, photovoltaic energy, hydro energy) and water electrolysis are considered attractive and promising solutions for a sustainable future [50], [51]. The water electrolysis process consists of employing electricity generated from renewable energy sources to split pure water into oxygen and hydrogen [52]. Other applications of electrocatalysis include but are not limited to CO_2 to CO or hydrocarbon conversion, nitrate and nitrogen or ammonia conversion etc. [53]

Electrocatalysts can be composed of materials ranging from metals, metal oxides, carbonaceous materials etc. [54] Across the wide operating range of electrochemical devices, electrolytes can range from aqueous ionic solutions, ions dispersed in organic solvents, ionic liquids, ionic polymers, molten salts, solid acids, solid bases, oxygen-conducting solid oxides such as yttria-stabilized zirconia (YSZ) and proton-conducting yttrium-doped barium zirconate (BZY) solid oxide. In these pathways, generated and stored hydrogen can be employed for different applications such as transportation, energy storage, power-to-gas, and industry [50], [55].

Overview of this Work

The objective of this research is to explore interfacial physical and chemical phenomena in energy storage applications such Li-ion batteries and solid oxide electrocatalysis devices using reactive molecular dynamics (MD) simulations. Despite a significant amount of experimental effort, detailed mechanisms of the intricate interfacial chemistry have not been explored comprehensively. The atomistic simulations can effectively enlighten the issues pertinent to the battery chemistry and the change in electrode properties during battery cycling. Several DFT based ab-initio MD simulations for investigating electrolyte decompositions at the electrode/electrolyte interfaces have been reported in recent literature [56]–[62]. However, applications of the quantum chemistry (QC) based methods are extremely limited by the length and time-scale that are required to predict the complex processes occurring at the Li-battery interfaces. Therefore, largescale MD simulations are necessary to address the issues associated with the interfaces of Li-ion batteries. Reactive force field (RFF) based methods are computationally cheap and can simulate reactions, therefore providing an attractive alternative to QC methods. In general, RFF-based methods are several orders of magnitude faster than QC methods and can handle systems with bigger length and time scales which is essential for investigating battery systems. ReaxFF is a reactive force field method, capable of describing reactions in nanoseconds of simulation in a length scale of nanometers while retaining most of the accuracy of DFT methods [63]. ReaxFF has been proven to be useful to study battery systems [25], [64]. However, the absence of an explicit electronic degree of freedom limits the application of the ReaxFF method in describing interfacial redox reactions of Li-ion batteries. Therefore, a comprehensive investigation of the interfacial oxidation and reduction reactions associated with the electrolyte decomposition and the formation of SEI requires the eReaxFF method [65], which is capable of incorporating an explicit electron or hole description within the ReaxFF framework. Using eReaxFF molecular dynamics simulation Islam

et al. [66] captured the mechanism of the reduction of the EC molecule due to electron transfer from lithium, ring opening of ethylene carbonate (EC) to generate EC^{-}/Li^{+} radicals, and subsequent radical termination reactions. The eReaxFF method can be extended for the non-zero voltage simulations of solid oxide electrocatalysis.

In this work, we used the ReaxFF method in Li/ $LiPF_6$/ EC / EMC / VC system to simulate solid electrolyte interphase formation chemistry in the anode/electrolyte interface. We used two separate Li parameter set to distinguish between Li-neutral and Li-cation and their behavior concerning solvation, desolvation, solvent exchange and reactivity with electrolyte molecules. We developed an eReaxFF force field for the description of graphitic anodes and used this force field to simulate both zero and non-zero voltage simulations on pristine and imperfect graphitic materials. We developed an eReaxFF force field for Yttria doped barium zirconate (BZY20) electrocatalysis to study oxygen vacancy migrations, water adsorption, water splitting and hydrogen generation at different surfaces.

This dissertation is organized as follows: after a brief introduction to the current state of lithium batteries and electrocatalysis devices in Chapter 1, Chapter 2 provides a detailed description of the energy functional of the ReaxFF method and the fundamental concepts of the explicit electron description in the eReaxFF method. Chapter 3 describes an accelerated molecular dynamics method that combines and achieves further accelerations of parallel replica dynamics (PRD) and collective variable hyperdynamics (CVHD). Chapter 4 describes the development of a ReaxFF force field for Li/ $LiPF_6$/ EC / EMC / VC system with two sets of Li parameters for making a distinction between neutral Li and Li^{+} cation. eReaxFF Force field development for graphitic anode materials is detailed in Chapter 5. Chapter 6 describes the eReaxFF force field development for BZY20 solid oxide electrocatalysis. Finally, Chapter 7 summarizes the conclusions and the outlook for future directions.

Chapter 2

ReaxFF: Reactive Force Field Method and eReaxFF: Explicit Electron Description Within ReaxFF

Molecular dynamics (MD) simulation is a technique for computing the physical movements of interacting particles, generally atoms, over a period of time. In the force field based MD methods, this interaction between particles is governed by empirically constructed potentials known as "force fields" which accounts for interatomic forces. It is assumed that the nuclear motion of the constituent particles obeys the laws of classical mechanics. Thus, the interaction between these particles and their trajectories are calculated by solving Newton's law of motion.

Force field (FF) based methods have been developed as an alternative to QC methods. FF methods use simplified functional forms and provide much better computational performance, enabling simulations to access much larger scales, of order nanometers in length and nanoseconds in time. However, most of the available force field methods are typically nonreactive in nature, implying the inability to simulate bond breaking and formation. To bridge the gap between minimal computational cost and the ability to simulate reactions, a genre of force field methods known as 'reactive force fields' was developed. The reactive force field methods[63], [67]–[69] possess the capability of simulating reactions on-the-fly.

Introduction to ReaxFF

The ReaxFF reactive force field method is a bond order based empirical potential that accounts for reactions by allowing bond formation and bond breakage during the simulation. In ReaxFF, forces on each atom are derived from the following energy expression

$$E_{system} = E_{bond} + E_{over} + E_{under} + E_{lp} + E_{val} + E_{tor} + E_{vdWaals} + E_{coulomb} \quad (2.1)$$

where partial energy contributions include bond, over-coordination penalty and under-coordination stability, lone pair, valence, and torsion, non-bonded interactions van der Waals, and Coulomb energies, respectively.

ReaxFF uses the concept of bond orders (BOs) to determine the bonded interactions among all atoms in a system. BOs are calculated from the interatomic distance and updated in every iteration. Since all the connectivity dependent interactions, i.e., valence and torsion energy are BO dependent, their energy contribution diminishes upon bond breaking. In non-reactive force fields, non-bonded interactions i.e., van der Waals and Coulomb are usually calculated between atom pairs that are not involved in a bond or not sharing a valence angle. However, in a reactive environment, atomic connectivity changes during a simulation and it is awkward to setup such an exclusion rule, therefore, in ReaxFF non-bonded interactions are calculated between all the atom pairs irrespective of their connectivity. To avoid Coulomb catastrophe due to short-range attraction between oppositely charged atoms, any excessive short distance non-bonded interactions are screened by using a shielding term in the van der Waals and Coulomb energy expressions. To eliminate any discontinuity in the non-bonded interaction energies, a seventh order taper function is employed [70]–[72]. A geometry dependent charge calculation scheme, Electronegativity Equalization Method (EEM) [71] and Atom-condensed Kohn-Sham DFT approximated to second order (ACKS2) [72] are used for charge calculation. ReaxFF uses several parameters that can be trained against empirical data, such as results from Density Functional Theory methods (DFT), other first-principle based methods or experiments, to ensure the energy description (*Esystem*) is capable of replicating realizable reaction paths and atomic trajectories.

Description of the ReaxFF Energy Functional

The key ReaxFF energy functionals are described briefly in this section, while a complete description of each energy term can be found in reference [73].

Bond Order and Bond Energy (E_{bond})

ReaxFF assumes that the bond order between any two atoms can be calculated from their interatomic distance using equation (2.2), which distinguishes between contributions from σ bond, π bond and double π bond.

$$BO'_{ij} = \exp\left[p_{bo,1}\left(\frac{r_{ij}}{r_{0\sigma}}\right)^{p_{bo,2}}\right] + \exp\left[p_{bo,3}\left(\frac{r^{\pi}_{ij}}{r_{0\pi}}\right)^{p_{bo,4}}\right] + \exp\left[p_{bo,5}\left(\frac{r^{\pi\pi}_{ij}}{r_{0\pi\pi}}\right)^{p_{bo,6}}\right] \qquad (2.2)$$

Equation (2.2) is a summation of three terms where the terms represent the contribution of σ, π and double π bonds between the atoms *i* and *j* respectively. r_{ij} is the distance between *i* and *j*, $r_{0\sigma}$, $r_{0\pi}$ and $r_{0\pi\pi}$ are the bond radii of σ, π and double π bonds, respectively. The terms p_{bo} are empirical which can be obtained through parameter fitting to available experimental or quantum data. Equation (2.3) is used to calculate bond energy from corrected bond orders.

$$E_{bond} = -D^{\sigma}_{e}.BO^{\sigma}_{ij}.e\exp\left[p_{be1}\left(1-\left(BO^{\sigma}_{ij}\right)^{p_{be2}}\right) - D^{\pi}_{e}BO^{\pi}_{ij} - D^{\pi\pi}_{e}BO^{\pi\pi}_{ij}\right] \qquad (2.3)$$

where p_{be1}, p_{be2}, D^{π}_{e} and $D^{\pi\pi}_{e}$ are force field parameters.

Lone Pair Energy (E_{lp})

Lone pair, Δ^{e}_{i} is the difference between the total number of electrons in the outer shell and

the sum of bond orders around the atomic center. The number of lone-pairs around an atom is calculated using equation (2.4b). The lone pair energy penalty is given by:

$$\Delta_i^e = -Val_i^e + \sum_{j=1}^{neighbor(i)} BO_{ij} \tag{2.4a}$$

$$n_{lp,i} = \text{int}\left(\frac{\Delta_i^e}{2}\right) + \exp\left[-p_{lp1}\left(2 + \Delta_i^e - 2.\text{int}\left(\frac{\Delta_i^e}{2}\right)\right)^2\right] \tag{2.4b}$$

$$\Delta_i^{lp} = n_{lp,opt} - n_{lp,i} \tag{2.4c}$$

$$E_{lp} = \frac{p_{lp2}\Delta_i^{lp}}{1+\exp\left(-75.\Delta_i^{lp}\right)} \tag{2.4d}$$

Where Δ_i^{lp} is the deviation from the optimal lone pair to the calculated lone pair and p_{lp1}, p_{lp2} are the force field parameters.

Over-coordination Energy (E_{over})

Equation (2.5a) calculates the over-coordination (Δ_i) of an atom and if Δ_i > 0, an energy penalty *Eover* is imposed which is calculated using equation (2.5b)

$$\Delta_i = -Val_i + \sum_{j=1}^{neighbor(i)} BO_{ij} \tag{2.5a}$$

$$E_{over} = \frac{\sum_{j=1}^{nbond} p_{ovun1}.D_e^{\sigma}.BO_{ij}}{\Delta_i^{lpcorr} + val_i}.\Delta_i^{lpcorr}.\left[\frac{1}{1+\exp\left(p_{ovun2}.\Delta_i^{lpcorr}\right)}\right] \tag{2.5b}$$

$$\Delta_i^{lpcorr} = \Delta_i - \frac{\Delta_i^{lp}}{1 + p_{ovun3}.\exp\left(p_{ovun4}\left\{\sum_{j=1}^{neighbors(i)}\left(\Delta_j - \Delta_j^{lp}\right).\left(BO_{ij}^{\pi} + BO_{ij}^{\pi\pi}\right)\right\}\right)} \quad (2.5c)$$

While calculating the lone pair energy, ReaxFF takes account of the deviation from optimal number of lone pairs, which is known as corrected over-coordination (Δ_i^{lpcorr}).

Under-coordination Energy (E_{under})

For an undercoordinated atom ($\Delta_i < 0$), the energy contribution for the resonance of the π-electron between bonded under-coordinated atomic centers are taken care using equation (2.6). E_{under} is only important when the bonds between under-coordinated atom *i* and its undercoordinated neighbors *j* have partly π-bond character.

$$E_{under} = -p_{ovun5}.\frac{1-\exp\left(p_{ovun6}.\Delta_i^{lpcorr}\right)}{1+\exp\left(-p_{ovun2}.\Delta_i^{lpcorr}\right)}.\frac{\Delta_i^{lp}}{1 + p_{ovun7}.\exp\left(p_{ovun8}\left\{\sum_{j=1}^{neighbors(i)}\left(\Delta_j - \Delta_j^{lp}\right).\left(BO_{ij}^{\pi} + BO_{ij}^{\pi\pi}\right)\right\}\right)} \quad (2.6)$$

The additional terms related to the over and undercoordination energy functional related to the eReaxFF method are described in the eReaxFF part of this Chapter.

Valence Angle Energy (E_{val})

The valence angle equation (2.7) ensures that the energy contribution due to angle diminishes as the bond order in the valence angle goes to zero. Θ_0 and Θ_{ijk} in equation (2.7) are equilibrium angles which depend on the sum of π bond orders around the central atom *j*.

$$E_{val} = f_7\left(BO_{ij}\right).f_8\left(BO_{jk}\right).f_8\left(\Delta_j\right).\left(p_{val1} - p_{val1}.\exp\left[-p_{val2}\left(\Theta_0\left(BO\right)-\Theta_{ijk}\right)^2\right]\right) \quad (2.7)$$

The exact functional forms of f_7 and f_8 can be found in reference[74] where p_{val1} and p_{val2} are force field parameters.

Torsion Angle Energy (E_{tor})

Torsion angle energy term is dependent on bond order like bond and angle energy term. It disappears when BO approaches to 0. The torsion angle energy term is expressed as follows:

$$E_{tor} = f_{10}\left(BO_{ij}, BO_{jk}, BO_{kl}\right).\sin\Theta_{ijk}.\sin\Theta_{jkl}.$$
$$\left[\frac{1}{2}V_1.\left(1+\cos\omega_{ijkl}\right)+\frac{1}{2}V_2.\exp\left\{p_{tor1}\left(BO_{jk}^{\pi}-1+f_{11}\left(\Delta_j,\Delta_k\right)\right)^2\right\}\left(1-\cos 2\omega_{ijkl}\right)+\frac{1}{3}V_3.\left(1+\cos 3\omega_{ijkl}\right)\right] \quad (2.8)$$

van der Waals Interaction Energy ($E_{vdWaals}$)

To account for van der Waals interactions, distance-corrected Morse potential is chosen. By considering the shielded interaction, excessively high repulsions between bonded atoms and atoms sharing a valence angle are avoided.

$$E_{vdWaals} = Tap.D_{ij}.\left\{\exp\left[\alpha_{ij}\left(1-\frac{f_{13}\left(r_{ij}\right)}{r_{vdW}}\right)\right]-2.\exp\left[\frac{1}{2}\alpha_{ij}\left(1-\frac{f_{13}\left(r_{ij}\right)}{r_{vdW}}\right)\right]\right\} \quad (2.9a)$$

where Tap is a taper term which circumvents energy discontinuities when charged species move in and out of the non-bonded cutoff radius.

$$f_{13}\left(r_{ij}\right)=\left[r_{ij}^{p_{vdW}}+\left(\frac{1}{\gamma_w}\right)^{p_{vdW}}\right]^{\frac{1}{p_{vdW}}} \tag{2.9b}$$

Coulomb Interaction Energy ($E_{Coulomb}$)

Coulomb interactions are calculated for each pair of atoms. A shielded Coulomb potential is used to adjust orbital overlap between atoms at close distance. The EEM method uses following set of equations for the calculation of atomic charges:

$$\frac{\partial E}{\partial q_1}=\chi_1+2q_1\eta_1+C.\sum_{j=1}^{n}\frac{q_j}{\left(r_{1,j}+\left(\frac{1}{\gamma_{1,j}}\right)^3\right)^{\frac{1}{3}}}$$

$$\frac{\partial E}{\partial q_2}=\chi_2+2q_2\eta_2+C.\sum_{j=1}^{n}\frac{q_j}{\left(r_{2,j}+\left(\frac{1}{\gamma_{2,j}}\right)^3\right)^{\frac{1}{3}}}$$

…….

$$\frac{\partial E}{\partial q_n}=\chi_n+2q_n\eta_n+C.\sum_{j=1}^{n}\frac{q_j}{\left(r_{n,j}+\left(\frac{1}{\gamma_{n,j}}\right)^3\right)^{\frac{1}{3}}}$$

$$\sum_{i=1}^{n}q_i=0 \tag{2.10}$$

where χ, η, γ, r, and q are atom electronegativity, hardness, shielding, the interatomic distance, and atomic charge, respectively. The columbic interactions are calculated as

$$E_{coulomb} = Tap.C.\frac{q_i q_j}{\left[r_{ij}^3 + \left(\frac{1}{\gamma_{ij}}\right)^3\right]^{\frac{1}{3}}} \tag{2.11}$$

Introduction to eReaxFF

Most of the available force field methods provide a substitute for the electronic structure implying the absence of explicit electrons and their impact on system geometry and energy. however, the implicit treatment of electrons is inadequate for the description of many physical systems, such as reduction and oxidation reactions of rechargeable battery interfaces, polarization behavior in ferro-electric / piezo-electric materials, fuel cells, solar cells etc. An accurate description of these phenomena requires an explicit treatment of electron degrees of freedom, which must be within the classical framework of the classical potentials. Recently, a number of force field methods have been developed that include aspects of explicit valence electrons, like the electron force field (eFF) [75], [76] and LEWIS [77], [78] force field. The available parameters for eFF are only limited to a small number of elements in the periodic table, and the primary application areas are materials that are subjected to extreme pressure and temperature apart from the complexity of the reactive systems [75], [76]. LEWIS method, on the other hand, is capable of describing the atomic electron affinities (EA) and ionization potentials (IP) of only the first three row elements, still such description for molecules is not available [79]. The LEWIS method, still faces challenge of describing complex reactions, or high-temperature dynamics with an acceptable level of accuracy. There also exists alternate methods to couple covalent and electrostatic interactions through split-charge equilibration (SQE) [80], [81] for describing charge transfer in reactive dynamics [82], without an explicit electron treatment.

To mimic redox reactions using ReaxFF, charge constraints can be imposed, but such charge constraints are problematic for describing charge transfer in reactive environments. ReaxFF also has difficulty in capturing accurate electron affinity and ionization potential of most species. An accurate description of electron transport phenomena requires an explicit treatment of electron/hole degrees of freedom. eReaxFF [65] method is an extension of the ReaxFF method with description of an explicit electron-like or hole-like particle. The treatment of an explicit electron within the classical framework can only capture the particle nature of electron whereas the wave properties are treated implicitly in the functionals of the ReaxFF method. A limited pseudo-classical explicit electron/hole degrees-of-freedom scheme is incorporated that is complementary to the implicit treatment of electrons in the bonded interactions of ReaxFF. All the many-body bonded and nonbonded interaction terms of ReaxFF are retained. New energy functionals are included to compute pairwise electrostatic interactions for explicit electrons and modifications are made on existing over- and under-coordination energy and lone pair energy terms. The electron or hole is represented as an additional particle that carries a -1 (electron) or +1 (hole) charge, respectively. The nuclei are treated as point charges and electrons as Gaussian wave functions $\psi \propto \exp\left(-\alpha\left(r-r'\right)^2\right)$. The energy is a function of the position of the electron and atomic-centers, and depends on the spread of the Gaussian function, α. The pairwise electrostatic interaction between the electron and core-charge is described as [65], [75]

$$E_{nucl(i)-elec(j)} = -\frac{1}{4\pi\varepsilon_0}\beta\sum_{i,j}\frac{Z_i}{R_{ij}}erf\left(\sqrt{2\alpha}R_{ij}\right) \tag{2.12}$$

where Z_i is the nuclear charge, R_{ij} is the distance between the electron and nucleus, α (Gaussian exponent), and β are constants that depends on the atom type. The core-charge is the charge corresponding to the atomic number of an atom. Electron-electron interactions are treated through Coulomb point charges, and short-range Gaussian repulsion functions.

In ReaxFF, valency and number of lone-pair electrons are treated as constants for an atom type. eReaxFF allows changes in the atom valency and number of lone pair of electrons when explicit electron/hole degrees of freedom are introduced into the system. The diffuse nature of an added explicit electron/hole and its relation to a particular atom is described as a function of the distance between electron/hole and the nuclear position of the host atom. The following exponential function is used to determine the number of electrons in the host atom, at the same time, this function ensures that an electron can virtually split itself among its neighboring atoms, that is, it resembles a partial delocalization in a molecule.

$$n_{el} = \exp\left(-p_{val}.R_{ij}^{2}\right) \tag{2.13}$$

where R_{ij} is the distance between the atom-center and the electron/hole and p_{val} is a general parameter in the force field.

The effect of an explicit electron in the vicinity of an atom can be explained as follows: an electron uptake by an oxygen atom, for instance, decreases its valency and increases its number of valence electrons by one. This changed oxygen atom behaves like a pseudo-fluorine atom, that is, it acquires an electron configuration similar to that of fluorine. The acceptance of a hole acts in the opposite manner, the number of outer shell electrons is reduced, and the valency of the oxygen atom increases from two to three, thus the electron deficient oxygen atom resembles the electron configuration of nitrogen. Accordingly, a set of rules are established in the eReaxFF code that dictates the effect of explicit electron/hole on the respective atom types. The atom valency and the number of lone-pair electrons become a dynamic variable, and they are evaluated at every step of the dynamics.

One of the biggest drawbacks in ReaxFF is that, the bonded and non-bonded interactions are calculated independently, that is, charge is not coupled with the number of valence electrons of an atom type which is used in bond order correction and over- and under-coordination energy terms.

For example, a hydrogen ion (H^+) is considered capable of forming bonds such as H^+-H^+ —despite the positive charge—as the number of valence electron remains one. With the charge-valency coupling, the H^+-H^+ bond is additionally counteracted by the over-coordination terms, as the positively charged H^+ ion loses its valence electron. The explicit charges of an atom are coupled with the atom valency and the over- and under-coordination energies are calculated based on the corrected valence electrons.

Modification in the number of valence electrons of an atom type modifies the degree of over- or under-coordination (Δ_i), thus corresponding energy penalties. A decrease in the valency of an atom at an existing bonding environment increases the over-coordination, resulting in a larger over-coordination energy penalty, and therefore reduces the BO associated with the atom and weakens relevant bonds. For example, in a methane molecule, an electron uptake by the carbon will decrease its valency from four to three, and at this bonding situation the carbon atom is further over-coordinated by ~1 which leads to a significant over-coordination energy penalty, and total bond order of carbon reduction to ~3.0 resulting in the elongation of C-H bonds.

In eReaxFF, the amount of modified degree of over- or undercoordination used in the corresponding energy penalty calculation is designed as a function of both atom and bond types, that is, it is contingent on the atom type as well as on the local bonding environment. This atom and bond-type dependent treatment of over- and under-coordination enable the eReaxFF method to capture EAs or IPs of various species using the same set of atomic-Gaussian parameters. The modified over- and under-coordination energy functionals are given by:

Degree of over-coordination: $$\Delta_i = -Val_i + \sum_{j=1}^{neighbor(i)} BO_{ij} \tag{2.14a}$$

Bond type dependency: $$f_{bond} = n_{el} \frac{\sum_{j=1}^{nbond} BO_{ij}.p_{ij}^{xel1}}{\sum_{j=1}^{neighbor(i)} BO_{ij}} \quad (2.14b)$$

Atom type dependency: $$f_i = \exp\left(-p_i^{xel2}.f_{bond}\right) \quad (2.14c)$$

Explicit electron correction: $$\Delta_i^{xel} = \Delta_i.\exp- p_i^{xel2}.n_{el}.\frac{\sum_{j=1}^{nbond} BO_{ij}.p_{ij}^{xel1}}{\sum_{j=1}^{neighbor(i)} BO_{ij}} \quad (2.14d)$$

$$\Delta_i^{lpcorr} = \Delta_i^{xel} - \frac{\Delta_i^{lp}}{1+ p_{ovun3}.\exp\left(p_{ovun4}\left\{\sum_{j=1}^{neighbors(i)} \left(\Delta_j^{xel} - \Delta_j^{lp}\right).\left(BO_{ij}^{\pi} + BO_{ij}^{\pi\pi}\right)\right\}\right)} \quad (2.14e)$$

$$E_{over} = \frac{\sum_{j=1}^{nbond} p_{ovun1}.D_e^{\sigma}.BO_{ij}}{\Delta_i^{lpcorr} + Val_i}.\Delta_i^{lpcorr}.\left[\frac{1}{1+\exp\left(p_{ovun2}.\Delta_i^{lpcorr}\right)}\right] \quad (2.14f)$$

$$E_{under} = -p_{ovun5}.\frac{1-\exp\left(p_{ovun6}.\Delta_i^{lpcorr}\right)}{1+\exp\left(-p_{ovun2}.\Delta_i^{lpcorr}\right)}.\frac{\Delta_i^{lpcorr}}{1+ p_{ovun7}.\exp\left(p_{ovun8}\left\{\sum_{j=1}^{neighbors(i)} \left(\Delta_j^{xel} - \Delta_j^{lp}\right).\left(BO_{ij}^{\pi} + BO_{ij}^{\pi\pi}\right)\right\}\right)}$$

(2.14g)

The explicit electron correction depends on the BOs and the electron occupancy of the host atom. The bond type parameter (p_i^{xel1}) and the corresponding BOs are used to adjust the number of electrons available to the host atom (Eq. 2.14(b)). The atom type dependency is introduced through Eq. 2.14(c), where p_i^{xel2} is an atom type parameter. Finally, the explicit electron correction on the Δ_i is expressed in Eq. 2.14(d) as Δ_i^{xel} . The Δ_i^{xel} is used in Eq. 2.14(e), 2.14(f), and 2.14(g)

to calculate the explicit electron modified over- or under-coordination energy penalty. A variable valency is considered in the over- and under-coordination and lone-pair energy functionals.

In the eReaxFF description, the electron is a negatively charged particle, therefore, it is mostly localized at a particular site in the molecule during geometry optimization. A limited degree of delocalization is still available among the neighboring atoms through the modification of their valence. This delocalization influences the local chemistry of the molecule. Quantum calculations indicate a higher-degree of delocalization of the added electron over the entire molecule, compared to the eReaxFF method. This particular limitation is a result of the treatment of the electron as a pseudo-classical particle. The eReaxFF code has been recently implementation in the commercial Amsterdam Density Function (ADF) [83] package that is capable of parallel processing.

ACKS2 Charge Calculation Scheme

The EEM method—widely used within the ReaxFF approach—is known for its spurious long-range charge transfer, for instance, between two or more molecules, even when they are well-separated [84]. It allows charge to be redistributed over all atoms as if the total system is an electric conductor [85], [86]. The long-range charge transfer of the EEM scheme is problematic for the eReaxFF method, as it impedes the accurate charge description of the reduced/oxidized molecules. The metallic polarizability of the EEM charges results in an almost complete charge compensation of the explicit electrons or holes. The ACKS2 charge calculation scheme [72] largely eliminates the issue of unrealistic long-range charge smearing. Therefore, ACKS2 is implemented in eReaxFF code.

Just like the EEM energy, the ACKS2 energy is quadratic in the atomic charges. Additional variables and quadratic energy terms are introduced to control the range over which charge can delocalize:

$$E_{ACKS2} = \min_{\substack{\{q_i\} \\ \sum q_i = \sum q_i^0}} \left[\sum_{i=1}^{natom} \chi_i q_i + \frac{1}{2} \sum_{\substack{i=1 \\ j=1}}^{natom} n_{ij} q_i q_j + \max_{\substack{\{u_i\} \\ \sum u_i = 0}} \cdot \left[\sum_{i=1}^{natom} u_i \left(q_i - q_i^0 \right) + \frac{1}{2} \sum_{\substack{i=1 \\ j=1}}^{natom} X_{ij} u_i u_j \right] \right]$$

The variables are q_i (atomic charges) and u_i (fluctuations in the atomic Kohn-Sham potential) and are recomputed at each time step for the current geometry. The first two terms are identical to the EEM energy in the conventional ReaxFF, whereas the last two terms are new and account for non-local contributions to the electronic kinetic energy [72]. In ReaxFF, χ_i and n_{ii} are atomic parameters, which are fixed for every chemical element in the calibration process. The parameter q_k^0 is a reference charge: it is zero for all atoms and it is set to −1 or +1 for the explicit electron or hole, respectively. The remaining matrix elements depend on the interatomic distance R_{ij} as follows:

$$n_{ij} = -\frac{1}{4\pi\varepsilon_0} \frac{1}{\sqrt[3]{R_{ij}^3 + \left(\gamma_i \gamma_j\right)^{-\frac{3}{2}}}}$$

$$X_{ij} = X_{soft} \left(\frac{2R_{ij}}{C_i + C_j} \right)^3 \left(1 - \frac{2R_{ij}}{C_i + C_j} \right)^6 \quad \text{when} \quad R_{ij} < \frac{C_i + C_j}{2}$$

$$X_{ij} = 0 \quad \text{when} \quad R_{ij} \geq \frac{C_i + C_j}{2}$$

$$X_{ii} = -\sum_{\substack{j=1 \\ j \neq i}}^{natom} X_{ij}$$

The off-diagonal element n_{ij} represents the Coulomb interaction with short-range damping controlled by the atomic parameters γ_i and γ_j [87]. The off-diagonal element X_{ij} can be interpreted as a bond softness (or atom pair softness): it determines to what extent atom *i* and *j* can exchange charge directly. In the bonding region, X_{ij} increases with increasing R_{ij} until it reaches

its maximum, X_{soft}, and then goes smoothly to zero at the cutoff ($C_i + C_j$)/2. The atomic softness cutoff parameters C_i and the universal softness parameter X_{soft} are fixed in the calibration procedure, with the cutoff parameters remaining short-ranged.

The energy penalty for a direct charge transfer between atoms *i* and *j* is quadratic in charge transfer and is proportional to $1/X_{ij}$ [72]. When X_{ij} is zero, charge transfer must pass through intermediate atoms, with similar energy penalties for all intermediate atom pairs. When no intermediate pairs are present, for example, between two separated molecules, no charge transfer is allowed, and the total charge of each isolated fragment is equal to the sum of the reference charges of the constituting particles. When two distant atoms reside in the same macromolecule, the number of required intermediate pairs, and thus also the energy penalty for charge transfer, scales linearly with the interatomic distance, which effectively inhibits long-range charge transfer.

The constrained minimization and maximization in the ACKS2 energy can be carried out simultaneously by solving a set of linear equations, which is similar to the EEM scheme. In addition, constraints are added to fix the charge of the explicit electron or hole, to −1 or +1, respectively. When some (or even all) X_{ij} elements go to zero, the equations remain well behaved, which is attractive compared to the BOP/SQE model, in which charge transfer is disabled by letting a bond-hardness parameter diverge to +∞ [85]. The polarization catastrophe can be avoided by imposing the following inequalities on the parameters: $n_{ii} > \frac{\gamma_i}{4\pi\varepsilon_0}$ and $X_{soft} > 0$. Under these conditions, the matrices n_{ii} and X_{ij} are guaranteed to be positive and negative semi-definite, respectively, for any possible geometry. As such, the minimum and maximum in the ACKS2 energy are well defined.

Chapter 3

Multiply accelerated ReaxFF molecular dynamics: coupling parallel replica dynamics with collective variable hyper dynamics

This chapter has been published in Molecular Simulation, reference [88], authored by Karthik Ganeshan, Md Jamil Hossain, Adri C. T. van Duin. KG implemented the parallel replica dynamics method and its coupling to collective variable hyperdynamics, and MJH optimized parameters, implemented the reaction analysis tool and performed the collective variable hyperdynamics simulations, under the supervision of ACTvD.

To tackle the time scales required to study complex chemical reactions, methods performing accelerated molecular dynamics are necessary even with the recent advancement in high-performance computing. A number of different acceleration techniques are available. Here we explore potential synergies between two popular acceleration methods – Parallel Replica Dynamics (PRD) and Collective Variable Hyperdynamics (CVHD), by analyzing the speedup obtained for the pyrolysis of n-dodecane. We observe that PRD + CVHD provides additional speedup to CVHD by reaching the required time scales for the reaction at an earlier wall-clock time. Although some speedup is obtained with the additional replicas, we found that the effectiveness of the inclusion of PRD is depreciated for systems where there is a dramatic increase in reaction rates induced by CVHD. Similar observations were made in the simulation of ethylene-carbonate/Li system, which is inherently more reactive than pyrolysis, indicate that the speedup obtained via the combination of the two acceleration methods can be generalized to most practical chemical systems.

Introduction

While atomistic-scale simulation tools have proven to be greatly useful in understanding and developing new materials, a choice is often required to be made on the simulation method to be used based on the required chemical accuracy and computational speed [89]. Ab initio methods such as Density Functional Theory (DFT) and the semi-empirical Tight-Binding DFT (DFTB) rely on obtaining the interaction potentials between the atoms using approximations to the equations of motion derived from Quantum Mechanics (QM). The evaluation of the partial or full electronic structure of each atom allows these methods to be the closest in obtaining chemical accuracy; but the requirement to re-evaluate the potentials at every timestep for dynamics makes the associated dynamical method, termed Ab initio Molecular Dynamics (AIMD), often too computationally expensive for practical applications. Classical non-reactive molecular dynamics is a method capable of simulating several thousand atoms efficiently. This is because the dynamics is obtained using Newton's laws of motion and the interatomic potentials are evaluated using efficient empirically optimized functions. However, the inability to form or break bonds prevent the method from being useful in simulating a reactive environment. A bridge between the two classes of methods is provided by reactive MD tools, such as ReaxFF [90], COMB [91], AIREBO [92], and MEAM [93]. Though these methods retain several similarities to nonreactive MD in using the classical equations of motion, the interaction potentials between the atoms are designed to allow bond breakage and bond formation by including parameters such as the bond order. These interactions are often trained against QM-data, or experiments when available, so that they can mimic the results of QM-based methods at a fraction of the cost while being only about 2 orders of magnitude more expensive than non-reactive MD for dynamics. Using the correct training set for the given system, these methods can reach very close to the chemical accuracy that can be obtained through DFT. Therefore, reactive MD can be used for efficiently capturing both dynamic and

chemical events for large systems at an acceptable efficiency. However, there is one limitation that is shared by all the above-mentioned methods that prevent long simulations – the largest time step to retain stability of the scheme. This issue arises from the requirement to resolve the vibrational modes of bonds between atoms. Typical time steps in ReaxFF are less than a femtosecond to ensure convergence of energy and prevent unphysical de/bonding interactions. Although higher order time stepping methods, such as Runge–Kutta (RK4), would generally help increase the time step while retaining stability, the short timescales in the vibrational modes prevent it from providing a practical advantage [94].

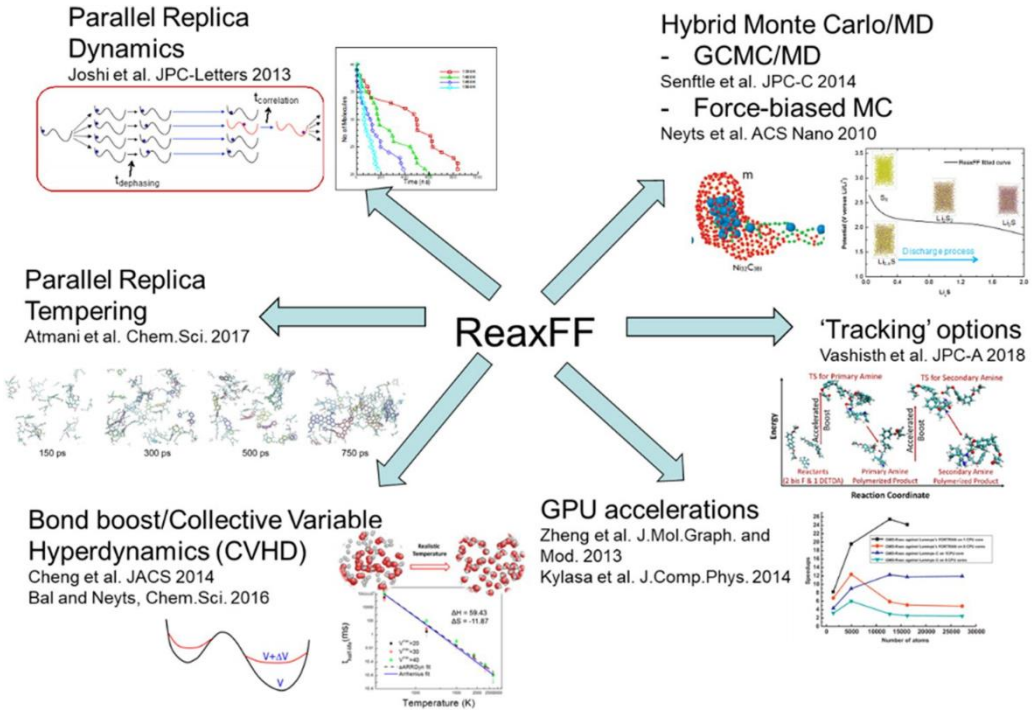

Figure **3-1**: Various acceleration methods available in the ReaxFF reactive molecular dynamics environment.

Figure **3-1** shows the acceleration methods currently implemented in ReaxFF, that help resolve the issue of extended residence time in a potential basin. GPU-enabled algorithms [95], [96] attempt to improve the per-timestep simulation time by utilizing the massively parallel

architecture of GPUs, providing a 6× to 16× speedup compared to CPU-based algorithms. Although this does not tackle the time step issue, it enables ReaxFF simulations to perform at close-to non-reactive MD speeds. Parallel Replica Dynamics (PRD) [97]–[100] is another method that takes advantage of the parallelism. Instead of running a single simulation over multiple processors, the system is replicated over each processor such that each trajectory samples the potential basin until one

observes a transition, providing a speedup directly proportional to the number of replicas used. Other methods rely on modifying the dynamics of the system to obtain the acceleration. In Temperature Accelerated Dynamics (TAD) the simulation is performed at an elevated temperature to allow quick escape of the system from the potential basin, and the correct transitions corresponding to the lower temperature are picked [101]. As at higher temperatures, entropically favored reactions dominate over the reaction pathways corresponding to lower temperatures, caution must be exercised in ensuring only the feasible paths are picked. Methods such as Hyperdynamics [102], Metadynamics [103] and Collective-Variable Hyperdynamics (CVHD) [104], modify the free energy landscape by providing a bias potential, which fills the energy minima and decreases the energy barrier for the transitions. Force Biased Monte Carlo [105] and Grand Canonical Monte Carlo (GCMC/MD) [106], use Monte Carlo techniques to enable the system to reach a global minima faster. However, these methods may not capture the correct dynamics associated with transition. Other methods include Bond Boost [107], where a potential bias and Tracking [108], where an additional force, is added to the bonds of labeled atoms to accelerate the dynamics.

In this work, we explore the combination of PRD and CVHD due to the mutual exclusivity in the acceleration method and generalizability to any reactive system. A descriptive introduction to the two methods and their combination is provided in the subsequent section, followed by the performance comparison against standard MD for n-dodecane pyrolysis.

Methods

Parallel Replica Dynamics

PRD takes advantage of the assumed ergodicity of the molecular dynamics process and the availability of several computer cores. For an ergodic process, the time average of the process in the simulation is the same as the ensemble average. Therefore, averaging over a large time domain is replaced by time averaging over multiple short simulations with different initial conditions. When the system is replicated amongst M replicas, it enables the overall simulation to sample M different escape routes out of the potential basin, c.f. Figure **3-2**. As a consequence, the trajectory that leads the system out of the potential basin can be identified in a shorter wall-time. The simulation procedure for PRD are as follows [97], [109]:

(1) Broadcast the configuration and minimize it over *M* replicas

(2) Initialize each replica with a unique random velocity distribution corresponding to the temperature

(3) Ensure each trajectory corresponds to a quasi-stationary state (dephase)

(4) MD run and check for any transitions

(5) Decorrelate the trajectory with respect to the transition state

(6) Purge all replicas and go to step 1

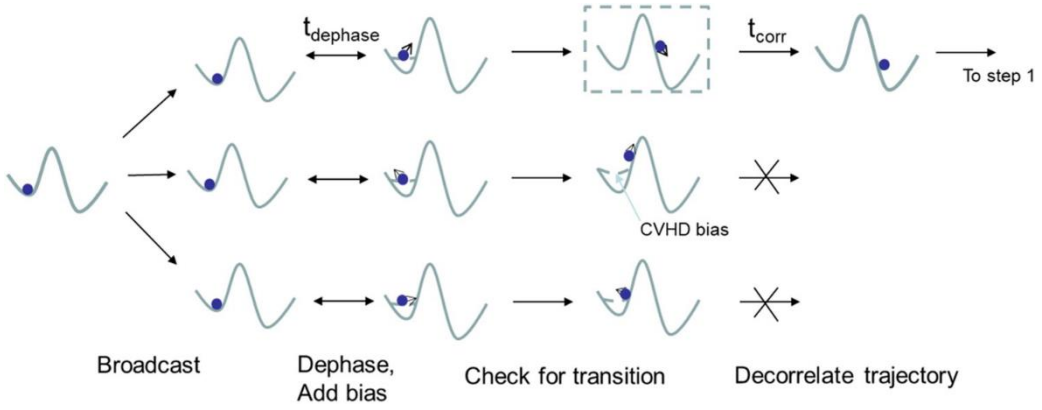

Figure **3-2**: Schematic of the implementation of PRD coupled with CVHD under a representative free energy surface (FES). The arrows indicate the direction the system is moving towards, over the FES.

A trajectory is considered to contain a 'successful event' when it has crossed the chosen potential barrier. In a reactive environment, any dominant reaction leading to a change in bonds can be considered as a successful event [98]. In some cases, the first crossing of the potential barrier may lead to a series of secondary reactions. These secondary events must not be considered as an independent successful event due to their underlying correlation to the primary event.

The checks for correlation (step 5) and dephasing (step 3) are included to ensure no error is introduced by PRD and that the mutual independence of the replicas is maintained. To broadcast the configuration with the successful event to another set of replicas and initialize with a different set of random velocities, it is required that the configuration is not correlated to its earlier transition state and any correlated secondary event must be completed. For all MD simulations, two trajectories with a small difference in initial conditions become uncorrelated after a certain period of simulated time due to the Lyapunov instability [94]. Let τ_{corr} correspond to the time for which the system continues to be correlated to the state that crossed the potential barrier and $\Delta t_{MD,corr}$ be the MD time after the potential barrier has been crossed. Ensuring that $\Delta t_{MD,corr} \geq \tau_{corr}$ guarantees that the reinitialization of the configuration with a different set of velocities will not be

correlated to the earlier transition state. Although τ_{corr} is system dependent, it is generally ~1 ps or a few Einstein vibrational periods [97]. Another criterion is that we sample only the quasi-stationary distribution during PRD. Therefore, the trajectories that leave the potential basin at time $t \leq \tau_{dephase}$ are purged and then re-initialized with different random velocities. The time of the purged simulations is not added to the effective PRD time. The mathematical formulation of PRD, including the restrictions imposed by the dephasing and correlation criteria, can be found in references [99] and [100].

The total simulated time is a sum of the individual time simulated by each replica, i.e.

$$t_{total} = \sum_{i}^{M} t_i \quad , \tag{3.1}$$

where t_i is the time simulated by the i^{th} replica. This is used instead of $t_{eff} = Mt_1$ *to* account for performance differences between the processors. The acceleration over standard MD is given by [109]:

$$\eta_{PRD} = M((1+ f_Q)(1+ 2Mk_g\tau_{corr}))^{-1} \quad . \tag{3.2}$$

Here, f_Q is the cost associated with checking for a successful event, per time step, and k_g is the transition rate for the observed reaction. The inverse relation to k_g indicates that the most acceleration is obtained only for rare events, i.e. $k_g \rightarrow 0$. Although it is not a requirement of the method, the most acceleration from PRD can be obtained when each replica is run on a single processor. Therefore, standard PRD quickly loses its effectiveness to methods that vary the potential energy surface, such as hyperdynamics, when using methods like AIMD or reactive MD simulations of very large systems ($N_{atoms} \gg 10^3$).

Collective variable hyperdynamics (CVHD)

Collective Variable Hyperdynamics is a combination of conventional metadynamics and hyperdynamics. Metadynamics [103] is a technique that is capable of calculating free-energy landscapes by using a history-dependent bias potential. The bias potential is dependent on a small number of collective variables (CVs) that describe the system. The bias potential is applied to the potential energy surface, which fills the energy minima and consequently lowers the reaction energy barrier and thus, shortens the waiting time between reactions. On the other hand, hyperdynamics is an accelerated MD technique which is similar to metadynamics in the sense that it is also based on the application of a bias potential but in hyperdynamics this bias potential is removed on-the-fly during the transition state. The free energy information is lost by the unbiasing but the hypertime can be recovered from the simulation. The Hypertime is the time required to get to a similar state in an unbiased simulation. The collective variable-driven hyperdynamics (CVHD) method [104] is a self-learning variant of the hyperdynamics algorithm that combines the hyperdynamics with CV-based feature of metadynamics in which an appropriate history-dependent bias potential can slowly be grown on the fly during the simulation to track the long time scale evolution of the system.

The choice of an appropriate collective variable (CV) is essential for a CVHD simulation. The CV is based on a set of local system properties or degrees of freedom (s_1, ..., s_N), which collects all the relevant degrees of freedom of the full slow system dynamics. Following the description from Bal and Neyts [104], for each local property s_i, a local distortion ($\chi_i = \chi(s_i)$) is defined and can have a value between 0 and 1, the value of 1 being at the transition state. The global distortion is defined as

$$\chi_t = \left(\sum_{i=1}^{N} \chi_i^p \right)^{\frac{1}{p}} \tag{3.3}$$

in which $p > 1$. The CV η is defined as

$$\eta = \frac{1}{2}\left(1-\cos\left(\pi\chi_t^2\right)\right) \quad , \text{if } \chi_t \leq 1 \tag{3.4a}$$

$$\eta = 1 \quad , \text{ if } \chi_t > 1 \tag{3.4b}$$

For reaction events involving bond breaking, the property s is considered as the stretch of a bond. For every bond pair i with length r_i, there are distances r_i^{min} and r_i^{max}, which mark the begin point and end point of possible reactive events. If $r_i < r_i^{min}$, the bond is not likely to dissociate soon, and is not biased, whereas if $r_i = r_i^{max}$, the bond is about to dissociate. For $r_i^{min} < r_i < r_i^{max}$ the local distortion is defined as

$$\chi_i = \frac{r_i - r_i^{\min}}{r_i^{\max} - r_i^{\min}} \tag{3.5}$$

The bias potential ΔV which is deposited at intervals τ_G is defined as a function of the CV η as a Gaussian shaped hill with width δ and height w_k as follows

$$\Delta V\left(\eta\right) = \sum_{k<n_G} w_k \exp\left[-\frac{\left(\eta-\eta\left(k\tau_G\right)\right)^2}{2\delta^2}\right] \tag{3.66}$$

The bias potential being dependent on the CV makes it history dependent. Gaussian shaped hills are added until a transition state is reached. Similar to the choice of the CV, choosing a suitable bias is hard and error-prone.

Using a bond length based CV, Bal and Neyts [110] applied the CVHD method in the pyrolysis and oxidation of n-dodecane at low temperatures and reached time scales which are unattainable by conventional molecular dynamics simulations.

CVHD coupled with PRD

The standard MD in each PRD replica can be replaced with an individually accelerated MD, such as CVHD or hyperdynamics, to obtain additional speedup per timestep. Such a combination of PRD and hyperdynamics has been evaluated by Voter & Germann for epitaxial growth of Ag layer [111]. The combination multiplies the effective increase in time of PRD to that of hyperdynamics, as described in the following equation [112].

$$t_{eff} = \sum_{i}^{M} t_i = \sum_{i}^{M} \sum_{j}^{N} \Delta t_{MD,i} exp\left[\Delta V\left(r_i\left(t_j \right) \right) / k_b T \right]. \tag{3.7}$$

It must be noted that the inclusion of hyperdynamics increases the rate of reaction observed in PRD, i.e. k_g has to be replaced by $\eta_{HD} k_g$ where η_{HD} is the boost provided by hyperdynamics. This increased rate of reaction diminishes the acceleration provided by PRD because of its inverse relation to k_g, as implied by equation (2). Therefore, the bias potential must be appropriately matched to maintain reasonable benefits in using the coupling to PRD.

Here, we explore the combination of PRD with CVHD to eliminate the requirement to have predefined boost potential. While both the methods reset after a transition has occurred, it is not required that the same transition is targeted. Therefore, a transition with a higher barrier could be targeted by PRD while CVHD is permitted to reset after transitions that occur at lower barriers. To provide an example, a large barrier transition could be a chemical reaction and a small barrier transition could be one associated with an internal rotational barrier for a partially conjugated hydrocarbon (e.g. butadiene). With this separation of event checks, we can utilize a lower CVHD boost potential to ensure that the smaller barriers are not bypassed while maintaining reasonable effectiveness of PRD. Figure **3-2** shows a schematic of a PRD+CVHD simulation under a representative free energy surface.

Simulation setup

The pyrolysis of n-dodecane was considered to study the effectiveness of PRD+CVHD in comparison to standard CVHD, as the process follows first order kinetics [98] and a reference CVHD parameters can be obtained from Bal and Neyts [110]. Here, 24 n-dodecane molecules were considered in a 50 Å × 50 Å × 50 Å periodic box, at a simulation temperature of 1200 K and 1500 K, with a density of 0.054 kg dm^{-3}. The parameters for CVHD from [110] were retained – a gaussian height of 0.25 kcal mol^{-1} was used with the gaussian half width of 0.025. The frequency of deposition of 0.2 ps and a 1 ps waiting period to check for an event was used. A local bond-breaking event check was implemented, based on which the boosted potential in equation (6) is altered. To maintain similarities with the reference [110], the ReaxFF force field parameters for C/H/O described by Chenoweth et al. [90] was used. A monitoring script was written in Bash to implement PRD by initiating and terminating replica MD runs based on event detection. The trajectory where one dodecane molecule completes a reaction is considered to contain the successful event for PRD. A sample pyrolysis reaction is shown in Figure **3-3**, where one of the 24 n-dodecane molecules decomposes into C_4H_9 and C_8H_{17} radicals.

The check for the transition is made by setting a bond order cutoff of 0.3 and counting the number of dodecane molecules based on the connectivity of each atom. Based on the analysis of the velocity autocorrelation of heptane [98], a τ_{corr} of 10 ps and $\tau_{dephase}$ of 5 ps was chosen. A higher τ_{corr} was opted to allow sufficient time for the secondary reactions to complete. The PRD algorithm mentioned earlier was slightly modified – the minimization of the system before checking for a transition was replaced by a primary check for the event followed by a confirmation check after $\Delta t_{MD} = \tau_{buffer}$. This eliminates any false positives generated by quickly reversible reactions without the requirement of pausing the MD run. Therefore, the PRD script does not interfere with the MD run until the reaction is complete, confirmed and passed the correlation

time. Here, a τ_{buffer} of 2 ps is considered. As the event detection is computationally cheap, a moderately frequent event check is carried out at every 0.1 ps to prevent extended runtimes after a successful transition is made. The PRD implementation, including the event checks, are external to the CVHD/MD run; which eliminates any additional computational overhead experienced by the simulation. However, there is a caveat – one additional processor that cannot be involved in the MD simulation is required to run the PRD monitoring and event check programs. As the process is serial and generally not computationally taxing, it can be accommodated on a local machine that is capable of initiating MD runs on another batch of processors. All MD/CVHD simulations were performed in ReaxFF within the ADF suite, distributed by SCM (see www.scm.com). ADF version later than 2017-r60492 is required to ensure each replica is initiated with a different random velocity.

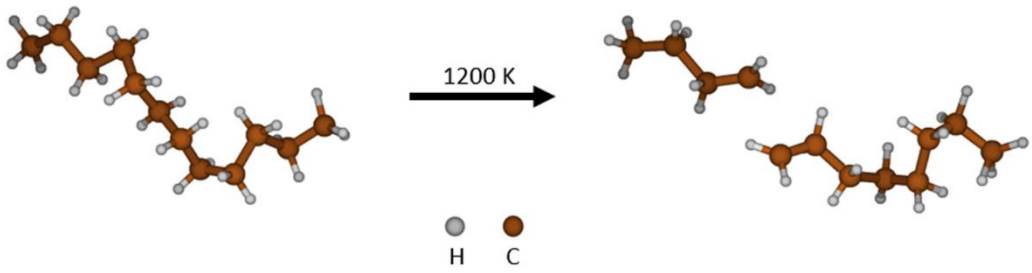

Figure **3-3**: One of the 24 n-dodecane molecules decomposing into C4H9 and C8H17 radicals.

Results and discussion

Figure **3-4** shows the difference in the time simulated by standard MD, PRD, CVHD and PRD + CVHD. Here, the initial stage of n-dodecane pyrolysis simulated by a 4-replica CVHD simulation is considered for illustrative purposes. Similar to the observation made by Voter and Germann [111], we see that over a relatively large number of steps, CVHD outperforms MD and standard PRD by simulating a time scale that is several orders of magnitude longer. As the

acceleration provided by CVHD slowly builds up with time, a larger speedup is obtained using PRD during very early stages of the simulation, as indicated by Figure **3-4**(b). It must be noted that in this work, we use dynamically biased CVHD instead of statically biased CVHD. In the case with statically biased CVHD we would expect a constant boost for every timestep, providing a linear increase in simulated time, similar to PRD. However, dynamic biasing of the system allows the desirable self-learning mechanism of biasing based on the requirements of the system.

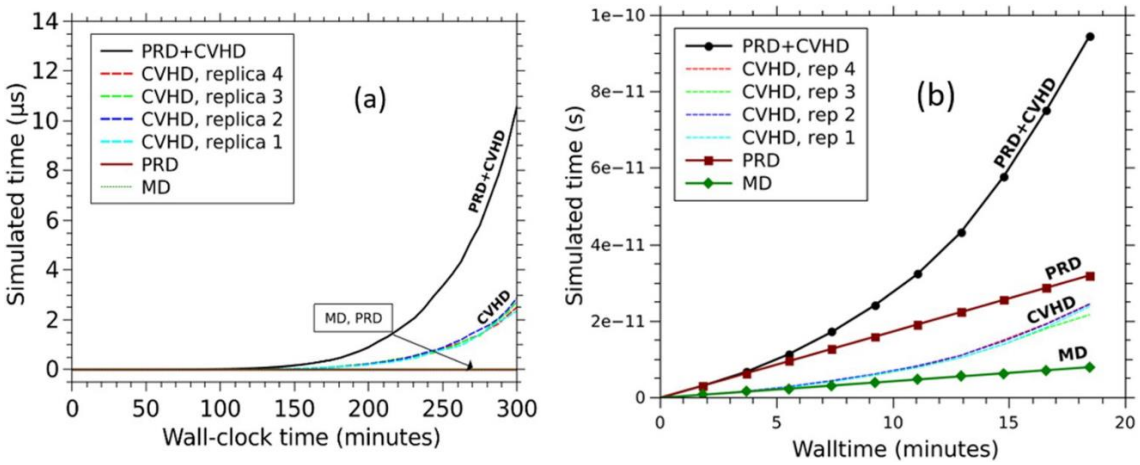

Figure **3-4**: The total simulated time vs wallclock time for different methods. (a) Time simulated at a later stage in simulation, where CVHD >> PRD (b) During the initial phase of the simulation, where PRD > CVHD.

Although the above analysis would indicate that using more replicas would proportionally increase efficiency, it is important to recall Equation (2). The inverse relation to M and kg suggests that there is depreciating gains for large number of replicas, for long simulations that involve several transitions. To evaluate the performance, a PRD + CVHD simulation was set up with 10, 20, 40, 70 and 100 replicas, with the results averaged over 3 sample runs. Each replica simulation was performed on a single Intel Xeon E5 2.5 GHz processor. A standard CVHD simulation was performed to serve as a point of reference, with the time averaged over 10 samples. Figure **3-5**

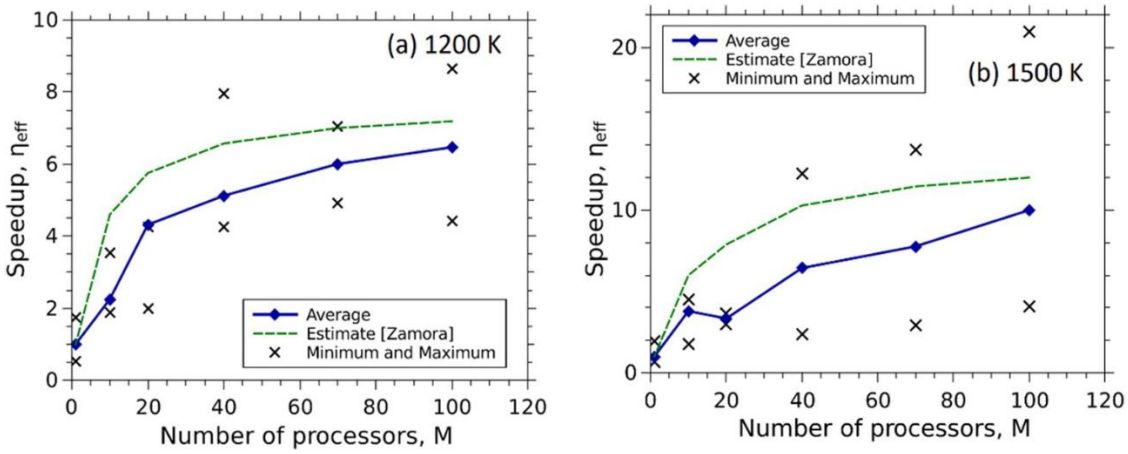

Figure **3-5**: The speedup in simulation obtained by the combination of PRD and CVHD, compared against standard CVHD. (a) Simulation temperature of 1200 K (b) Simulation temperature of 1500 K.

shows the speedup obtained by the inclusion of PRD over standard CVHD, evaluated by using the relation

$$\eta_{eff} = \frac{walltime\ \ for\ 1\ replica}{walltime\ \ for\ M\ \ replicas} \tag{3.8}$$

The theoretical estimate of speedup over CVHD is obtained by following relation

$$\eta_{eff} = \frac{\eta_{PRD+CVHD}}{\eta_{CVHD}} = M\,\frac{1+2k_{g,eff}\tau_{corr}}{1+2Mk_{g,eff}\tau_{corr}} \tag{3.9}$$

Here, $k_{g,eff}$ is the effective reaction rate observed by PRD due to the acceleration provided by CVHD. From the analysis conducted by Chowdhury et al. for n-Dodecane pyrolysis[113], the expected rate constant for the reaction at 1200 K is ≈ 6.1E+04 s^{-1} and $k_g\tau_{corr}$ ≈ 6.1E-07. However, due to the acceleration provided by CVHD, a value of $k_{g,eff}\tau_{corr}$ = 0.075 was used for the evaluation of the estimated speedup at 1200 K. We can immediately see that PRD doesn't scale linearly with the number of replicas as a direct consequence of the inverse relation to $Mk_{g,eff}$

predicted by equation (2). Therefore, only an incremental speedup can be expected when larger number of replicas are used. When conducting a similar experiment at 1500 K, we observe that the speedup obtained by PRD is larger at 1500 K than at 1200 K, as indicated by Figure **3-5** (b). We believe this could be attributed again to the boost provided by CVHD. As the reaction rate is inherently higher at 1500 K, the assistance required from CVHD is lowered. Therefore, the effective rate of the reaction is lower than that of the boosted 1200 K simulation.

The perceived lower reaction rate at 1500 K contributes to the increased effectiveness of PRD. It is important to note that the data presented in Figure **3-5** correspond to the speedup obtained by using PRD in comparison to standard CVHD. Caution must be exercised when following this trend for different temperatures, especially lower temperatures such as 1000 K and 700 K. The effective increase in the rate of the reaction by CVHD is governed by the bias potential properties set a priori by the user. Hence, even at lower temperatures, the effectiveness of the combination of PRD and CVHD can be significant if the bias potential applied is moderated. Therefore, the trend of the effectiveness of the combination of the two methods must be perceived as a function of the effective rate of reaction of the system, rather than a function a particular system property. The total time required to complete the decomposition of three n-dodecane molecules is of the order of 2 μs. Hence, in non-accelerated MD, 2 × 1010 steps or 72 thousand hours would be required. Due to the randomness of the initialized velocity distribution in each system, there will be statistical noise in the results obtained for performance comparison. However, many more samples can be used to obtain a more accurate representation of the average performance.

Table **3-1** shows the cumulative net simulated time across the 3 stages of the PRD simulation. We see that the effective simulated time across multiple number of replicas mostly remains within the same order of magnitude as that of a single CVHD simulation. Comparing the values to the hypertime observed by the successful trajectory in PRD, we can see that the successful trajectory experiences a lower hypertime corresponding to the speedup provided by PRD.

Therefore, it can be inferred that the acceleration provided by CVHD is lowered with coupled with PRD; and the rate of reaction captured is independent of the number of replicas, provided a reasonable boost potential is used in CVHD.

Table **3-2**: Comparison of effective simulated time and hypertime of the trajectory with a successful transition across different number of replicas.

Number of Replicas used	Average simulated time (seconds)	Successful trajectory hypertime (seconds)
1	1.71e-5	1.71e-5
10	2.27e-5	2.59e-6
20	2.55e-6	9.55e-8
40	7.582e-6	2.49e-7
70	1.36e-5	2.03e-7
100	3.33e-5	3.98e-7

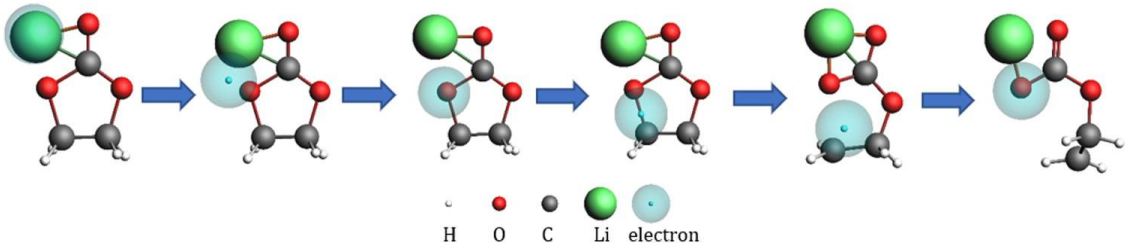

Figure **3-6**: Ring opening reaction of ethylene carbonate induced by Li.

In addition to the pyrolysis of n-dodecane, eReaxFF MD [114] was used to perform a comparative study between MD, PRD and PRD + CVHD for the ring opening reaction of ethylene-

carbonate (EC)/Li system. A system comprising of 201 EC molecules with 15 Li^+/explicit-electron pairs in a periodic cube of dimension 40 Å at density of 0.46 g cm^{-3} was simulated at 300 K using the NVT ensemble with Berendsen thermostat under a damping frequency of 100 fs. 10 replicas were used in both PRD and PRD + CVHD simulations and CVHD parameters – gaussian height of 0.5 kcal mol^{-1} with a half-width of 0.025 at a deposition frequency of 0.5 ps were considered for CVHD and PRD + CHD. For the comparison of accelerations, a complete ring opening reaction of the EC molecule was considered as a successful transition. Figure **3-6** illustrates the simulated ring opening reaction of the EC/Li system. Similar behavior, as that of n-dodecane pyrolysis, is seen when comparing the performance between the different acceleration tools. Although the EC/Li system is more reactive (key barrier around 10 kcal mol^{-1}) in comparison to dodecane pyrolysis (key barrier around 60 kcal mol^{-1} in the presence of radicals; around 80 kcal mol^{-1} for homolytic scission), the results shown in Figure **3-7** provide evidence to generalize that the acceleration provided by the combination of PRD and CVHD is greater than the methods considered independently.

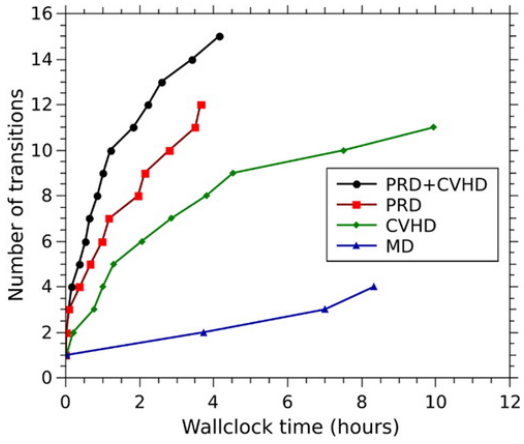

Figure **3-7**: Number of reactive transitions observed in the system vs. wall-clock time.

Conclusion

We have analyzed the performance of the combination of PRD and CVHD for the pyrolysis of n-dodecane. Although the combination of the two provides a method capable of simulating milliseconds to seconds time period in a reasonable wall-clock time, there is a decrease in the speedup obtained in PRD as the rate of reaction increases, especially because of the boost provided by CVHD. The effective simulated time across different combinations of PRD added to CVHD lies within the same order of magnitude. This indicates that the observed reaction mechanism is independent of the number of replicas chosen and using larger number of replicas only save wall-clock time required. Similar speedup obtained for the system of ethylene carbonate/Li indicates that the combined method can be advantageous even for a moderately more reactive system.

Chapter 4

Lithium-electrolyte solvation and reaction in the electrolyte of a lithium ion battery: A ReaxFF reactive force field study

This chapter has been published in The Journal of Chemical Physics, reference [115], authored by Md Jamil Hossain, Gorakh Pawar, Boryann Liaw, Kevin L. Gering, Eric J. Dufek and Adri C. T. van Duin. MJH calculated the DFT data, optimized ReaxFF parameters and performed the simulations, under the supervision of GP and ACTvD.

Introduction

As world population continues to grow and the amount of fossil fuels begins to diminish, it may not be possible to provide the amount of energy demanded by the human population by only means of fossil fuels. It has long been discussed that the ascent of lithium-ion batteries - which are durable and energy-dense and have high operating voltage - would mark the beginning of the end of the fossil-fuel age. A typical Li-ion battery consists of a negative electrode called the anode, a positive electrode called the cathode and an electrolyte solution. Generally, the anode of a conventional Li-ion battery is formed from graphite, the cathode is formed from a transition metal oxide and electrolyte solution is formed from carbonate-based solvents and lithium salts. During battery discharging, battery electrodes are connected through an external circuit and the Li atom in the anode oxidizes to give up its electron and converts to Li^+. The electron flows through the outer circuits and arrives at the cathode while Li^+ diffuses through the electrolyte to the cathode where it gets reduced and becomes Li atom. The charging process operates in an opposite way. During the first charge/discharge cycle of Li-ion batteries, anodic reduction of the electrolytes creates a thin

passivation layer, known as the solid electrolyte interphase (SEI) [4], consisting of different reduction products of electrolytes formed through the reactions in the anode/electrolyte interface due to electron leakage from the anode [116], [117]. The SEI is a multilayered structure with an inorganic inner later and an organic outer layer. It acts as a barrier between the electrolyte solution and the electrode and, thus, prevents decomposition of the electrolytes in the subsequent cycles. The formation of SEI leads to the irreversible loss of Li, therefore detrimentally affecting the capacity of the battery, life time, cyclability and power density [31], [40]–[42]. Ideally an SEI should have zero electron transference number (or electron conductivity) and high ionic conductivity to facilitate easy Li^+ ion migration during the battery operation. Furthermore, the SEI should have an excellent mechanical strength and flexibility to overcome the expansion and contraction of the anode during the Li intercalation/deintercalation process. In addition, SEI should have lower solubility to the electrolyte to limit the continuous consumption of Li. The SEI is considered as the most important but least understood component of a Li-ion battery [116]. Thus, the importance of understanding the mechanism that leads to SEI formation cannot be overemphasized. Essentially, the choice of electrolytes has a significant influence on the formation of an SEI and its underlying chemical and mechanical properties. It is well known that the electrolytes based on ethylene carbonate (EC) form a stable SEI on graphitic anodes that helps prevent the continuous decomposition of electrolyte and concomitantly provides good Li^+ ion conductivity [31], [118]. Therefore, the electrolyte candidates require certain qualities such as high dielectric constants, low viscosity and low melting point. In order to fulfill these diverse operational requirements, typical compositions of electrolytes are based on the mixture of two or more organic solvents and solutions of one or more lithium salts. The most commonly used electrolytes are a mixture of one or more alkyl carbonates, such as ethylene carbonate (EC), dimethyl carbonate (DMC), diethyl carbonate (DEC), and ethyl methyl carbonate (EMC) and $LiPF_6$ salt [33]–[36].

Using spectroscopic methods, many experimental studies have been conducted to study Li transport and solvation in different electrolyte compositions with different Li salts, solvents and concentrations [119]–[121]. They report the Li coordination number around Li^+ ion to be in the range of 2 to 5. Classical force field studies on this matter reported a coordination number of 4 where the Li^+ ion interacts with the carbonyl oxygen of the solvent's carbonate [122]–[125]. Quantum chemistry (QC) based methods such as first-principles molecular dynamics (FPMD) has been used to study Li^+ ion transport and solvation in different electrolytes [58], [126]. However, QC based methods are computationally intensive and mostly limited to small length and time scales. Besides, a combination of QC and classical MD studies has been reported on Li^+ ion solvation and solvent exchange in EC/DMC/$LiPF_6$ electrolytes by Borodin and Smith [127]. Ong et al. [32] combined FPMD and reactive molecular dynamics on the study of Li^+ ion transfer and solvation in EC/DMC/$LiPF_6$ electrolytes. However, no electrolyte reduction reactions have been reported in the study.

The electrolyte reduction that subsequently leads to SEI formation, on the other hand, is challenging to directly capture the reactions at the electrode/electrolyte interface experimentally, as some of the reactions could occur at the picosecond (ps) timescale. Thus, quantum chemistry (QC) and classical molecular dynamics (MD) simulations have been extensively used to study the initial electrolyte reduction decomposition mechanisms. A picture for Li ion battery SEI modeling in many different studies was described in the recent review paper [128]. Wang et al. [129] investigated the possible reduction pathways for EC using density functional theory (DFT) which is a quantum chemistry (QC) based method. A Li bound EC can go through either a single electron reduction process that opens the EC ring or a double electron reduction process that produces Li_2CO_3 and ethylene gas. The one-electron reduction is favored at a high EC concentration, while the two-electron reduction is favorable at a high Li concentration. Both single and double electron reduction reaction products of EC are seen in SEI structures [41], [42]. Based on this study, Leung

and Budzien [56] modeled the reduction pathways of SEI formation using *ab initio* molecular dynamics (AIMD) simulations. Classical MD methods can be employed to a larger length and time scales compared to QC based methods. Bedrov et al. [130] used ReaxFF [63] and Islam et al. [66] used eReaxFF [65] reactive molecular dynamics simulations to investigate EC reduction and SEI formation pathways. Wang et al. [129] also investigated possible reduction processes of $Li^+(EC)_n$ (n=1~5) using DFT and showed that EC can go through one and two electron reductions to create different SEI compounds. Tasaki [131] found that the order for the solvent molecule to go through one-electron reduction is EC > PC > VC > DMC > EMC > DEC with EC being the most likely to be reduced while the order for the two-electron reduction is VC > EC > PC with VC to be the most likely to go through two-electron reduction. Electrolyte additives also play an impactful role in the SEI formation. Using AIMD simulations, Ushirogata et al. [132] found that vinylene carbonate (VC) additive reacts with EC anion radial and, thus, the normal two-electron reduction of EC is surpassed.

Electrons can freely move around in a graphitic anode and leak into the electrolyte. Electrons leaked from the anode can be captured either by the electrolyte molecules or Li^+ ion. Carbonate solvent such as EC has a negative electron affinity (-7.6 kcal/mol) while a Li^+ ion has a strongly positive electron affinity (+128 kcal/mol) [129]. So, Li^+ has a greater chance of capturing an electron than a carbonate solvent. A Li^+ ion reduced to a Li atom by the leaked electron can become highly reactive and can initiate electrolyte reduction decomposition, which is the first step towards SEI formation. To the best of our knowledge, no MD simulations have been performed that describe both Li-electrolyte solvation as well as electrolyte reduction decomposition reactions, probably due to the lack of an accurate intermolecular potential. In order to enable relatively large-scale simulations related to anode/electrolyte interfacial chemistry that leads to SEI formation, we have developed a ReaxFF reactive force field that is able to exhibit Li solvation with up to four EC and EMC molecules as well as capable of initiating electrolyte decomposition reactions. Several

DFT studies [61], [129] report that solvent reduction can occur regardless of being coordinated with Li^+. Although it is not a requirement for Li^+ to be reduced to neutral Li in order to further reduce solvent molecule, we describe neutral Li as a conduit for electron transfer to the solvent for the reduction process. It is convenient for us to turn Li^+ to Li and then let Li take care of the solvent reduction process. To make a distinction between the Li atom and the Li^+ ion, we have introduced a second Li parameter set to describe the Li^+ ion, targeting that both Li neutral and cation will have similar solvent binding energies but unlike Li neutral, Li^+ will have no reactivity with electrolytes. Although Bedrov et al. [130] imposed a +1 charge constraint for Li to describe Li^+ ion, it is still difficult to properly train ReaxFF force field to understand the difference between a Li and Li^+ when an electrolyte reduction decomposition is concerned, unless different sets of parameters are used to distinguish between them. The probability of electrons being captured by a Li^+ cation or electrolyte molecule depends on the voltage and proximity to the graphitic anode. The eReaxFF method [65], [66], which can simulate explicit electrons in the ReaxFF framework, can be helpful in obtaining such a probability distribution. Once the probability distribution is known, the Li^+ cations can be converted to neutral Li in a Monte Carlo fashion and eventually electrolyte reduction decomposition can be expected to occur. In this manuscript we describe the development and validation of the ReaxFF description for the Li^+ cation and neutral Li atom types, the implementation of the Monte Carlo concept and its connection to eReaxFF simulations will be described in a subsequent publication.

Methodology

ReaxFF background

The ReaxFF reactive force field method is a bond order [67], [69] based empirical potential that accounts for reactions by allowing bond formation and bond breakage during the simulation. In ReaxFF, forces on each atom are derived from the following energy expression:

$$E_{system} = E_{bond} + E_{over} + E_{under} + E_{lp} + E_{val} + E_{tor} + E_{vdWaals} + E_{coulomb} \quad (4.1)$$

where partial energy contributions include bond, over-coordination penalty and under-coordination stability, lone pair, valence, and torsion, non-bonded van der Waals interactions, and Coulomb energies, respectively.

ReaxFF uses the concept of bond orders (BOs) to determine the bonded interactions among all atoms in a system. BOs are calculated from the interatomic distance and updated in every iteration. Since all the connectivity dependent interactions, i.e., valence and torsion energy are BO dependent, their energy contribution diminishes upon bond breaking. In non-reactive force fields, non-bonded interactions i.e., van der Waals and Coulomb are usually calculated between atom pairs that are not involved in a bond or not sharing a valence angle. However, in a reactive environment, atomic connectivity changes during a simulation and it is awkward to setup such an exclusion rule, therefore, in ReaxFF non-bonded interactions are calculated between all the atom pairs irrespective of their connectivity. To avoid Coulomb catastrophe due to short-range attraction between oppositely charged atoms, any excessive short distance non-bonded interactions are screened by using a shielding term in the van der Waals and Coulomb energy expressions. To eliminate any discontinuity in the non-bonded interaction energies, a seventh order taper function is employed [70]–[72]. A geometry dependent charge calculation scheme, Electronegativity Equalization Method (EEM) [71] is used for charge calculation. ReaxFF uses several parameters that can be trained against empirical data, such as results from Density Functional Theory (DFT) methods and

other first-principle based methods or experiments, to ensure the energy description (*Esystem*) is capable of replicating realizable reaction paths and atomic trajectories. Since its first formulation for hydrocarbons [63], [133], ReaxFF has been applied to a wide range of systems, including but not limited to Li-ion batteries [134], Li-S batteries [25], [64], 2D materials [135], nanoparticle [136], polymers [137], [138] and ferroelectric materials [139]. Although ReaxFF has been proven to successfully simulate larger timescales compared to QC based methods, sometimes the time scale achieved is not enough to study complex chemical reactions even with the current high-performance computing capabilities. Accelerated molecular dynamics methods in the ReaxFF environment assists to achieve an extended MD time scale. Parallel replica dynamics (PRD) [98], collective variable hyperdynamics (CVHD) [140] and combined PRD-CVHD [141] are some accelerated MD methods that have been applied in the ReaxFF environment.

DFT calculations

In order to enable relatively large-scale (>> 10,000 atoms) simulations related to anode/electrolyte interfacial chemistry that leads to SEI formation, we have extended the existing ReaxFF force field parameter sets to include the descriptions of Li associated reduction reactions of EC, EMC, and VC and the description of $LiPF_6$ and Li-EC/EMC solvent binding energies for solvation structures. This ReaxFF extension was accomplished by first generating a suite of Density Functional Theory (DFT) data describing Li-associated initiation reactions for organic electrolyte species and Li and Li^+ binding energies with up to four electrolyte molecules. The DFT calculations for the organic electrolyte/Li interactions were performed using the Jaguar-code [142] using the DFT/B3LYP method and a 6-311G**++ basis set. First, we optimized the Li-binding location and subsequently a reaction scan was performed – typically by stretching a target bond – to obtain a bond distance/bond energy plot that could be used for the ReaxFF force field development.

To develop ReaxFF parameters for organic electrolyte reactions in the presence of neutral Li we performed a series of non-periodic DFT calculations. Figure **4-1** shows the results for a ring opening in ethylene carbonate (EC) by ether C – ether O bond breaking, resulting in a reduction of the EC and the formation of a radical anion. These DFT calculations are in good agreement with earlier DFT work performed by Bedrov et al. [130], showing a relatively low (12 kcal/mol) ring opening barrier and a strongly exothermic reaction. Figure **4-2** shows similar reaction scans for other organic electrolyte molecules – vinylene carbonate (VC) and ethyl methyl carbonate (EMC). We observe that the VC ring opening reaction has a higher barrier (13.6 kcal/mol) and is less exothermic than the Li/EC case. The EMC reaction has a 16 kcal/mol barrier. This ether C – ether O bond breaking reaction is exothermic which is also confirmed by Tasaki [131]. During the EMC reaction, Li moves from a mono-dentate mode to a bi-dentate mode with O.

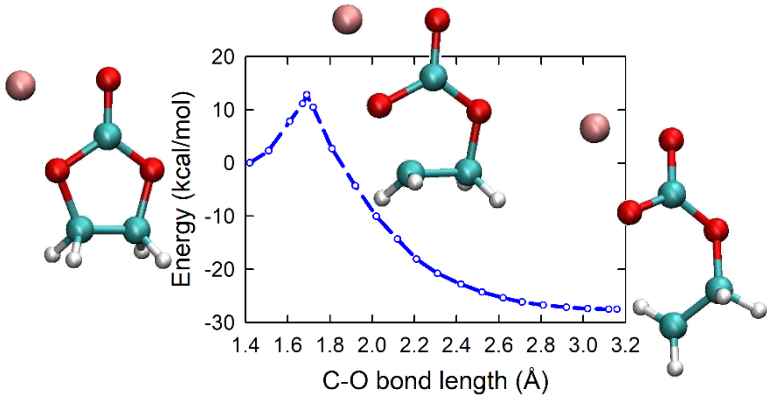

Figure **4-1**: DFT results for an ether C - ether O bond opening reaction in ethylene carbonate (EC) in the presence of neutral Li. Color scheme: C: cyan, H: white, O: red and Li: pink.

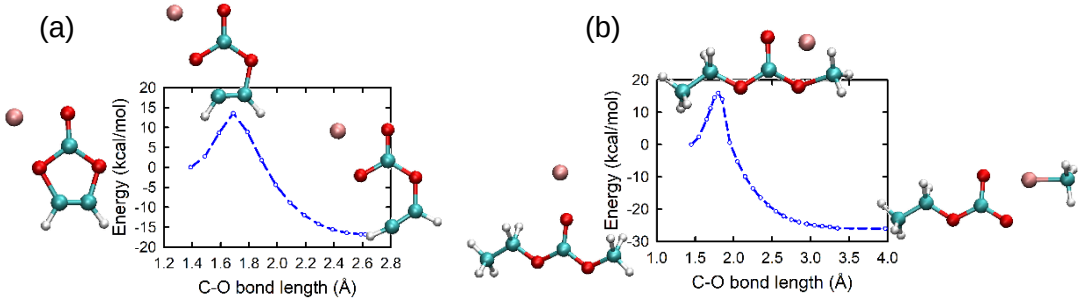

Figure **4-2**: DFT results for an ether C - ether O bond opening reaction in (a) vinylene carbonate (VC) and (b) ethyl methyl carbonate (EMC) in the presence of neutral Li.

In addition to these C-O bond scans, we also performed C-O bond opening reactions within the carbonate functional group (Figure **4-3**). The EC carbonyl C – ether O bond breaking reaction has a low barrier, indicating that the carbonate functionality becomes very mobile in the presence of a neutral Li-atom. The EMC carbonyl C – ether O bond breaking reaction, on the other hand, has a high barrier and the reaction is not exothermic. Similar to the ether C -ether O bond breaking reaction of EMC, Li moves from a mono-dentate mode to a bi-dentate mode with O.

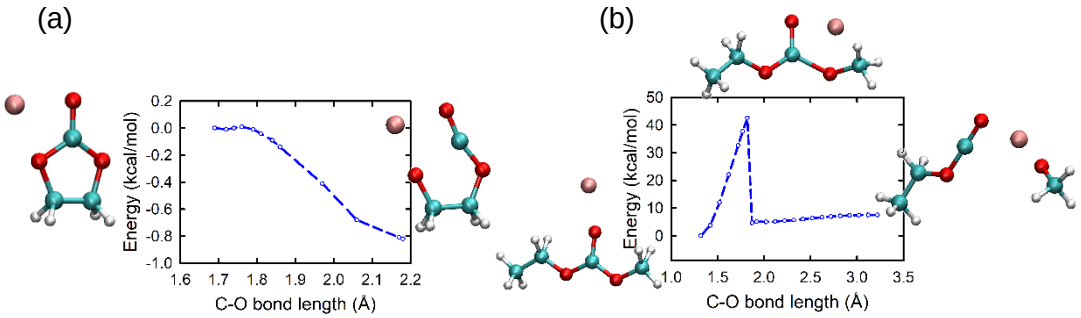

Figure **4-3**: DFT results for a carbonyl C - ether O bond opening reaction in (a) ethylene carbonate (EC) and (b) ethyl methyl carbonate (EMC) in the presence of neutral Li.

We have also calculated the total binding energies for $Li(EC)_n$ and $Li(EMC)_n$ (n=1~4) using the following expression:

$$\Delta E = E_{Li(EC/EMC)_n} - E_{Li} - nE_{EC/EMC} \tag{4.2}$$

We have considered both Li neutral and Li^+ ion for the binding energy calculations. We have also calculated total binding energies for $PF_6Li(EC)_n$ and $PF_6Li(EMC)_n$ (n=1~3) solvation structures. The results of the binding energy calculations are shown in the Appendix.

DFT calculations were also done for EC ring opening reaction in $Li(EC)_n$ (n=1~4) solvation structures to get an insight of whether solvation size has an effect on EC ring opening reaction barrier. For solvation structures that had two or more ECs, we calculated EC ring opening on EC with both the shortest and longest Li-Oc (carbonyl O) and Li-Oe (ether O) distances. The reaction barrier for $Li(EC)_1$ is 12 kcal as seen in Figure **4-1**. The barrier for $Li(EC)_2$ is 13.46 kcal/mol and

16.46 kcal/mol for EC with shortest and longest Li-Oc/Li-Oe distance respectively. The barrier for $Li(EC)_4$ is 21.24 kcal/mol and 29.85 kcal/mol for EC with shortest and longest Li-Oc/Li-Oe distance respectively. The results of the reaction scans are shown in the Appendix. From these calculations, it is established that the EC ring opening reaction barrier is a function of the size of the solvation structure.

Force field development

The calculated DFT data were added to existing ReaxFF training data for ethylene carbonate (EC)/Li interactions [64], [130] and for C/H/O general chemistry [133], [143]. Subsequently, we trained the ReaxFF C/H/O/P/F/Li atom, bond, angle and dihedral parameters with the aim to find the optimal reproduction of the DFT data. The second Li type that is to be simulated as Li^+ ion is always constrained with a +1 charge and trained against DFT data such that reactions involved with Li^+ will have a high reaction barrier that cannot be achieved in the battery operating temperature range and the reactions will be endothermic. The two types of Li parameters are created by initially duplicating the original Li atom, bond and angle parameters and then training each Li type for separate targets. The ReaxFF force field development was performed using the standalone ReaxFF program, which includes a single-parameter force field parameter optimization method that uses a parabolic search [74]. Parameter correlations were included by performing multiple cycles over all the eligible force field parameters.

Figure **4-4** shows the ReaxFF force field optimized results in a comparative fashion with DFT targets for Li -associated EC, VC and EMC reactions. The ReaxFF predicted reaction barrier for EC ring opening reaction is 6.7 kcal/mol which is below the DFT target of 12 kcal/mol. The reaction barrier for EC was intentionally kept smaller to enable reactions within the simulation time scale. Keeping the barrier slightly lower than DFT provides a better chance to get meaningful molecular dynamics statistics in a molecular dynamics accessible time scale. The ReaxFF predicted

reaction barrier for VC is 11.2 kcal/mol which is close to the DFT target of 13.6 kcal/mol. For the ether C – ether O bond breaking of EMC, the ReaxFF barrier is 20 kcal/mol which is slightly higher than the DFT barrier of 16 kcal/mol and the reaction is less exothermic compared to the DFT predicted exothermicity. For the carbonyl C – ether O bond breaking of EMC, the ReaxFF barrier is 50 kcal/mol whereas the DFT barrier is 43 kcal/mol. For this case, ReaxFF predicts an endothermic reaction like the DFT although the endothermicity is higher than the DFT prediction. Nonetheless, this deficiency of ReaxFF should not substantially affect the reaction dynamics. The trends of the reaction barriers agree well with the DFT. EC would be most likely to be reduced compared to VC. In addition, EMC having a larger barrier indicates that it is less likely to decompose within the simulation time. Our ReaxFF parameters qualitatively reproduce DFT data quite well and can be used to compare between different organic electrolyte molecules since it can capture the relative reaction barriers between the different electrolytes. This ReaxFF description can be used as a comparative tool between different organic electrolytes where the absolute rates of reaction to some extent may not be directly comparable but the relative rates are comparable.

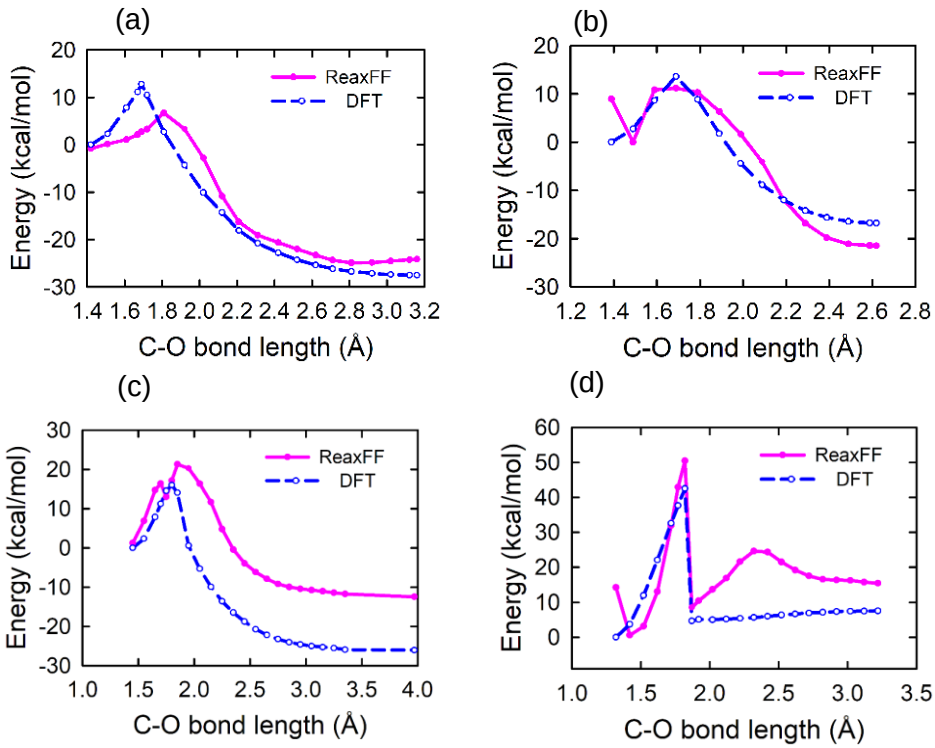

Figure **4-1**: ReaxFF vs DFT results for Li-associated decomposition reactions scans of (a) EC (ether C – ether O bond breaking), (b) VC (ether C – ether O bond breaking), (c) EMC (ether C – ether O bond breaking) and (d) EMC (carbonyl C – ether O bond breaking).

Figure **4-5** shows the ReaxFF force field result of Li^+-ion associated EC reaction in a comparative fashion with DFT reference data. Although there are discrepancies between the DFT and ReaxFF results, the reaction barrier predicted by ReaxFF is high enough that the Li^+-associated decomposition reaction of EC cannot be achieved in the battery operating temperature range and also the reaction is endothermic as intended.

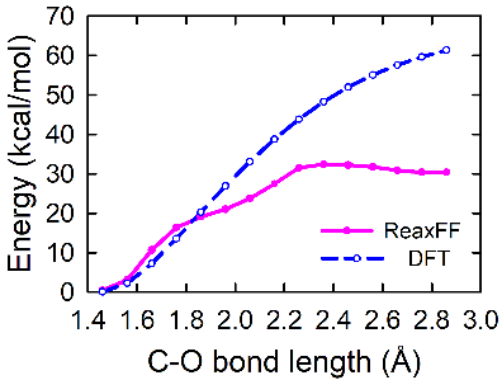

Figure **4-5**: ReaxFF vs DFT result of Li^+-associated decomposition reaction of EC.

Figure **4-6** shows the ReaxFF vs DFT energies of Li-F bond compression/stretch in a 1-fold configuration of $Li^+PF_6^-$. The ReaxFF result is in very good agreement with the DFT specially around the equilibrium bond length. The equilibrium bond length and relative energies for 2-fold configuration (see Figure **4-7** (a)) and 3-fold configuration (see Figure **4-7** (b)) of $Li^+PF_6^-$are also well predicted by ReaxFF as shown in Table **4-1**. The current force field has not yet been trained for PF_6^- to be electrochemically reduced to LiF and PF_n particles like that described by Leung[144] but work is underway to include this in the future ReaxFF force field description.

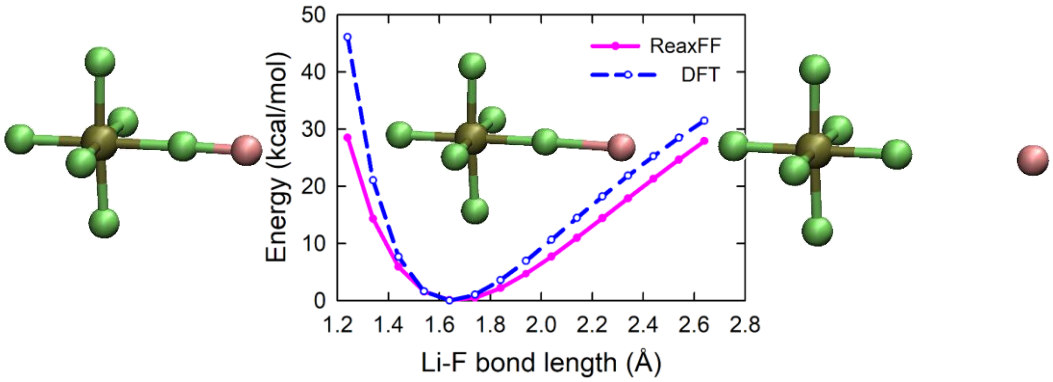

Figure **4-6**: ReaxFF vs DFT results for Li-F bond compression/stretch curves in a 1-fold $Li^+PF_6^-$. Atom color scheme: Li: pink, P: tan and F: lime.

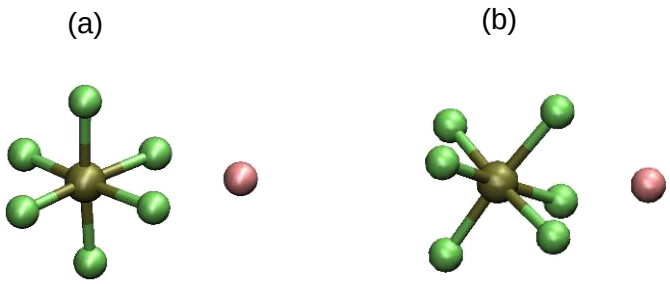

Figure **4-7**. Structures of (a) 2-fold and (b) 3-fold configuration of $Li^+PF_6^-$.

Table **4-1**: Comparison between ReaxFF, DFT and the literature for energies and equilibrium bond lengths of different configurations of $Li^+PF_6^-$

Configuration of $Li^+PF_6^-$	Energy wrt 3-fold $Li^+PF_6^-$ (kcal/mol)		LiF equilibrium bond length (Å)			LiP equilibrium bond length (Å)		
	ReaxFF	DFT	ReaxFF	DFT	Ref.[127]	ReaxFF	DFT	Ref.[127]
1-fold	14.05	16.43	1.64	1.64	1.65	3.26	3.47	3.43
2-fold	2.56	1.96	1.84	1.79	1.78	2.70	2.68	2.64
3-fold	0	0	1.97	1.91	1.89	2.53	2.48	2.43

The ReaxFF vs DFT comparison for EC ring opening in $Li(EC)_n$ (n = 2 and 4) and binding energies of Li-electrolyte and PF_6Li-electrolyte solvation structures are shown in the Appendix. ReaxFF predicts that the EC ring opening barrier increases as the solvation structure size increases. To compare the ReaxFF predicted solvent binding energies, we also used the Advanced Electrolyte Model (AEM) [145] which is a theoretical model, based on a statistical-mechanical framework, that is able to calculate numerous properties of electrolytes. Using AEM, we calculated Li^+ ion binding energies for $Li^+(EC)_n$ and $Li^+(EMC)_n$ at 273K. Also, the ReaxFF predicted binding energy trends are in good agreement with the DFT and the AEM (see the Appendix). Additionally, we compared our newly developed ReaxFF force field with the force field used in the Islam 2014 work [64]. Our current force field predicts the binding energy trends of the solvation structures better. Also, we have seen that the EC ring opening without the presence of Li has a reaction barrier of 20 kcal/mol in the Islam 2014 description. This barrier should be higher since EC should not undergo

ring opening unless reduced. Our current force field predicts a 45 kcal/mol barrier ensuring no EC will decompose without the presence of Li at the normal battery operating temperature. The Islam 2014 description predicts the carbonyl C – ether O bond breaking of EMC to be an exothermic reaction whereas both our current ReaxFF description and DFT predict it to be endothermic. This current version of ReaxFF force field has certain advantages over previous versions such as the capability of changing Li^+ ion to neutral Li and we have introduced the strong correlation between Li-solvation by EC and EC ring-opening kinetics. While the current version of ReaxFF force field has the capability of reproducing the key reactions properties and Li-solvation energies obtained from DFT, it still has certain drawbacks. The current force field is capable of describing initiation reactions that lead to SEI formation but has not yet been trained for secondary chemistry like the work performed by Bedrov et al. [130] The ReaxFF method uses EEM for charge calculation which is known for its spurious long-range charge transfer and this hinders the accurate charge description of the reduced/oxidized molecules. The eReaxFF method used by Islam and van Duin [66] uses ACKS2 for charge calculation which prevents unrealistic long-range charge smearing to a great extent.

Results And Discussion

We utilized our newly developed ReaxFF reactive force field to perform MD simulations to study the dynamics of EC/EMC/Li/$LiPF_6$ chemistry in the anode/electrolyte interface. We performed several simulation cases with different combination and concentration of electrolytes and salts in an attempt to observe Li-electrolyte solvation and reduction reactions. For all of the simulation cases we used our in-house code to place the molecules randomly in a periodic box. Next, we performed a low temperature (1 K) NVT (constant number, volume and temperature) MD-based structural relaxation simulation. Then, we carried out MD NVT equilibration at 300 K temperature to investigate the dynamic evolution of the solvation and reduction processes. All of

the MD simulations presented in this work was performed using the ReaxFF parallel implementation in the commercial Amsterdam density functional (ADF 2019.3) [146] package. The current force field allowed a low temperature – 300 K - to be used to observe the electrolyte dissociation within the simulation time scale. The temperature of the system was controlled using a Berendsen thermostat [147] with a damping constant of 100 fs. Newton's equations of motion were integrated using the velocity Verlet algorithm. A time step of 0.25 fs was used.

Effect of solvation on decomposition reaction

In order to observe how our ReaxFF reactive force field behaves in terms of reduction decomposition as a function of solvation structure size, we took three isolated systems of $Li(EC)_n$ (n=1~3) and performed structural relaxation simulations followed by MD NVT simulations at 300 K. For each solvation structure size, we took ten samples with the same initial geometry but with a different set of random velocities assigned as the initial velocity distribution. And during the course of the simulation the velocities equilibrated. Due to different trajectories, reactions occurred at different MD time. A configuration that allowed the atoms to move in the right position presented the quickest reaction. We, then, calculated means and standard deviations of the simulation times required for an EC ring opening reaction to occur for each solvation structure size and a corresponding bar graph is shown in Figure **4-8**. It can be seen from the graph that as the size of the solvation structure increases, the average time required for an EC ring opening reaction increases. The standard deviations between each sample for all of the solvation structure sizes are relatively large. However, a bigger sample size might be able to lower the standard deviations. In order to verify the abovementioned outcomes, we also calculated the energy barriers for EC decomposition reactions for four solvation structures of $Li(EC)_n$ (n=1~4). Reaction barriers are calculated from reaction pathways enforced by applying a biasing potential in between the atom pair of interest to drive the reaction along the intended reaction coordinates. This additional biasing

potential is added to the system that is intended to stretch or compress bonds at a pre-defined rate such that this additional energy can help achieve the energy to cross the reaction barrier. The biasing potential has the following form,

$$E_{biased} = f_1\left(1 - e^{f_2\left(r_0 - r_{ij}\right)^2}\right) \tag{4.3}$$

where f_1 and f_2 are force constants, and r_{ij} is the distance between atom pair of interest and is varied along the reaction coordinate. The potential energy distributions of the reaction scans obtained from ReaxFF are shown in Figure **4-9**. The biasing potential is subtracted from the potential energy shown. It can be seen that as the number of EC around Li increases, the EC ring opening reaction barrier increases. The reaction barriers are 5, 9, 10 and 14 kcal/mol for EC ring opening in $Li(EC)_n$ (n=1~4) respectively. For the $Li(EC)_1$ case, The Li is in bidentate mode with O atoms. Li reduces EC and the ring opening reaction occurs by the ether O - ether C bond breaking. For the $Li(EC)_2$, $Li(EC)_3$ and $Li(EC)_4$ cases, the Li initially takes the monodentate mode with carbonyl O of all ECs. For an EC ring opening to occur, Li is moved toward a bidentate position with the EC of interest. After ring opening is complete, the Li remains in bidentate mode with the open ring EC. For the $Li(EC)_4$ case, while Li is pushed toward a bidentate mode with the EC of interest Li becomes uncoordinated with another EC since Li likes to be 4 coordinated.

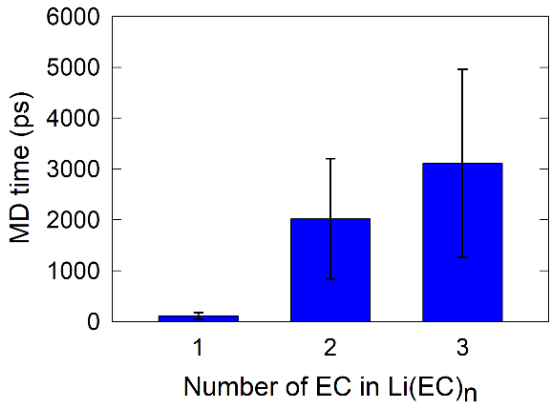

Figure **4-8**: Means and standard deviations of the required simulation times for decomposition reaction as a function of number of EC in $Li(EC)_n$.

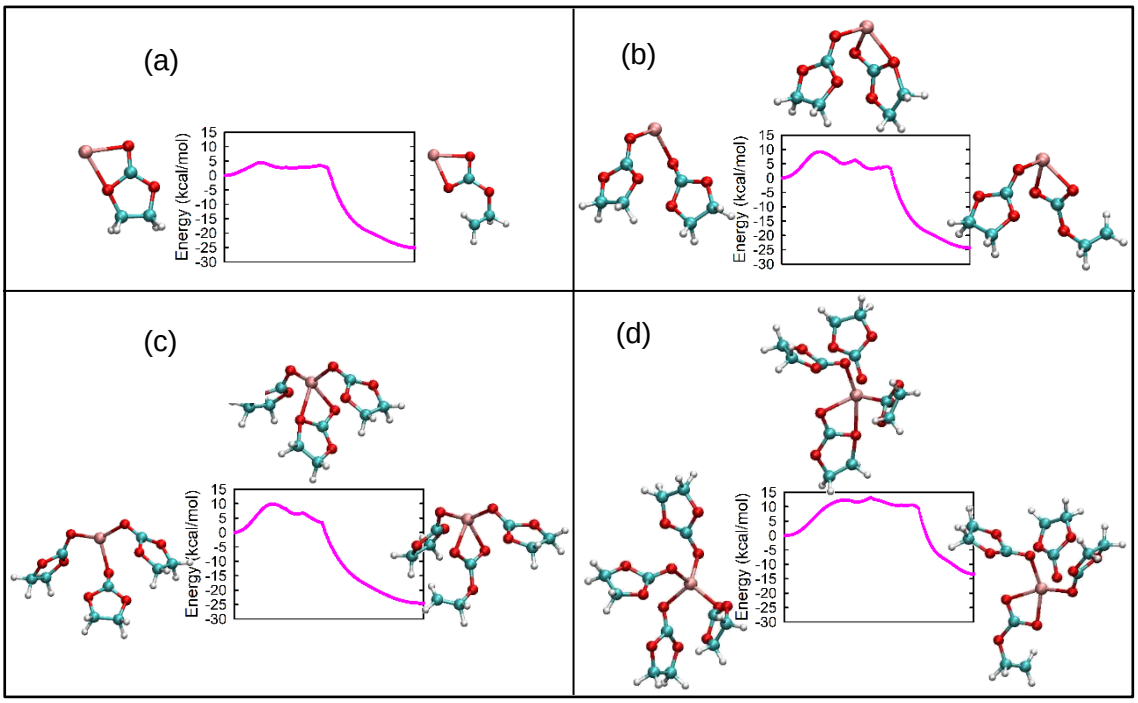

Figure **4-9**: Reaction scans of EC ring opening in $Li(EC)_n$ for (a) n=1, (b) n=2, (c) n=3 and (d) n=4.

Neutral Li vs Li cations

Li can reduce EC and EC undergoes reduction decomposition reaction. On the other hand, a Li^+ cation cannot donate an extra electron to EC and thus, cannot reduce EC. In order to test the second Li parameter set, that describes the Li^+ ion, in our ReaxFF force field, we have performed MD NVT simulations on a Li^+ bound EC to observe whether any EC ring opening reaction occurs. Even at 600 K in a 2.5 ns long MD simulation, no ring opening reaction was seen as intended. To further verify this, a reaction scan was performed to obtain the reaction barrier of EC ring opening in Li^+EC. The reaction scan is shown in Figure **4-10**. It can be seen that the reaction is endothermic and the reaction barrier is 33kcal/mol. Thus, the Li cation description turned out as we intended.

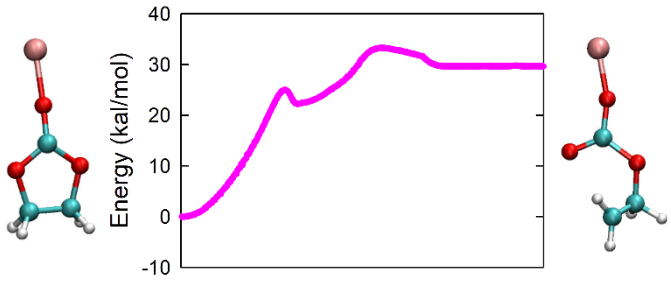

Figure **4-10**: Reaction scans of EC ring opening in Li^+EC.

An electrolyte solution typically contains $LiPF_6$ salt dissolved in a mixture of organic solvents. Ideally, $LiPF_6$ salt is dissolved as Li^+ and PF_6^- by the solvent for most of the time. In this next test we simulated $LiPF_6$ separately by using both Li parameter sets. For the second parameter set, we constrained the Li with a +1 charge and PF_6 with a -1 charge. Ideally an EC coordinated with a Li of a $LiPF_6$ ($Li^+PF_6^-$) should not undergo ring open reaction since Li^+ cannot reduce EC. We have performed a reaction scan on EC ring opening when $LiPF_6$ is involved using both of our Li parameter sets. The reaction scans are shown in Figure **4-11**. The reaction barrier using the Li-neutral atom type is around 16 kcal/mol which means this reaction can occur within the battery operating temperature range. Using Li-cation atom type the reaction barrier is around 35 kcal/mol

which is more realistic since EC should not ring open in the presence of $Li^+PF_6^-$. Thus, $LiPF_6$ modeling should be done with the Li-cation atom type.

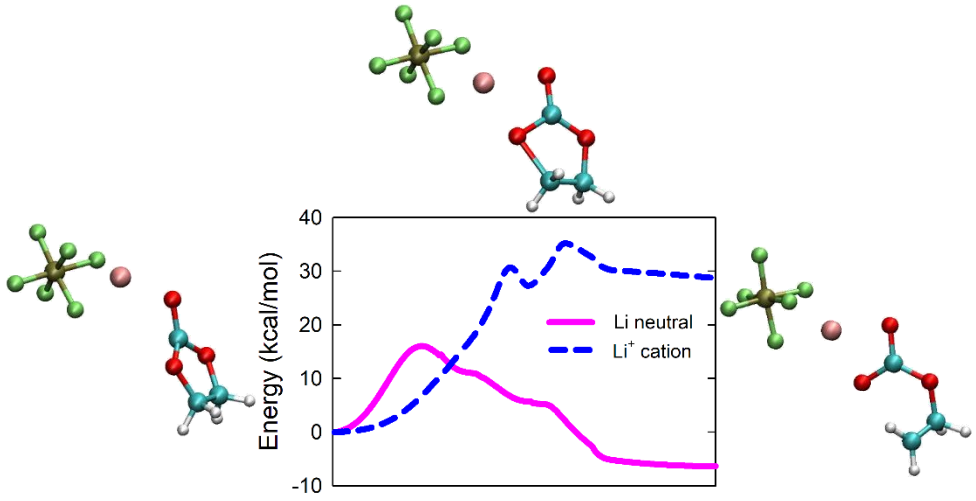

Figure **4-11**: Reaction scans of EC ring opening in $LiPF_6$-EC using both types of Li parameter sets.

MD simulations of different electrolyte systems

In this section, we will discuss results of ReaxFF MD simulations performed on various systems of electrolyte solvents and salts.

3 EC 7 EMC 1 Li^+ system

We took 3 EC molecules, 7 EMC molecules and 1 Li^+ ion in a periodic box of 30 Å × 30 Å × 30 Å (Figure **4-12** (a)). This constitutes a very low density of the electrolyte solution and the Li concentration is about 0.06 M which is very low compared to typical Li ion batteries. This low Li concentration was taken to observe a single Li solvation without the effects of other Li or Li salts. We ran an MD NVT simulation at 300 K temperature for an MD time of 2.5 ns and the final structure is shown in Figure **4-12** (b). Throughout the course of the simulation, Li^+ solvates with the EC and EMC electrolyte solvents and moves from one solvation structure to another. It is seen that Li^+ ion coordinates mostly with carbonyl O of EC and EMC, but in some cases coordinates with the ether O as well. Snapshots of different solvation structures observed throughout the course

of the simulation are shown in Figure **4-13**. As expected, no decomposition reaction takes place. If the Li^+ cation is converted to the neutral Li atom type, reactions are expected to happen and to demonstrate this we have taken snapshots of the simulation trajectory at 121 ps and 2.5 ns and converted the Li^+ ion to Li and performed reaction scans on EC ring opening. Figure **4-14** (a) shows the solvation structure at 121 ps. The Li is coordinated to carbonyl O of EC and EMC. Figure **4-14** (b) shows the reaction scan of EC ring opening. The Li is moved toward a bidentate mode with EC to favor the ring opening reaction. It is seen that the reaction barrier is around 7 kcal/mol for EC ring opening. Similarly, Figure **4-15** (a) shows the solvation structure at 2.5 ns. The Li is solvated with a total of four electrolyte solvent molecules. Li is coordinated with carbonyl O of two ECs, one EMC and ether O of one EMC. Figure **4-15** (b) shows the reaction scan of EC ring opening. In this case the reaction barrier is around 14.7 kcal/mol for EC ring opening. Thus, both of these reactions can be expected at the current temperature. After 2.5 ns MD simulation with Li^+, we then converted the Li^+ to a Li and continued the simulation at 300 K. An EC ring opening reaction is, indeed, seen and the path leading towards this reaction is shown in Figure **4-16**. After the Li^+ ion to Li atom conversion, an EMC de-solvates from the $Li(EC)_2(EMC)_2$ solvation structure. Then, Li forms a bidentate mode with an EC which forces another EMC to de-solvate. Finally, EC ring opens. The de-solvation of some solvent molecules makes the EC ring opening more favorable since the final solvation structure just before the EC ring opening is a smaller one.

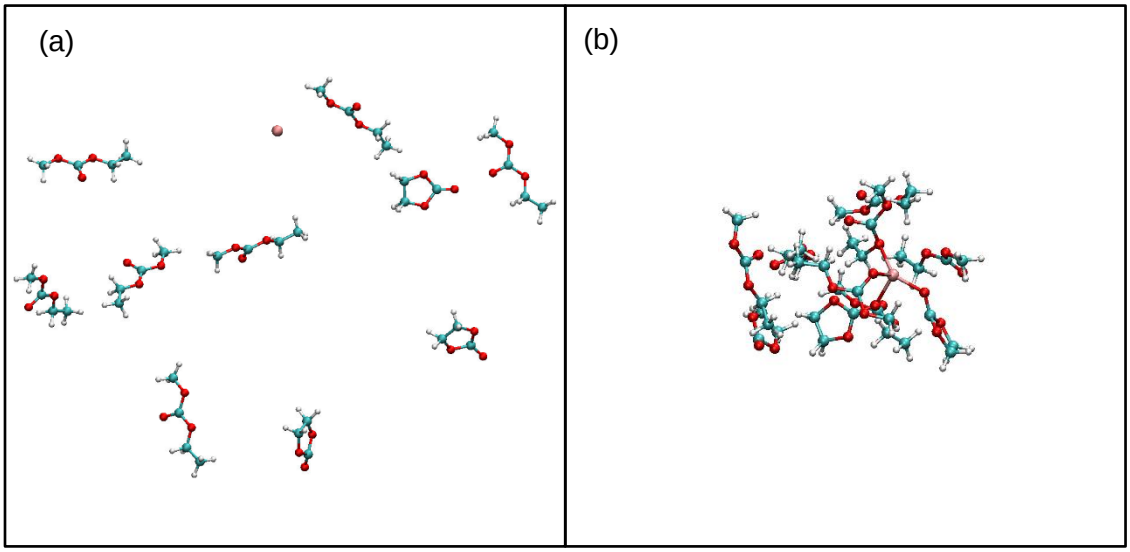

Figure **4-12**: Configuration of 3 EC 7 EMC 1 Li^+ system at (a) t = 0 and (b) t = 2.5 ns.

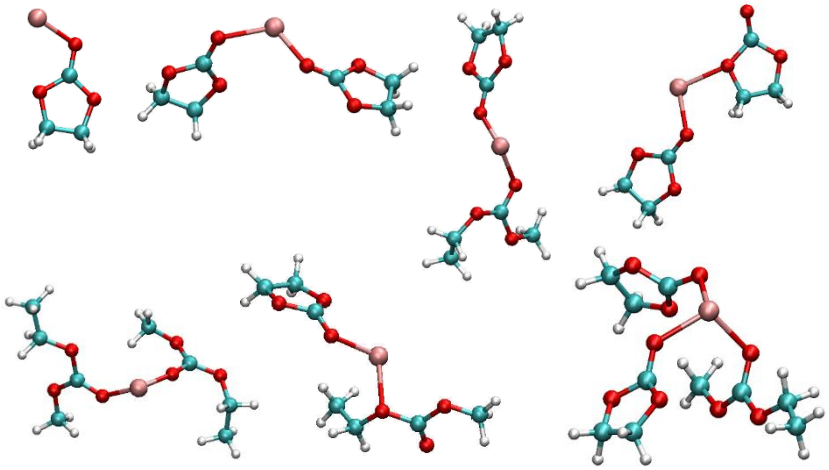

Figure **4-13**: Different solvation structures seen throughout the simulation of 3 EC 7 EMC 1 Li^+ system.

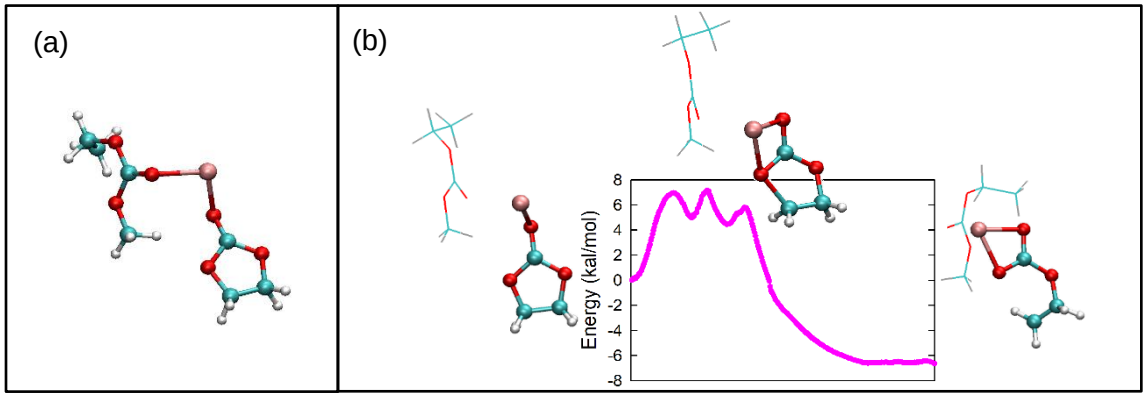

Figure **4-14**: (a) Solvation structure and (b) reaction scan of EC ring opening from the solvation structure at 121ps of the 3 EC 7 EMC 1 Li^+ system.

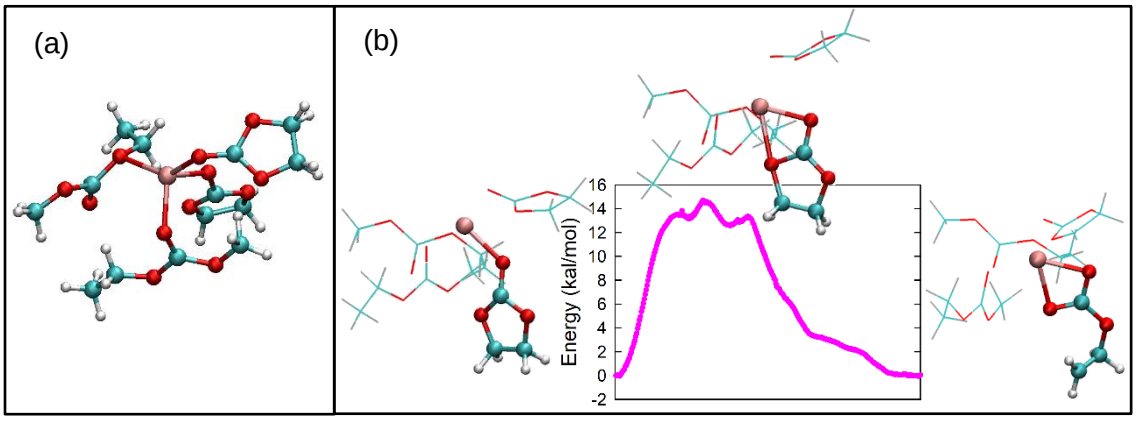

Figure **4-15**: (a) Solvation structure and (b) reaction scan of EC ring opening from the solvation structure at 2.5 ns of the 3 EC 7 EMC 1 Li^+ system.

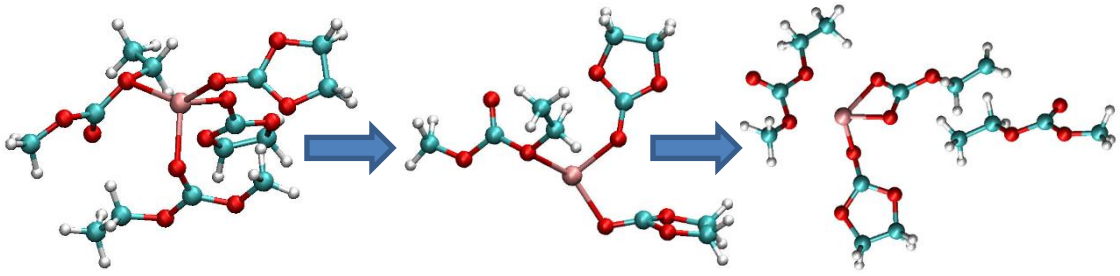

Figure **4-16**: Path leading to Li de-solvation and EC ring opening reaction in the 3 EC 7 EMC 1 converted-neutral Li system.

30 EC 70 EMC 3 Li^+ system

Now we took a bigger system with 30 EC molecules, 70 EMC molecules and 3 Li^+ ions in a periodic box of 40 Å × 40 Å × 40 Å (Figure **4-17** (a)). This system corresponds to a total of 1353 atoms and a density of 0.26 g/cm^3. The concentration of Li in this system is about 0.08 M. Our goal of this simulation is to observe whether the similar solvation and reaction processes take place in a bigger system. The solvation structures formed by each Li^+ supposedly will provide an idea of preferential solvation structures. We ran an MD NVT simulation at 300 K temperature for an MD time of 1.66 ns and the final structure is shown in Figure **4-17** (b). Similar to the previous case, Li^+ solvates with the EC and EMC electrolyte solvents and moves from one solvation structure to another throughout the course of the simulation. A snapshot taken from the simulation trajectory at 1.66 ns shows that one Li^+ solvates to form $Li^+(EC)_1(EMC)_1$ (Figure **4-18** (a)) and the other two Li^+ ions form $Li^+(EC)_3$ (Figure **4-18** (b)). To observe reduction chemistry, we have chosen to convert one out of the three Li^+ ion to a Li atom. If Li^+ from one of the $Li^+(EC)_3$ structure is converted and the MD simulation is continued, we see that an EC ring opening reaction is seen after 139 ps as shown in Figure **4-19**. In another case, we converted Li^+ from the other $Li^+(EC)_3$ structure and continued the simulation. In this case, as shown in Figure **4-20**, the $Li(EC)_3$ structure further solvates with another EC and the Li becomes four coordinated. Li solvates with the ether O of this fourth EC and forms $Li(EC)_4$. Finally, in only 1.6 ps the fourth EC ring opens but this time the carbonyl C – ether O bond breaks. According to DFT, Li-bound EC can indeed break carbonyl C – ether O bond break since this reaction has a very low barrier (Figure **4-3** (a)).

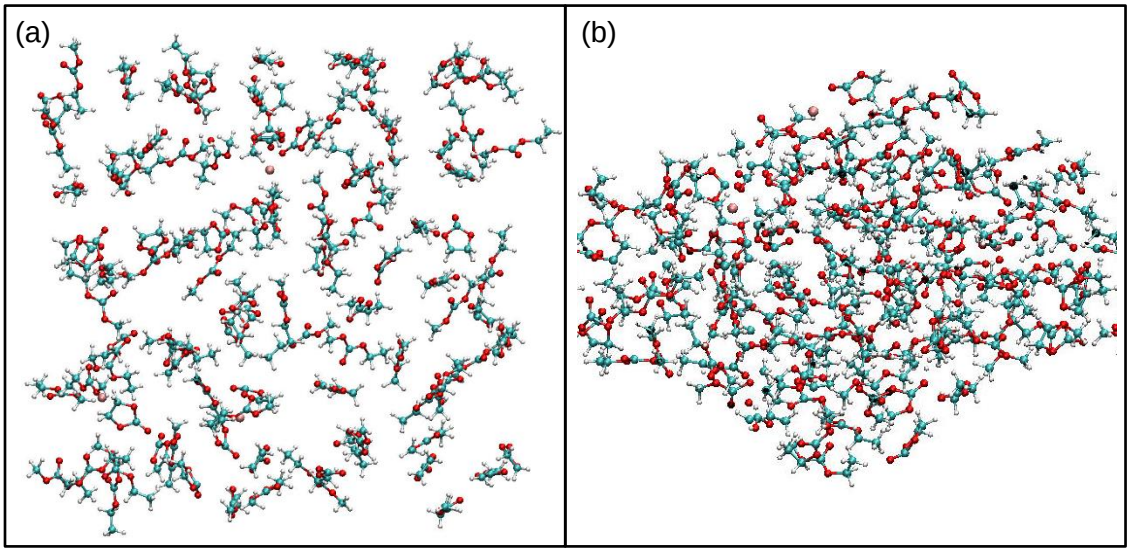

Figure **4-17**: Configuration of 30 EC 70 EMC 3 Li^+ system at (a) t = 0 and (b) t = 1.66 ns.

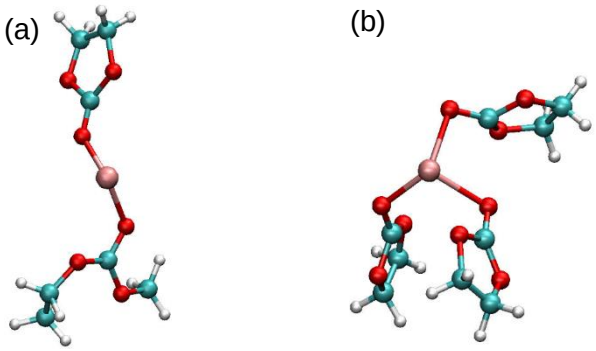

Figure **4-18**: Solvation structures (a) $Li^+(EC)_1(EMC)_1$ and (b) $Li^+(EC)_3$ observed at 1.66 ns of the simulation of 30 EC 70 EMC 3 Li^+ system.

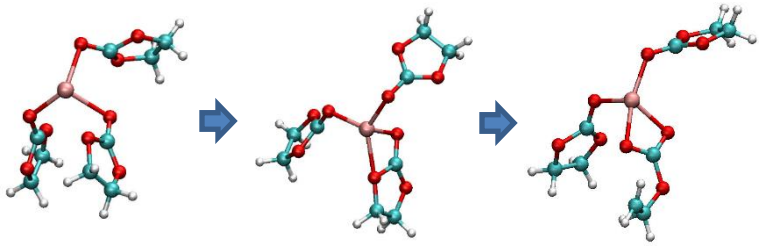

Figure **4-19**: Path leading to EC ring opening reaction (case 1) in the 30 EC 70 EMC 3 Li^+ system with 1 converted neutral Li.

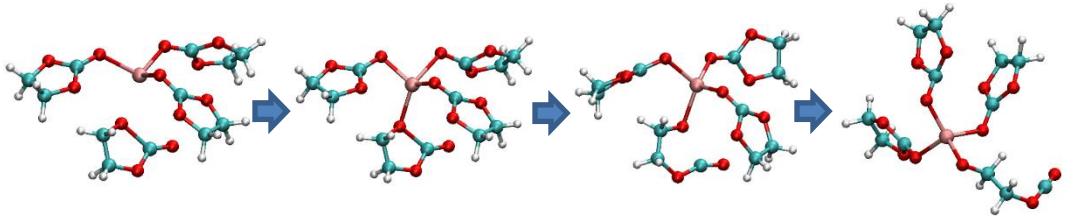

Figure **4-20**: Path leading to EC ring opening reaction (case 2) in the 30 EC 70 EMC 3 Li^+ system with 1 converted neutral Li.

3 EC 7 EMC 1 $Li^+PF_6^-$ system

Now, in order to observe how $LiPF_6$ behaves in solvation, we took a low-density system of 3 EC molecules, 7 EMC molecules and 1 $LiPF_6$ salt molecule in a 30 Å × 30 Å × 30 Å periodic box as shown in Figure **4-21** (a). A 2.5 ns MD NVT simulation shows that the Li^+ cation remains associated with the PF_6^- anion the whole time but the Li^+ ion along with the PF_6^- moves from solvation structure to other solvation structures. In most cases, the Li^+ is solvated with the carbonyl O of one EC (Figure **4-22** (a)), the carbonyl O of one EMC (Figure **4-22** (b)) or carbonyl O of one EC and ether O of one EMC (Figure **4-22** (c)).

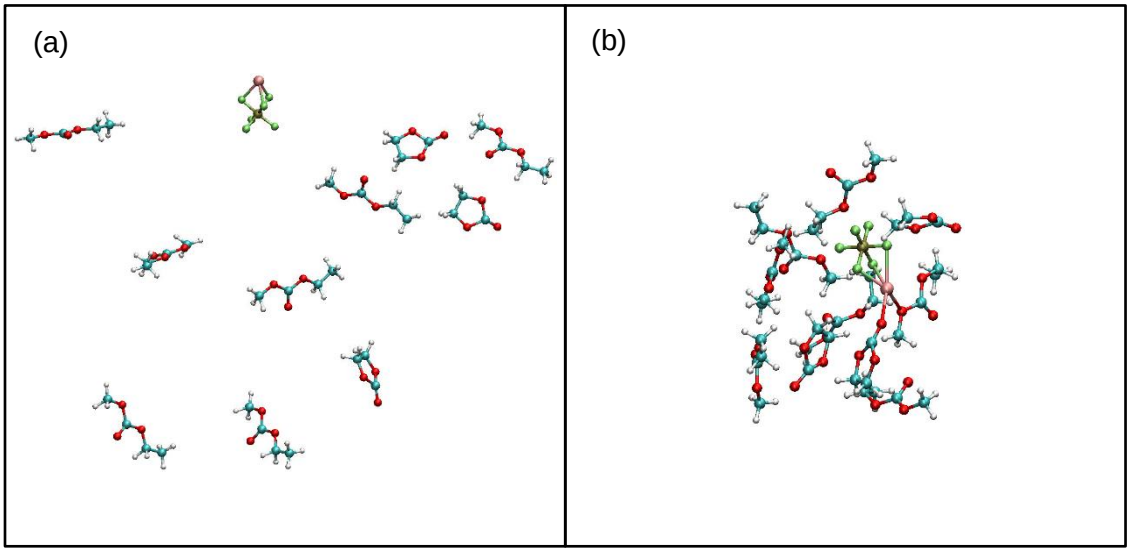

Figure **4-21**: Configuration of 3 EC 7 EMC 1 $Li^+PF_6^-$ system at (a) t = 0 and (b) t = 2.5 ns.

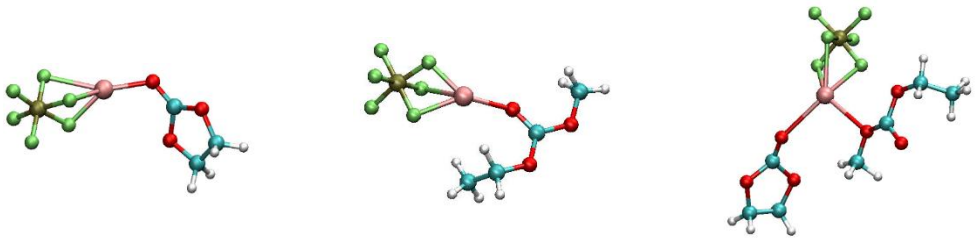

Figure **4-22**: Different solvation structures seen throughout the simulation of 3 EC 7 EMC 1 $Li^+PF_6^-$ system.

30 EC 70 EMC 3 $Li^+PF_6^-$ system

Now, we have taken a bigger system with 30 EC, 70 EMC and 3 $LiPF_6$ molecules in a 40 Å × 40 Å × 40 Å periodic box as shown in Figure **4-23** (a). This system was simulated for an MD time of 1.84 ns and the final structure is shown in Figure **4-23** (b). In this system we mostly see $PF_6^-Li^+(EC)_1$ solvation structure similar to Figure **4-22** (a). Li^+ ion being three coordinated with PF_6^- hinders its ability to solvate with higher number of electrolyte solvent molecules. The solvation structures with $LiPF_6$ described by Ong et al. [32] had coordination of 1 or 2 between Li and PF_6 making room for up to three solvent molecules around the Li.

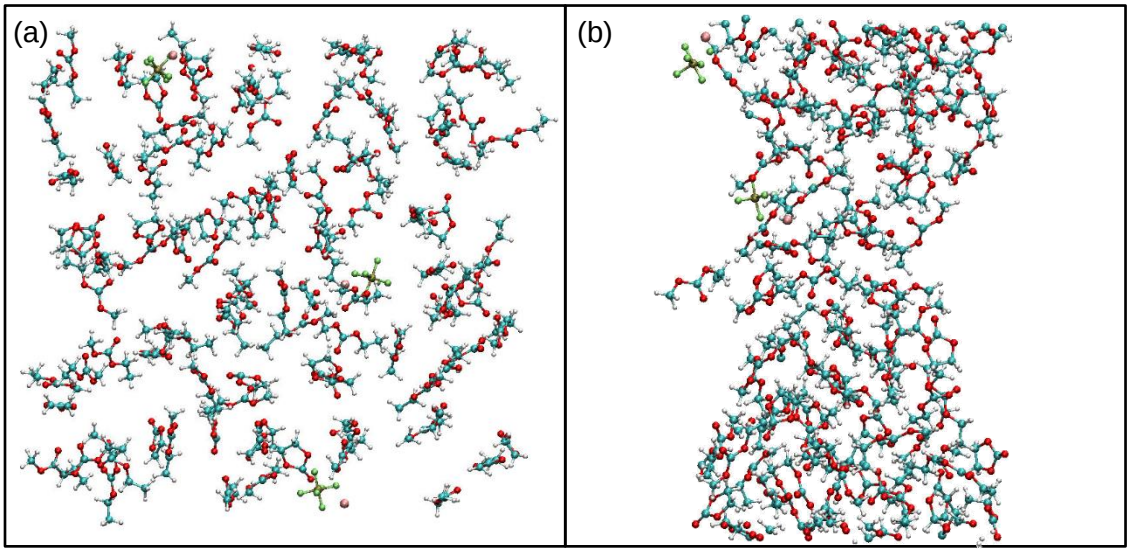

Figure **4-23**: Configuration of 30 EC 70 EMC 3 $Li^+PF_6^-$ system at (a) t = 0 and (b) t = 1.84 ns.

Conclusion

We have successfully developed a ReaxFF reactive force field that can simulate the kinetics of the anode/electrolyte interfacial chemistry, specifically, the events leading to the formation of SEI. Our ReaxFF predicted results for the organic electrolyte decomposition reactions and binding energies of Li with electrolyte molecules are in good agreement with the trend of the DFT data. Our simulations show Li-electrolyte solvation, solvent exchange, de-solvation and finally electrolyte reduction decomposition which is the initial step towards SEI formation. In our simulations, Li predominantly solvates with up to three electrolyte solvent molecules, but occasionally it solvates with up to four molecules. Our force field correctly distinguishes between the reactivity of a neutral Li atom and a Li^+ cation. We find that the Li^+ atom type cannot initiate a reduction reaction while a neutral Li atom can, thus providing a foundation for a ReaxFF simulation setup where Li-cations can be transformed into neutral Li atoms through a Monte Carlo type scheme that takes into account proximity to the anode and the anode voltage. We found that the size of the solvation structure has a significant effect on the reduction decomposition of electrolytes. The reaction barrier increases as the size of the solvation structure increases. This dependence of reaction kinetics on solvation structure indicates the relevance of methods like ReaxFF – which have sufficient time and length scales to capture both solvation structure and sample chemical events – for battery SEI structure evaluation.

Supplementary Material

See the Appendix for additional DFT results, additional ReaxFF force field optimization results and binding energies of solvation structures.

Chapter 5

Development and applications of an eReaxFF Force Field for graphitic systems

This chapter is part of a manuscript under preparation, authored by Md Jamil Hossain, and Adri C. T. van Duin. MJH optimized the eReaxFF parameters and performed the simulations, under the supervision of ACTvD.

Introduction

One of the advancements of the lithium-ion battery technology is directly linked to the emergence of graphitic materials, such as carbon nanotubes, nanoribbons, graphene, etc., as battery electrode due to their properties such as high electron conductivity, high surface area for intercalation of ions, high surface-to-volume ratio, shorter ionic-diffusion distance, broad electrochemical window, thermal and chemical stability etc. [148] Li-intercalated graphene with a stoichiometry of Li_2C_6 has a specific capacity of 540 mAh/g whereas Li-intercalated graphite in a stoichiometry of LiC_6 has a specific capacity of only 372 mAh/g [149]; The specific capacity can be enhanced up to 730 mAh/g and 784 mAh/g, respectively, by introducing carbon nanotubes and fullerenes between the layers of multilayer graphene. Nitrogen or boron-doped graphene on the other hand exhibit 1043 mAh/g and 1549 mAh/g, respectively [15]. Several studies on graphene-based anodes have been reported in the literature [15], [150], [151]. The aspects of using graphene as battery anodes have been detailed in the review articles [152], [153].

A real-life graphene anode is not free from imperfections. Graphene lattice imperfections such as Stone-Wales defect, line defect, foreign atom defect, sp^3 connection between two graphene layers of a bilayer graphene are quite common [154]. Imperfections create curvature in graphene.

These imperfections deteriorate the properties of graphene since they alter the electronic, optical, thermal, and mechanical properties of the solid. However, these local properties can be tailored to achieve useful functionalities for some applications.

Molecular dynamics (MD) simulations provide detailed observation of the interactions at the atomic level, which lead to better understanding of material behavior. ReaxFF reactive force field based MD simulations [63] can model chemical reactions based on the bond length-bond order relationship [67], [69] and can model larger systems over much longer timespans than ab initio methods. ReaxFF has been applied to a wide range of systems, including but not limited to Li-ion batteries [32], [115], [130], Li–S batteries [25], [64], graphitic materials [143], [155]. The eReaxFF method [65] is an extension of the ReaxFF method with a description of an explicit pseudo-classical electron-like particle. This method has been applied to simulate electronic motion in carbon-based-systems [65], lithium-electrolyte systems [66] and was recently extended to Ag metal systems [156] and polyethylene electrical breakdown [157].

In this manuscript, we describe the development and application of the eReaxFF force field for graphitic anodic systems. We demonstrate the quality of the force field in simulating the conduction behavior in pristine and imperfect graphitic systems. We further demonstrate the force field's capability of simulating electron leakage from graphene to exposed Li^+ ions and the eventual initiation of Li-metal-plating on graphene surface.

Method

eReaxFF method is an extension of the standard ReaxFF method which incorporates a pseudo-classical explicit electron scheme. The general expression of the eReaxFF energy is

$$E_{system} = E_{bond} + E_{over} + E_{under} + E_{lp} + E_{val} + E_{tor} + E_{vdWaals} + E_{coulomb} + E_{nucl-elec} + E_{elec}$$

where partial energy contributions include bond, over-coordination penalty and under-coordination stability, lone pair, valence, torsion, non-bonded van der Waals, Coulomb, electron-nucleus interactions and electron-electron interactions respectively. All the many-body bonded interaction and nonbonded interaction terms of ReaxFF are retained with modifications made to the over-coordination penalty, under-coordination stability and lone pair terms to incorporate explicit electrons. In addition, new energy functionals are included to account for electron-nucleus and electron-electron interactions.

In eReaxFF, the nuclei are treated as point charges and electron as Gaussian wave $\psi \infty \exp\left(-\alpha\left(r-r'\right)^2\right)$. This Gaussian wave interacts with the nuclei though a pairwise interaction described as

$$E_{nucl(i)-elec(j)} = -\frac{1}{4\pi\varepsilon_0}\beta\sum_{i,j}\frac{Z_i}{R_{ij}}erf\left(\sqrt{2\alpha}R_{ij}\right) \tag{5.1}$$

where Z_i is the nuclear charge, R_{ij} is the distance between the electron and nucleus, α and β are constants that depends on the atom type. The electron is represented as an additional particle that carries a -1 charge; electron particles interact with all other atomic charges using the same shielded Coulomb interaction as in standard ReaxFF. The number of electrons associated with any single atom is determined by the following equation

$$n_{el} = \exp\left(-p_{val}.R_{ij}^2\right) \tag{5.2}$$

where R_{ij} is the distance between the atom-center and the electron and p_{val} is a Gaussian exponent. This enables the electron particle to hop between atoms, thus allowing electron transfer processes to be modeled by eReaxFF.

In ReaxFF, the bonded and non-bonded interactions are calculated independently, that is, the valency and number of lone pair electrons of an atom type are independent of atomic charge. Thus, the bond orders are fully de-coupled from the charges - as such, a hydrogen ion (H^+) is considered capable of forming bonds. eReaxFF, on the other hand, fixes this shortcoming by introducing variable valency and number of lone-pair electrons of an atom depending on the proximity of explicit electrons. The bond orders and over-coordination, under-coordination and lone pair energies are calculated based on the corrected valence electrons. Removing an electron from an atom decreases the atom's valency and consequently increases the over-coordination of an existing bond, resulting in a larger over-coordination energy penalty, and therefore reduces the bond order associated with that atom and weakens the bond. In contrast to ReaxFF, this scheme has enabled the eReaxFF method to counteract the formation of unphysical bonds such as H^+–H^+ due to the higher over-coordination penalty stemming from the loss of valence electron from the H atom. To compute atomic charges, eReaxFF uses the atom-condensed Kohn–Sham density functional theory approximated to the second order (ACKS2) charge calculation scheme instead of the electronegativity equalization method (EEM) or the charge equilibrium method (QEq) used by most ReaxFF force fields.

Most eReaxFF force fields described a system with one extra electron on a molecule. However, Evangelisti et al. [156] recently developed an eReaxFF force field for Ag-systems where every neutral silver atom is described as a positive Ag^+ cation paired with an electron in a quasi-Drude fashion. The present eReaxFF description of graphitic system for battery anode application is similarly described where every atom in the system is paired with an extra electron. One advantage of this concept is that the charge distribution, atomic dipole and polarization behavior can be described very accurately. In the graphitic system, the neutral C atom is simulated as a C^+

and e^- pair since the extra electron on C^+ increases its valency from 3 to 4 matching that of neutral C valency.

In the current eReaxFF force fields, the mass of the electron particles is considered 1 amu in order to allow femto-second MD timesteps. Our simulation results for graphene/graphite electron conductivity, obtained using a 1 amu mass for electron, are qualitative in nature. Our initial target is to get the qualitative trends of electron conduction right, and then move on to quantify the results and compare with actual values since at the end a proper description of electron conduction is desired. Using a smaller mass for electrons or using path integral molecular dynamics (PIMD), quantitative results can be expected.

Force field training

The eReaxFF force field parameters were developed and trained with an aim to reproduce quantum chemistry-based data from the literature. Parameter optimization was conducted using a successive one-parameter search technique [74] to minimize the following expression for the error:

$$error = \sum_{i=1}^{n} \left(\frac{x_{i,lit} - x_{i,eReaxFF}}{\sigma_i} \right)^2 \tag{5.3}$$

where $x_{i,lit}$ and $x_{i,eReaxFF}$ are the target quantum chemistry/experimental data and eReaxFF values of the i^{th} entry of the force field training set and σ_i is the inverse weight that determines how accurately that particular data needs to be fitted with the QC/experimental data. The summation of all errors in the training set provides the overall error, which is one of the measures of the quality of the force field.

The C atom and C-C bond parameters of the force field have been trained against quantum chemistry-based data describing electron affinities and ionization potentials of several polycyclic aromatic hydrocarbons and graphene. The QC data are obtained from references [158]–[169]. The electron affinity is defined as

$$EA_x = E_x - E_x^- + E_{el} \tag{5.4}$$

where E_x and E_x^- are the energy of the molecule in a neutral state and in a state with an additional electron, respectively, and E_{el} is the energy of an electron. A positive value of electron affinity would indicate that the molecule would like to accept an additional electron. The ionization potential is similarly defined as

$$IP_x = E_x - E_x^+ - E_{el} \tag{5.5}$$

where E_x^- is the energy of the molecule in a state with one fewer electron and the other terms remaining the same. A positive value of ionization potential would indicate that the molecule would like to lose an electron. Figure **5-1** (a) shows the different anions of polycyclic aromatic hydrocarbons (PAHs), C-60 bucky ball and graphene. All C atoms are represented as a C^+/electron$^-$ pair. One additional electron is included with every compound to represent the anionic state of that compound. The bar chart from Figure **5-1** (b) shows the comparison of the electron affinities obtained by eReaxFF with the target data from literature. Although, eReaxFF over predicts the value of the electron affinities, the overall qualitative trend agrees well with the QC data.

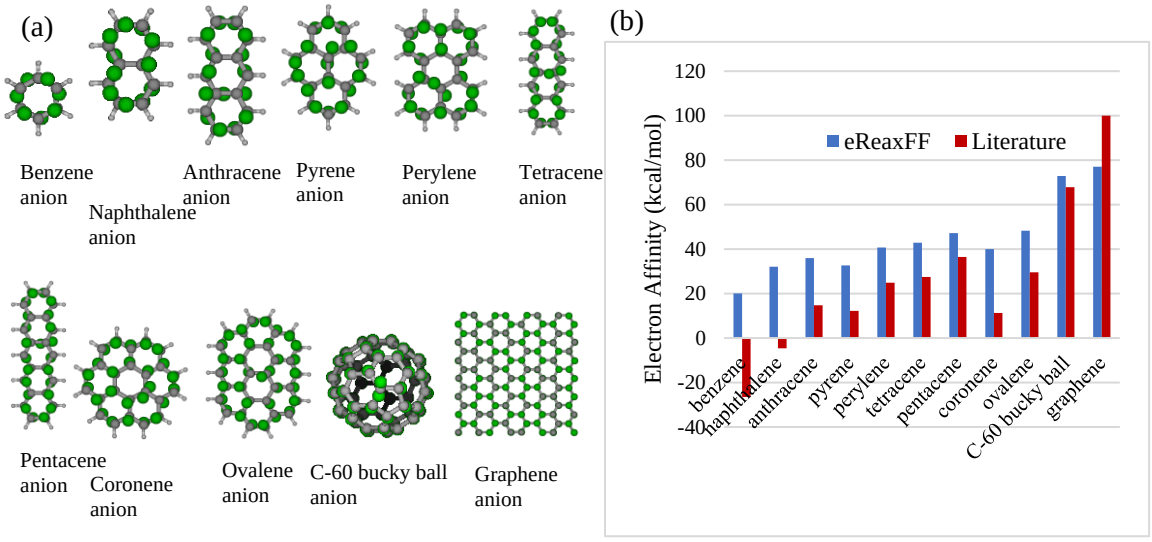

Figure **5-1**: (a) Anions of polycyclic aromatic hydrocarbons (PAHs), C-60 bucky ball and graphene. Color scheme: C^+: grey, electron: green. (b) Bar chart of eReaxFF and literature comparison of electron affinities of PAHs, bucky ball and graphene.

The force field parameters have also been trained against density functional theory (DFT) calculated equation of states for graphite compression/expansion in both the ab-direction as well as the c-direction obtained from Srinivasan et al. [143] As shown in Figure **5-2**, the eReaxFF results agree quite well with the DFT especially around the equilibrium ensuring that graphite would have a proper C-C bond length in the graphene layer and a proper spacing between layers. This has been done in such a way that the C-C pair would have a van der Waals repulsion in the c-direction while maintaining a strong bond in the ab-direction.

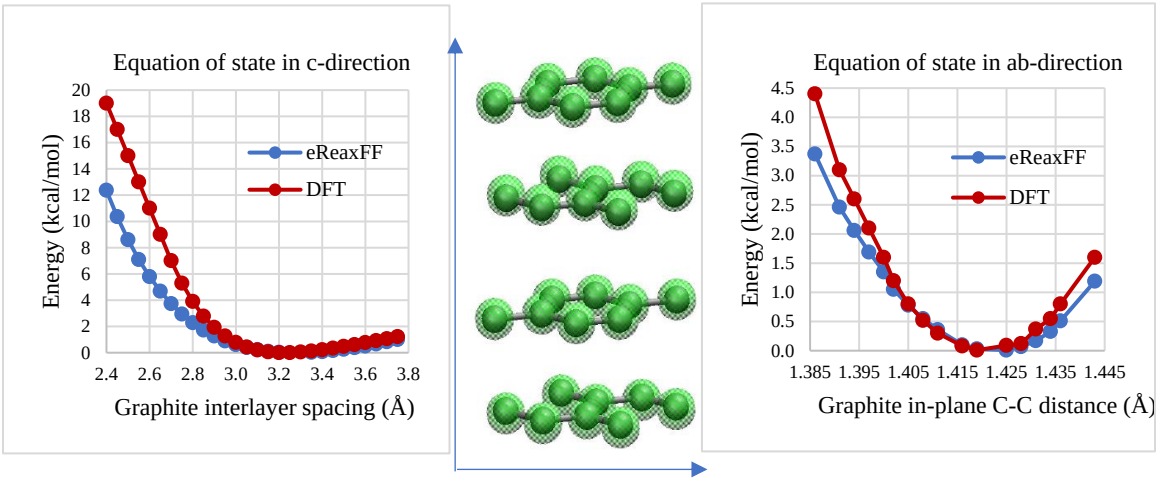

Figure **5-2**: Graphite equation of states in c-direction and ab-direction. Color scheme: C^{+}: grey, electron: transparent green.

From conventional wisdom, it is known that graphite is an electrical conductor in the ab-direction where as an electrical insulator in the c-direction. In order to maintain graphene in-plane electrical conductivity and restrict out-of-plane electrical conductivity, the electron transition barrier has been kept low (~1.5 kcal/mol) to allow easy transition of electrons in the plane of graphene layers while the barrier for electron transition from one graphene layer to another layer has been kept relatively high (~6.5 kcal/mol). By optimizing the carbon-electron van der Waals parameters as well as the electron Gaussian exponent and Taper radius, we have successfully managed to limit the out-of-plane electron transition while retaining the proper in-plane electron mobility.

In order to avoid graphene curvature formation, we have introduced DFT data describing the rotation of C-C=C-C torsion angle of 2-butene and trained the C-C-C-C dihedral parameters. We have achieved a high enough energy barrier (eReaxFF: 27 kcal/mol vs DFT: 38 kcal/mol) for C-C=C-C torsion angle rotation which, as desired, retains the planarity of graphene layers in the MD simulations. We have also added DFT data describing the rotation of C-C-C and C-C=C angle

of different hydrocarbon compounds and trained the C-C-C angle parameters. The DFT data for angle bending and rotation of dihedrals were obtained from reference [133]. eReaxFF agrees quite well with the DFT data it was trained against.

The C^{+}-e^{-} interaction has been trained in such a way that e^{-}, instead of sitting directly on the core of C, now orbits the host atom with a 0.35 Å radius. This, somewhat resembles a realistic C behavior where a real C has an atomic radius, i.e., the distance from the center of the nucleus to the outermost shell of an electron, of 0.67 Å. This makes it easy for a neutral graphene system for its electrons to move around in the plane which is in contrast to the behavior from previous iterations of the eReaxFF force fields where only the anionic state of graphene would show electron motion in the graphene plane. Thus, the metallic characteristics of graphene can now be observed in MD simulations.

Results and discussion

Graphene electron conduction in-plane and out-of-plane

For the purpose of testing graphene's in-plane electron conductivity, we have taken single layers of graphene for both charge-neutral system and anion system and performed MD NVT simulations at 300 K. For the neutral system, it is observed that electrons orbit their host atoms' nuclei with a 0.35 Å radius and move from one host to another. Electron exchange between host atoms is seen. A "free electron" motion is observed which resembles a metallic behavior as expected. For the anion system, where there is one extra electron for every 112 carbon atoms, the extra electron moves from one carbon to another while replacing an existing electron's place. The replaced electron will also do the same while moving to the next carbon atom. At a given moment in time, one carbon among the 112 will always have an extra electron. Figure **5-3** (a) shows the extra electron (in transparent red) in a graphene anion at a given moment in time. Figure **5-3** (b)

shows the plot of the total path traveled by the extra electron in 50 ps. From the figure, it is obvious that the extra electron is very mobile and moves to almost all the carbon atoms in the system every now and then.

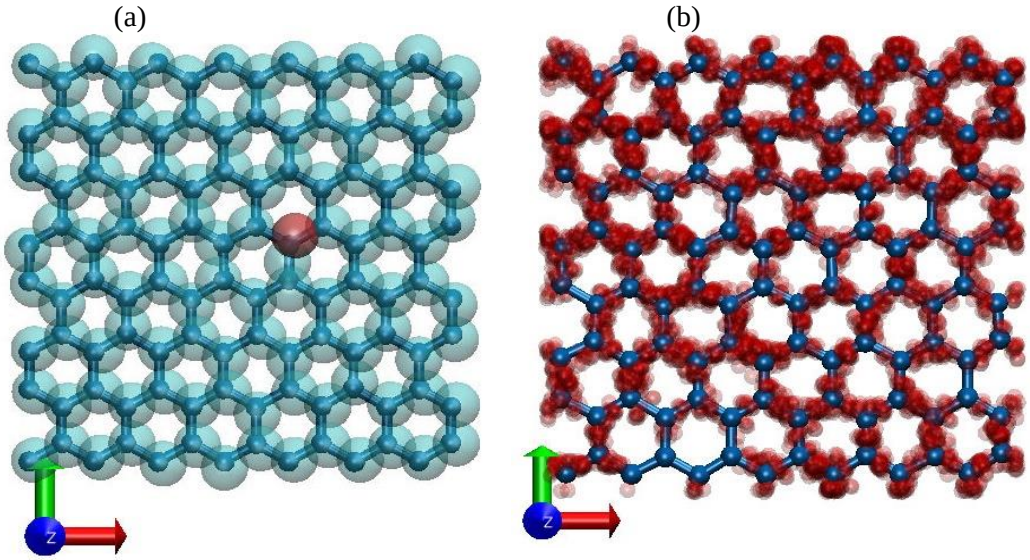

Figure **5-3**: (a) Graphene anion with every C^+ with an electron orbiting them while one of the C^+ has an extra electron shown at a given moment in time. (b) Plot of the total path traveled by the extra electron in graphene anion in 50 ps. Color scheme: C^+: blue, electron: transparent cyan, extra electron: transparent red.

In order to test the quality of the force field in restricting out-of-plane electron motion in graphite, we have taken a graphite consisting 4 graphene layers, each layer consisting 32 carbon atoms, in a periodic box where the second from the top layer contains an extra electron as shown in Figure **5-4** (a). We performed MD NVT simulations at three different temperatures to observe whether temperature has an effect on the out-of-plane motion of electrons. For the room temperature (300 K) simulation, the extra electron only moves in the graphene plane and remains in that plane throughout the period of the whole 205 ps simulations as shown in Figure **5-4** (b). In

other words, graphite perfectly performs as an electrical conductor in the graphene plane and an insulator out-of-plane at room temperature.

Effect of temperature

In order to observe whether temperature has an effect on the out-of-plane electron conduction, we have performed MD simulations at temperatures of 400 K and 500 K. At 400 K and beyond, electrons achieve the energy to cross the barrier for out-of-plane electron motion. Throughout the course of the MD NVT simulation at 400 K, the extra electron spends most of its time in the second from the top layer and then sparks to the third layer just once and remains in that layer as seen from Figure **5-4** (c). In the case of 116 ps simulation at 500 K, the extra electron after spending some time in the second to the top layer sparks to the third layer and after spending most of its time there sparks back to the second layer and then sparks to the top layer and spends a brief time there as seen from Figure **5-4** (d).

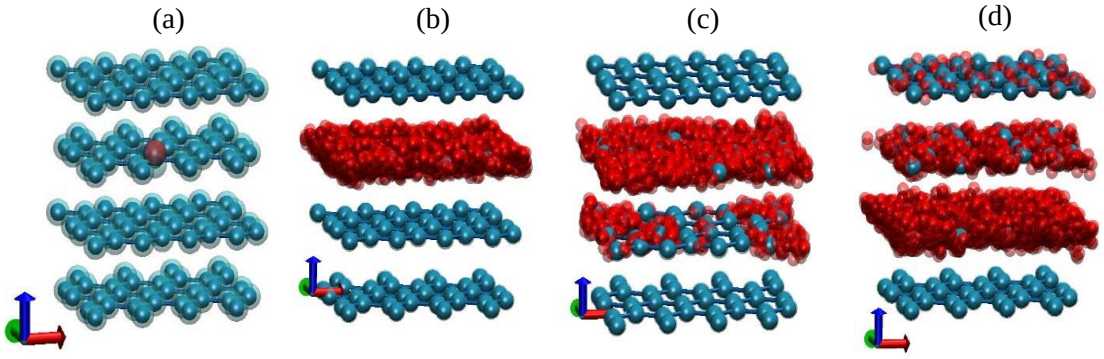

Figure **5-4**: (a) Graphite anion at t = 0, (b) Plot of the total path traveled by the extra electron in graphite anion at 300 K, (b) Plot of the total path traveled by the extra electron in graphite anion at 400 K, (b) Plot of the total path traveled by the extra electron in graphite anion at 500 K. Color scheme: C^{+}: blue, electron: transparent cyan, extra electron: transparent red.

Effect of voltage

In order to observe whether applied voltage has an effect on the out-of-plane electron conduction, we have varied the voltage, in other words varied the excess charge loading of one the graphene layers of graphite. We have performed MD simulations of graphite with the second from the top layer loaded with 2, 3, 4 and 5 extra electrons and recorded the number of times out-of-plane electron motion occurs in 200 ps. Table **5-1** summarizes the effect of applied voltage on the number of electron sparks. We can see that as the number of extra electrons increase in the second from the top layer, the number of out-of-plane electron motion events increase. For the case where 4 extra electrons start in the second layer, the end of the 200 ps simulation reveals that the extra electrons are distributed in such a way that each layer has an extra electron. For the case of 5 extra electrons, the distribution at the end of the simulation is 1 electron in the top layer, 2 in the second and 1 in the third layer and 1 in the bottom layer. The extra electrons essentially redistribute in way such that each graphene layer would reach an equivalent charge.

Table **5-1**: Effect of excess charge loading on out-of-plane electron conductivity.

Number of extra electrons on the second from the layer of graphite	**Number of out-of-plane electron motion events**
2	2
3	3
4	3
5	4

For all the simulations at different temperature and voltage, one thing that is true for all of the cases is that the electron is far more conductive in the plane of graphene compared to the out-of-plane behavior. Electrons are significantly less diffusive perpendicular to the graphene plane than graphene in-plane, thus it can be concluded that our eReaxFF description perfectly captures the true nature of electron conduction in graphitic materials.

Electron conduction in graphene with defects

In a real graphitic anode, point defects such as C-vacancies, Stone-Wales defect, line defects etc. exist. In a bilayer graphene, in addition to point and line defects, an sp^3 connection between the two graphene layers might exist. Such defects in graphene strongly influence the electronic, optical, thermal and mechanical properties [154]. Wrinkles and curvature might also be present in graphene. High-curvature regions of rippled graphene have a higher charge density than planar regions [170]. In this section, we will discuss the electron conduction in an sp^3 connected bilayer graphene and in graphene with single C-vacancy.

Bilayer graphene electron conduction through sp^3 linker

From the previous discussions we have seen that graphite behaves as an insulator in the direction perpendicular to the graphene plane. In this section, we will observe whether extra electrons can easily transmit from one graphene layer to another if these graphene layers are connected by an sp^3 linker. For this purpose, the geometry is created by connecting one carbon atom of one graphene layer with the closest carbon atom of another graphene layer. Since a bond is formed between these two carbon atoms, they become sp^3 hybridized. The sp^3 carbon – sp^3 carbon bond length is 1.7 Å while the distance between the graphene layers is 3.3 Å. Several simulation scenarios at 300 K are performed with different excess charge loading on one side of the sp3 linker in order to observe electron motion through the sp^3 linker and the effect of excess charge loading on electron motion through the vacuum.

Figure **5-5** (a) shows the first case where the bottom layer is loaded with two extra electrons. In the 300 K MD simulation, the two extra electrons diffuse in the graphene plane for a while before one electron comes closer to the sp^3 carbon and then eventually moves through the sp^3 linker to the other graphene layer as shown by the steps in Figure **5-5** (b). During the course of

the MD simulation, the extra electrons do go back and forth from one graphene layer to the other through the sp^3 linker. No electron, however, is seen to spark through the vacuum to transit to the other graphene layer. Figure **5-6** (a) shows the plot of the total path traveled by the extra electrons in the first and last 50 ps of the 230 ps simulation. It can be seen that the extra electrons spend most of their time in the bottom layer and moves back and forth through the sp^3 linker to spend some time in the top layer. From the charge density plot of the last 50 ps of the simulation, it can be seen that the system reached equilibrium with excess charge equally distributed between the two graphene layers (Figure **5-6** (b)). On average, there is one extra electron in each graphene layer.

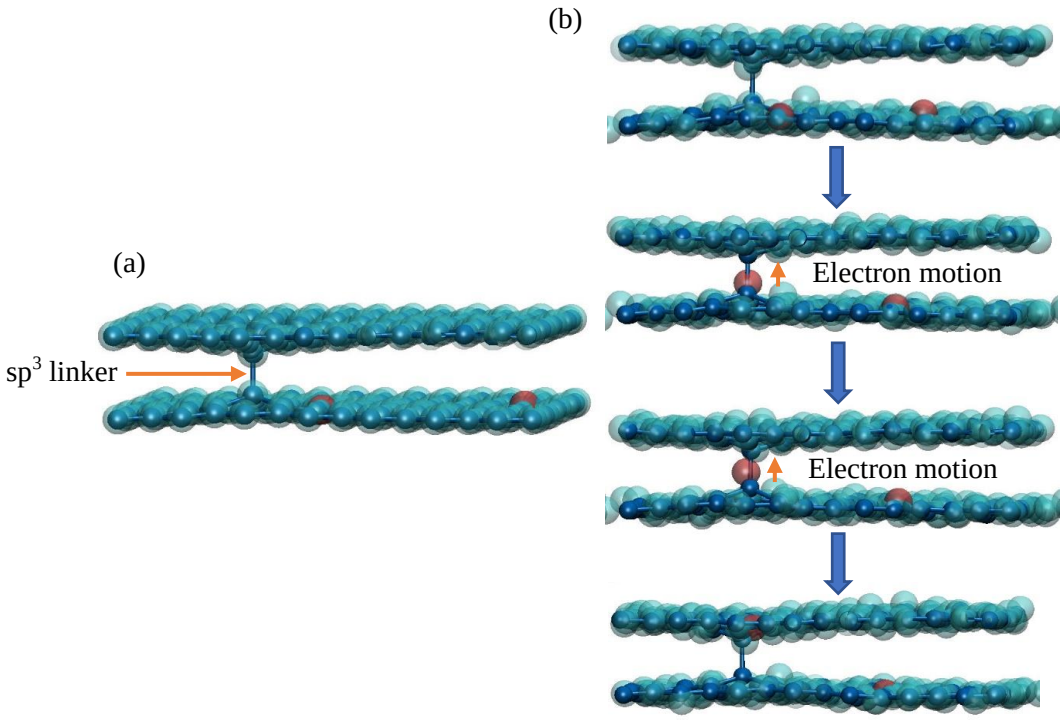

Figure **5-5**: (a) Two graphene layers connected via sp^3 linker with two extra electrons on the bottom layer, (b) Steps involved in the electron transition from one graphene layer to the other through the sp^3 linker. Color scheme: C^+: blue, electron: transparent cyan, extra electron: transparent red.

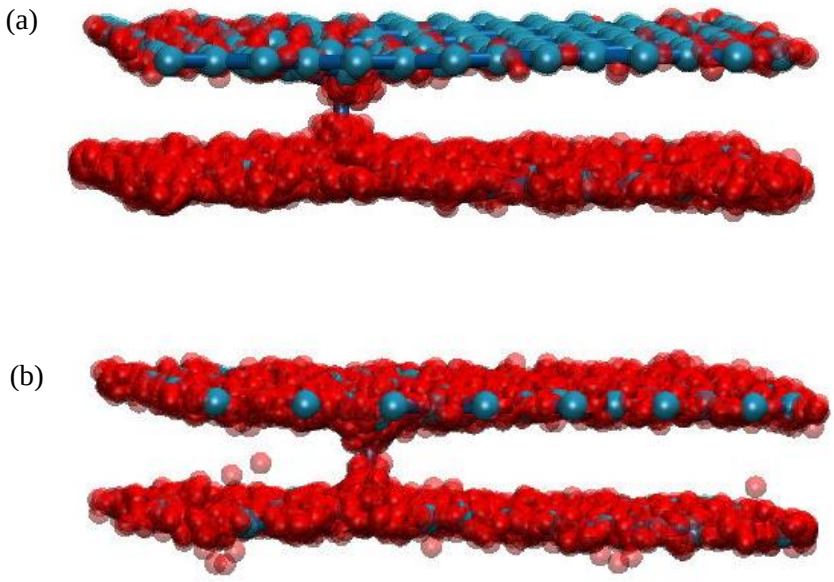

Figure **5-6**: Plot of the total path traveled by the extra electrons for the simulation case starting with two extra electrons in the bottom graphene layer for (a) the first 50 ps, (b) the last 50 ps. Color scheme: C^+: blue, electron: transparent cyan, extra electron: transparent red.

The second simulation case performed included three extra electrons in the bottom graphene layer. Also in this case the extra electrons go back and forth through the sp^3 linker to the other graphene layer and does not show any spark behavior. Charge equilibrium is reached in the first 50 ps and on average, the excess charge is equally divided between the two graphene layers. The charge equilibrium can be observed from the charge density plot shown in Figure **5-7** (a). The final simulation case is with five extra electrons in the bottom layer. Although most of the electron motion is through the sp^3 linker, some electrons spark through the vacuum to the other graphene layer. From Figure **5-7** (b) it can be seen that some electrons' pathway is through the vacuum between the graphene layers since with the high voltage on one graphene layer the spark barrier becomes comparable to the electron transition barrier through the sp^3 linker and thus, a competition between these two pathways is present. The charge equilibrium in this case is also achieved in the

first 50 ps of the simulation. In reality, electrons tunnel and do not occupy the vacuum space at all. Electrons have a quantum nature and tunnelling occurs non-classically. With bias such as high voltage on one graphene layer, electron tunnelling barrier becomes comparable with electron migration barrier through the sp^3 bridge. Although our method treats explicit electrons semi-classically, it still provides useful qualitative information such as the effect high voltage and high temperature has on electron migration.

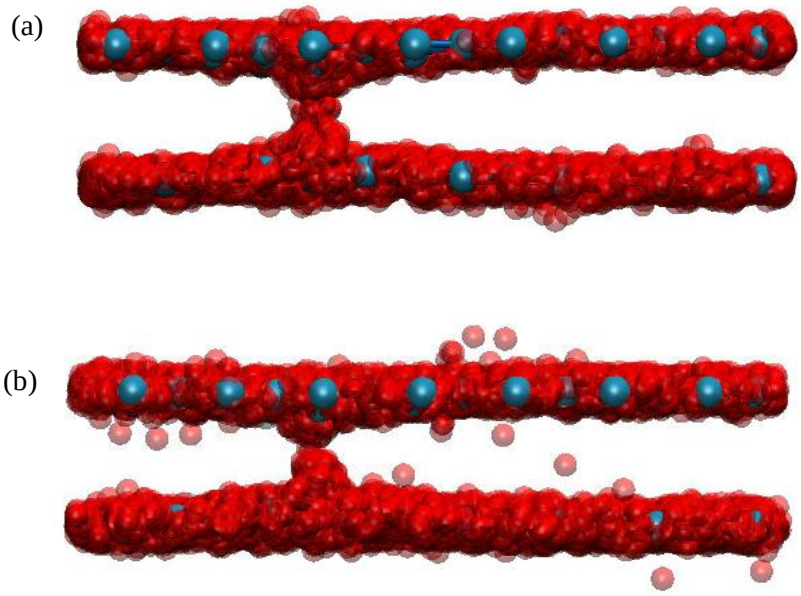

Figure **5-7**: Plot of the total path traveled by the extra electrons in the first 50 ps of the simulation cases starting with (a) three extra electrons in the bottom graphene layer, (b) five extra electrons in the bottom graphene layer. Color scheme: C^+: blue, electron: transparent cyan, extra electron: transparent red.

Electron conduction in graphene with C-vacancy

Carbon vacancies in graphene attract electrons due to the undercoordinated carbon atoms. We have created a graphene with a single carbon vacancy and put an extra electron far from the vacancy to observe whether the extra electron finds the vacancy and gets trapped. During the course of the MD simulation, the electron, indeed, finds its way to the vacancy at gets trapped and spends

most of its time there. Figure **5-8** (a) and (b) show the snapshots of the MD simulation at 300 K where the extra electron is far from the vacancy and trapped at the vacancy respectively. The plot of the total path traveled by the electron as shown in Figure **5-8** (c) proves that the average electron density is highest around the vacancy site.

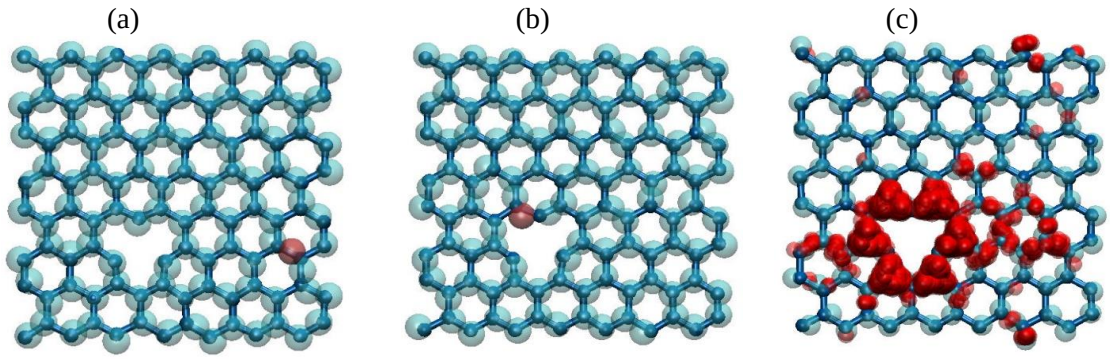

Figure **5-8**: Graphene with single carbon vacancy with (a) extra electron far away from vacancy, (b) extra electron trapped at the vacancy, (c) plot of the total path traveled by the extra electrons in the first 50 ps of the simulation. Color scheme: C^+: blue, electron: transparent cyan, extra electron: transparent red.

Li/Li$^+$ interaction with neutral graphene and graphene anion

In order to observe Li-interaction with graphene at different voltage, we have introduced Li parameters in the graphene eReaxFF force field. The Li neutral atom is represented as represented as a Li^+/e^- pair. The Li parameters are developed to reproduce electron affinity and equation of state for Li-bcc cluster. The electron affinity of Li^+ ion (eReaxFF: 112 kcal/mol vs QC: 128 kcal/mol) is quite close to graphene's electron affinity (eReaxFF: 78 kcal/mol vs QC: 100 kcal/mol) and as such, there is some competition expected between graphene and Li^+ ion to grab extra electrons.

We have performed MD simulations at 300 K with Li^+ ion exposed to both neutral graphene and graphene with one extra electron. Throughout the course of the 800 ps simulation with Li^+ ion

exposed to neutral graphene no electron ever leaves the graphene surface to neutralize the Li^+ ion. On the other hand, the simulation with Li^+ ion exposed to the graphene anion shows that once Li^+ ion is close to the graphene surface (fluctuates between 2.7 to 3.2 Å from graphene surface), almost immediately (t = 3 ps) captures the excess electron of graphene (Figure **5-9**). The captured electron remains with the Li^+ ion, which has now become a Li-neutral and remains so throughout the rest of the 800ps simulation. The Li-neutral now fluctuates between 3.7 to 4.0 Å from the graphene surface. The center of mass of the electron cloud revolves around Li at radius of 1.8 Å. Similar to C, this resembles a realistic Li behavior where a real Li has an atomic radius of 1.67 Å. From Figure **5-9** (b) it can be seen that there is a slight polarization of Li's electron towards the graphene surface.

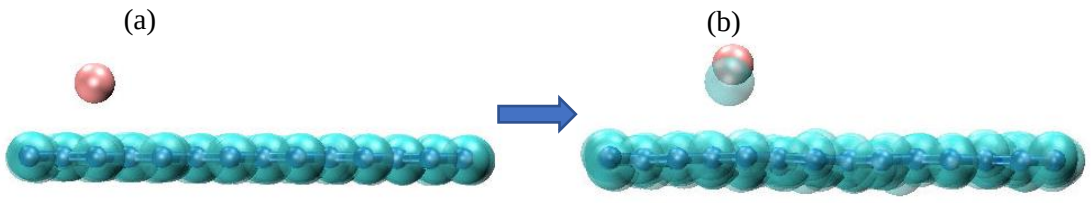

Figure **5-9**: Li^+ ion exposed to graphene anion (a) before and (b) after capturing extra electron from graphene anion. Color scheme: C^+: blue, electron: transparent cyan, Li^+: pink.

Next, MD simulations have been performed on a system with 5 Li^+ ions exposed to graphene anion with 5 extra electrons. All the 5 Li^+ ions find their way towards the graphene surface (Figures **5-10** (a, c)). Throughout the course of the 300 K simulation, 4 out of the 5 extra electrons of graphene are captured by the Li^+ ions. The Li^+ ions, most of which are now Li-neutral approach each other and interact and initiation of Li-metal plating on the graphene surface is observed as shown in Figures **5-10** (b, d). These simulations are somewhat similar to the Li-plating described by [155]. From these aforementioned observations, it can be concluded that the eReaxFF force field has the potential to simulate Li-metal plating on graphene surface.

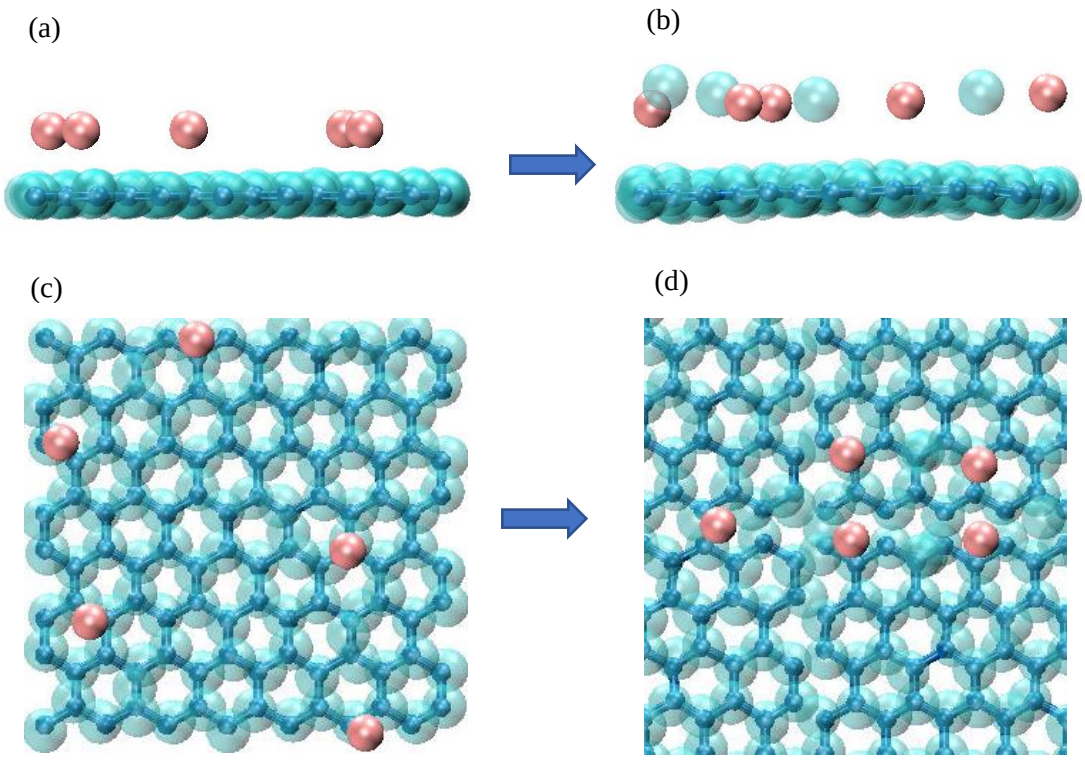

Figure **5-10**: 5 Li^+ ions exposed to graphene anion (a,c) before and (b,d) after capturing 4 extra electrons from graphene anion and forming Li-metal plating on graphene surface. Color scheme: C^+: blue, electron: transparent cyan, Li^+: pink.

Conclusion

We have successfully developed an eReaxFF description for graphene using a Quasi Drude model, where every carbon atom is represented by a C^+/e^- pair. Our force field reproduces the trends of quantum chemistry-based electron affinities and equation of states. The force field is capable of simulating electron conduction in the graphene plane while restricting out-of-plane motion. Out-of-plane conduction can be adjusted based on temperature and applied voltage, however, for all cases the in-plane electron diffusivity far outweighs the out-of-plane diffusivity concluding that graphitic materials are electron conductors in the graphene plane and insulators in the direction perpendicular to the plane. The force field captures the correct trends on electron motion in both

pristine and imperfect graphene. Finally, the developed eReaxFF description shows the correct behavior of Li^+ ions capturing electrons leaked from graphene and shows the potential to simulate Li-metal-plating on the graphene surface. These capabilities are encouraging and, with further development, should enable us to model detailed Li-graphene interaction at non-zero voltages.

Chapter 6

Development of an eReaxFF Force Field for BZY20 Solid Oxide Electrocatalysis

This chapter is part of a manuscript under preparation, authored by Md Jamil Hossain, Yun K. Shin, Jessica Schulze, Gorakh Pawar, Meng Li, Yuxiao Lin and Adri C. T. van Duin. ML and YL calculated the DFT data, JS calculated the constrained-DFT data, MJH constructed the eReaxFF training set, ACTvD optimized the eReaxFF parameters, MJH and YKS performed the simulations, under the supervision of GP and ACTvD. MJH's contribution is presented in this chapter.

Introduction

Electrocatalysis is a type of catalysis that results in the change of the rate of an electrochemical reaction occurring on an electrode surface by varying the electrical potential. Electrocatalysis involves a catalytic process where bonds break and form for oxidation and reduction reactions through the direct transfer of electrons and ions. The electrocatalysts must process the ability to lower the overpotential of these reactions [171] as well as to adsorb key intermediate species as it provides alternate energy pathways [172]. Electrocatalytic processes take place in fuel cells, electrolysis devices or even in electrochemical energy storage in batteries, such as metal–air batteries [173].

One of the key areas in electrocatalysis is clean energy conversion – an electrochemical conversion processes that convert molecules in the atmosphere (e.g., water, carbon dioxide, and nitrogen) into important fuels and chemicals (e.g., hydrogen, hydrocarbons, oxygenates and ammonia). These fuels can be used in fuel cells to produce clean electricity. This current study will focus on hydrogen production. The water-splitting reaction, which consists of the hydrogen

evolution reaction (HER; $2H^+ + 2e^- \rightarrow H_2$), is quite noteworthy in the production of hydrogen [174], [175]. Details of its applications and catalysts utilized are reported in the review article [176].

The reaction rate of an electrocatalyst system can be improved by increasing the number of active sites on a given electrode e.g., through increased loading or improved catalyst structuring to expose more active sites to facilitate binding different reaction intermediates and transition states in different ways. This can be done by alloying, doping, or the introduction of defects.

Transition metal oxides (TMOs) have been widely used in electrocatalysis because of their cost-effective, stable, accessible, and environmentally benign characteristics. Currently, TMOs are one of the most promising classes of electrocatalysts for HER. Yttria doped barium zirconate is a promising solid oxide material for electrocatalysis applications. Barium zirconate doped with 20 mol% of yttrium (BZY20) is an almost pure proton conductor in the presence of water vapor or/and hydrogen containing atmospheres below 650 °C. BZY20 has a high proton conductivity with a small activation energy [177].

Modeling techniques can help understand the complexities of catalyst and electrode/electrolyte interface in the atomistic- and molecular-level while providing insights in the depictions of the solvent, cations, and anions near the interface, as well as the mechanisms and reaction barriers of key steps involving proton/ electron transfers in any reaction environment – lenient to harsh. Modeling the Electrocatalytic processes require to describe bond-breaking and bond-making processes which make a quantum chemical treatment such as density functional theory (DFT) useful and various application of DFT are detailed in the review article [54]. However, the inability of DFT to simulate large length and timescale make them limited in this application. On the other hand, empirical force field-based methods such as reactive force fields can simulate reactions at larger length and time scales.

The ReaxFF reactive force field method has been employed in many chemical systems including solid oxide fuel cells [178]. However, ReaxFF method has its limitations as far electron

conductivity is concerned. The eReaxFF method [65] is an extension of the ReaxFF method with a description of an explicit pseudo-classical electron-like particle. This method has been applied to simulate electronic motion in carbon-based-systems [65], lithium-electrolyte systems [66] and was recently extended to Ag metal systems [156] and polyethylene electrical breakdown [157].

In this manuscript, we describe the development and application of the eReaxFF force field for BZY20 solid oxide. First, we generated a suite of relevant condensed phased density functional theory (DFT) data describing BZY20 bulk and slab structures with and without the presence of oxygen vacancies and water adsorption energies, water splitting and hydrogen generation energies at different surfaces (100, 110) with different surface terminations. Next, these DFT data were subsequently added to existing ReaxFF training data for YSZ solid oxide [178]. Then, we trained the eReaxFF Ba/Zr/Y/O atom, bond, angle and dihedral parameters with the aim to find the optimal reproduction of the DFT data. Finally, we demonstrate the quality of the newly developed force field in simulating the water adsorption, water splitting and eventual proton transfer and hydrogen generation at zero-voltage of the BZY20 solid oxide. Our quality of the force field trends opens up an avenue for introducing the explicit electron component to the force field for the purpose of simulating non-zero voltage scenarios.

Methods

Density functional theory (DFT)

We performed a series of periodic DFT calculations on the bulk and several slab models with different surface terminations of BZY20 solid oxide material. For our periodic DFT calculations we used a combination of VASP and CP2K planewave method using PBE functionals. We have considered different configurations for each case based on the pristine structures as well as structures with oxygen vacancies at different locations and concentrations. Next, we calculated slab models with different concentrations of hydrogenation. Based on these DFT calculations, we

obtained oxygen migration energies, water adsorption energies, hydrogen generation energies and subsequently put all these data in an eReaxFF force field training set. We have also added the training set data of the previously published YSZ solid oxide force field [178] to our training set.

eReaxFF

eReaxFF method is an extension of the standard ReaxFF method which incorporates a pseudo-classical explicit electron scheme. The general expression of the eReaxFF energy is

$$E_{system} = E_{bond} + E_{over} + E_{under} + E_{lp} + E_{val} + E_{tor} + E_{vdWaals} + E_{coulomb} + E_{nucl-elec} + E_{elec}$$

where partial energy contributions include bond, over-coordination penalty and under-coordination stability, lone pair, valence, torsion, non-bonded van der Waals, Coulomb, electron-nucleus interactions and electron-electron interactions respectively. All the many-body bonded interaction and nonbonded interaction terms of ReaxFF are retained with modifications made to the over-coordination penalty, under-coordination stability and lone pair terms to incorporate explicit electrons. In addition, new energy functionals are included to account for electron-nucleus and electron-electron interactions.

In ReaxFF, the bonded and non-bonded interactions are calculated independently, that is, the valency and number of lone pair electrons of an atom type are independent of atomic charge. Thus, the bond orders are fully de-coupled from the charges - as such, a hydrogen ion (H^+) is considered capable of forming bonds. eReaxFF, on the other hand, fixes this shortcoming by introducing variable valency and number of lone-pair electrons of an atom depending on the proximity of explicit electrons. The bond orders and over-coordination, under-coordination and lone pair energies are calculated based on the corrected valence electrons. Removing an electron from an atom decreases the atom's valency and consequently increases the over-coordination of an existing bond, resulting in a larger over-coordination energy penalty, and therefore reduces the

bond order associated with that atom and weakens the bond. In contrast to ReaxFF, this scheme has enabled the eReaxFF method to counteract the formation of unphysical bonds such as H^+–H^+ due to the higher over-coordination penalty stemming from the loss of valence electron from the H atom. To compute atomic charges, eReaxFF uses the atom-condensed Kohn–Sham density functional theory approximated to the second order (ACKS2) charge calculation scheme instead of the electronegativity equalization method (EEM) or the charge equilibrium method (QEq) used by most ReaxFF force fields. In the current eReaxFF force fields, the mass of the electron particles is considered 1 amu in order to allow femto-second MD timesteps.

Force field training

The eReaxFF force field parameters were developed and trained with an aim to reproduce quantum chemistry-based density functional theory (DFT) data. Parameter optimization was conducted using a successive one-parameter search technique [74] to minimize the following expression for the error:

$$error = \sum_{i=1}^{n} \left(\frac{x_{i,lit} - x_{i,eReaxFF}}{\sigma_i} \right)^2 \tag{6.1}$$

where $x_{i,lit}$ and $x_{i,eReaxFF}$ are the target quantum chemistry/experimental data and eReaxFF values of the i^{th} entry of the force field training set and σ_i is the inverse weight that determines how accurately that particular data needs to be fitted with the QC. The summation of all errors in the training set provides the overall error, which is one of the measures of the quality of the force field.

We have taken BZY20 bulk structure with three different Y doping locations. From Figure **6-1**, it can be seen that the Y doping of the 3rd kind is the most energetically favorable one according

to both eReaxFF and DFT. The rest of the analysis will be based on the structure corresponding to the 3rd kind of doping.

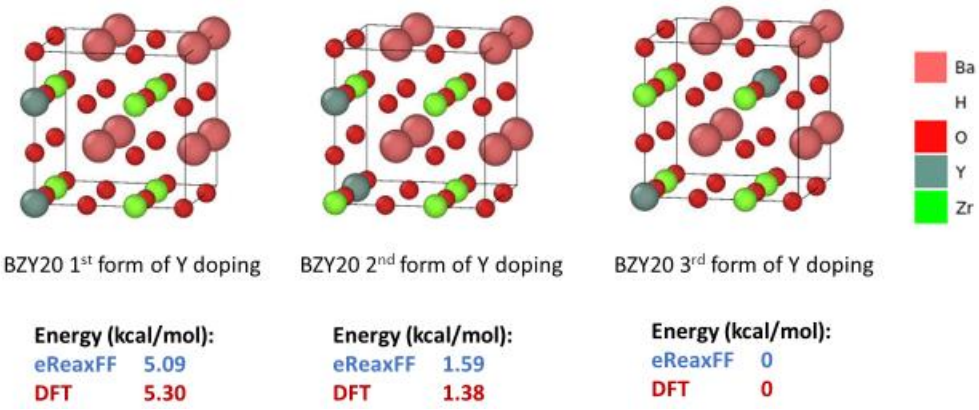

Figure **6-1**: BZY20 bulk structures with different Y doping position and comparison of their energies calculated by both eReaxFF and DFT.

Now, oxygen vacancies are created by removing one or two oxygen atoms at different locations and shown in Figure **6-2** (a). The 't1 O vac' and 't2 O vac' structures have one oxygen vacancy while '2 t1 O vac' and '2 t2 O vac' structures have two oxygen vacancies. The corresponding eReaxFF and DFT energies are plotted in the bar graph in Figure **6-2** (b). The negative number indicates that the existence of oxygen vacancies in the structures are not energetically favorable. Similar qualitative trends between eReaxFF and DFT energies can be seen.

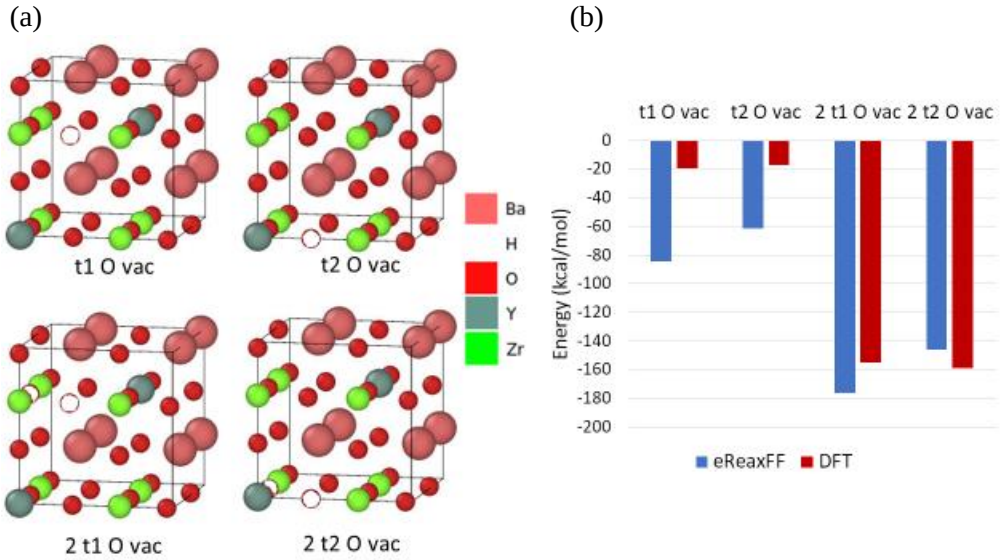

Figure **6-2**: (a) BZY20 3rd form of Y doping with different number and sites of oxygen vacancies (marked in white circles) and (b) comparison of their energies calculated by both eReaxFF and DFT.

Figure **6-3** shows the equation of state of BZY20 bulk structure calculated using both eReaxFF and DFT. Both methods are in excellent agreement with each other, especially around the equilibrium volume.

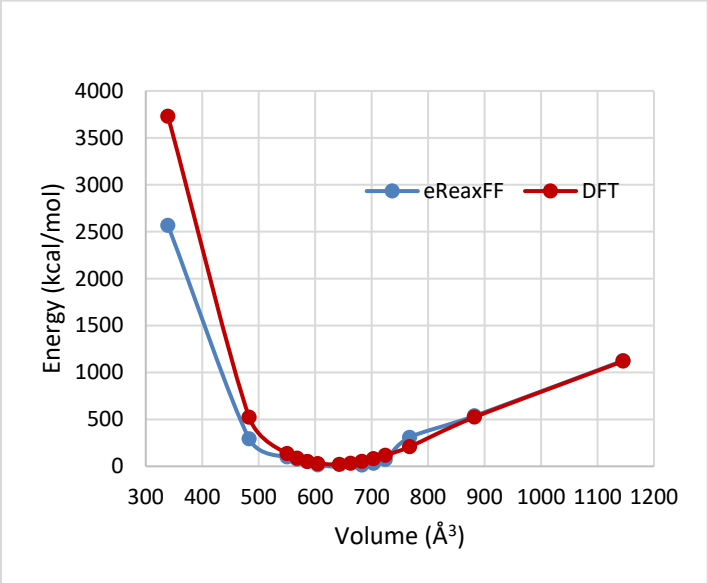

Figure **6-3**: (a) eReaxFF and DFT comparison of equation of state for BZY20 3rd form of Y doping.

In order to study the different aspects of the surface chemistry of BZY20 solid oxide, we built slab models from the BZY20 bulk structure with the 3rd form of Y doping (Figure **6-4**). We considered two different surface orientations – the (100) and (110). We considered two different terminations for the (100) surface – Ba-O termination and Zr-Y-O termination. From the slab models, we created surface oxygen vacancies at different sites with different concentrations (Figures **6-5** and **6-6**). The corresponding eReaxFF and DFT energies for oxygen vacancy formation are summarized in Table **6-1**. Similar to the case of bulk structures, the vacancy formation energies for surfaces are also negative, meaning that the presence of vacancy is not energetically favorable.

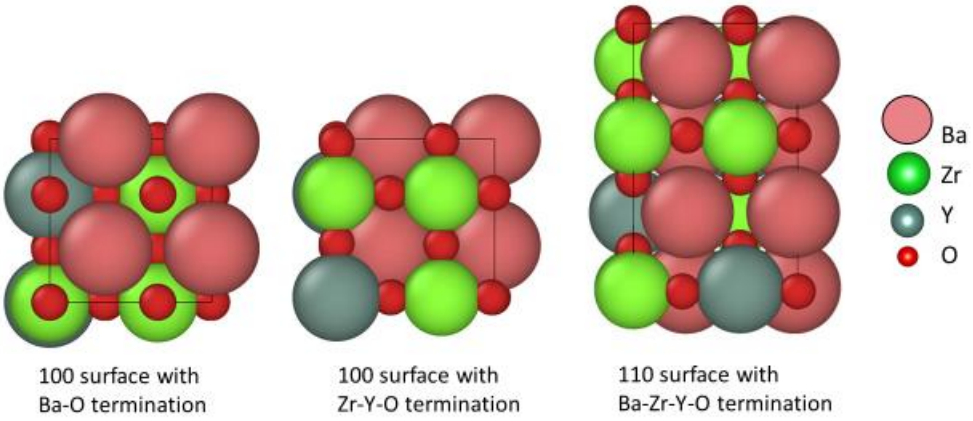

Figure **6-4**: (a) Top view of BZY20 slab models with different surface orientations and surface terminations

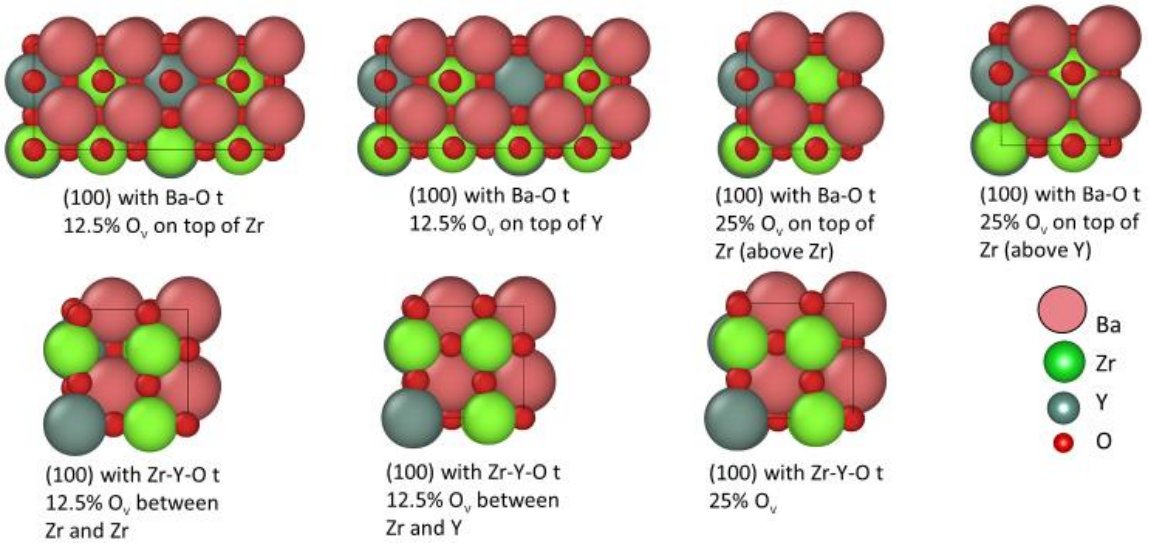

Figure **6-5**: Top view of BZY20 (100) surfaces with different terminations and surface oxygen vacancy (O_v) concentrations and sites.

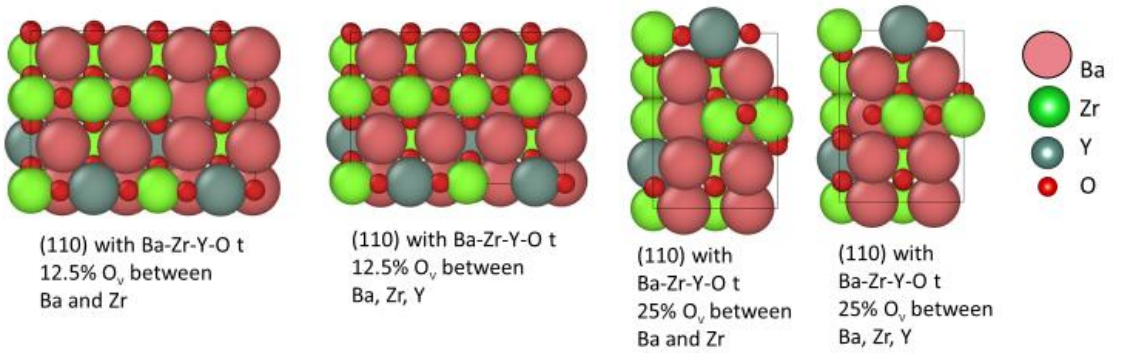

Figure **6-6**: Top view of BZY20 (110) surfaces with Ba-Zr-Y-O termination and different surface oxygen vacancy (O_v) concentrations and sites.

Table **6-1**: eReaxFF and DFT comparison of BZY20 surfaces with different terminations, surface oxygen vacancy (O_v) concentrations and sites.

Orientation	Termination	O_v concentration at surface	O_v site	O_v formation energy (kcal/mol)	
				eReaxFF	DFT
(100)	Ba-O	12.5%	On top of Zr	-141.40	-236.62
(100)	Ba-O	12.5%	On top of Y	-92.17	-99.61
(100)	Ba-O	25%	On top of Zr (above Zr)	-112.40	-82.68
(100)	Ba-O	25%	On top of Zr (above Y)	-103.68	-115.69
(100)	Zr-Y-O	12.5%	Between Zr & Zr	-110.96	-117.74
(100)	Zr-Y-O	12.5%	Between Zr & Y	-86.65	-65.69
(100)	Zr-Y-O	25%	Between Zr & Zr and Zr & Y	-182.42	-244.01
(110)	Ba-Zr-Y-O	12.5%	Between Ba & Zr	-119.49	-98.47
(110)	Ba-Zr-Y-O	12.5%	Between Ba & Zr & Y	-66.34	-60.07
(110)	Ba-Zr-Y-O	25%	Between Ba & Zr	-145.52	-49.46
(110)	Ba-Zr-Y-O	25%	Between Ba & Zr & Y	-100.49	-184.98

Finally, we calculated reaction energies for H_2O gas adsorption and H_2O splitting to H and OH where OH would locate at a surface oxygen vacancy site and H would connect to a lattice oxygen. Figure **6-7** shows the H_2O gas adsorption splitting reaction with energies calculated by eReaxFF and DFT for (100) surface with Zr-Y-O termination with different oxygen vacancy concentrations. Figure **6-8** shows the H_2 gas generation reaction energies calculated by eReaxFF

and DFT for the same surface. The eReaxFF calculated energies agree quite well with the DFT energies indicating that the newly developed eReaxFF force field has been trained well with the DFT data.

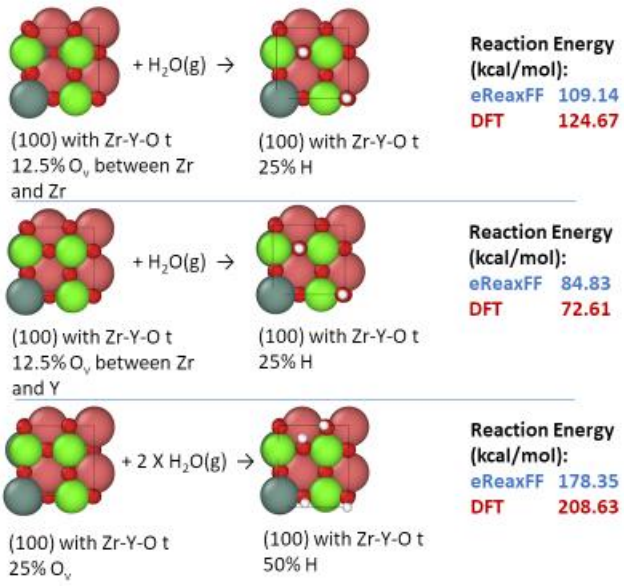

Figure **6-7**: eReaxFF and DFT comparison of H_2O adsorption and splitting reaction energies on BZY20 surfaces.

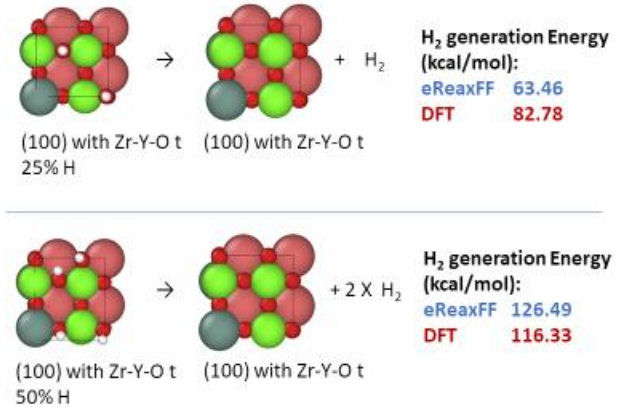

Figure **6-8**: eReaxFF and DFT comparison of H_2 generation energies on BZY20 surfaces.

Based on the above discussion, it can be concluded that our force field is capable of reproducing the DFT data it was trained against quite well. In the next section, molecular dynamics simulations based on this force field will be discussed.

Results and discussion

Utilizing our newly developed eReaxFF force field, we performed simulations on a BZY20 slab model with Zr-Y-O terminated surface with 12.5% surface oxygen vacancies. The oxygen vacancies are located between Zr and Y atoms. The mechanism of water adsorption on the oxygen vacancy site and the eventual formation of hydrogen gas is as following:

$H_2O(g) + O_v + O_O \rightarrow OH + OH$ [O_v is an oxygen vacancy site, O_o is a lattice oxygen site]

$2OH \rightarrow 2O_O + 2H$

$2H \rightarrow H_2(g)$

An H_2O molecule adsorbs at the oxygen vacancy site and splits into an H and an OH. H adsorbs on a lattice O, while OH locates at an O_v site. Next, the two OH splits and the two H atoms bind to form H_2 gas.

Bond restraint simulations

In order to determine the binding energy of water molecule and the energy barriers concerning water splitting reactions and hydrogen generation reactions, we performed bond scans using a biasing potential. Figures **6-9** and **6-10** shows the different stages and energy barriers of the reactions. From figure **6-9**, it can be seen that water, initially far above the surface (stage 1), finds the oxygen vacancy site and adsorbs with an adsorption energy of 65 kcal/mol (stage 2). Now the water can split into H and OH where OH is situated at the Ov site and H can choose lattice oxygen either between an Y and Zr (Path A) (stage 3b), or between two Zr (Path B) (stage 3a). Path A is more favorable since it has lower energy barrier (7 kcal /mol) than Path B's energy barrier (9

kcal/mol). Also, Path A is more exothermic (-16 kcal/mol) than Path B's exothermicity (-11 kcal/mol). The H dissociation from OH and eventual H_2 formation can occur either from stage 2 or state 3b as shown in Figure **6-10**. H_2 generation directly from stage 2 is more favorable than from stage 3b but for both cases the energy barriers are extremely high and endothermic indicating that, these reactions might not occur in the solid oxide operating temperature of 800 K. No excess electrons, thus no applied voltage, are present in the solid oxide. It is expected that at applied voltages, the H_2 generation barrier might get lowered and H_2 generation might occur in the simulations.

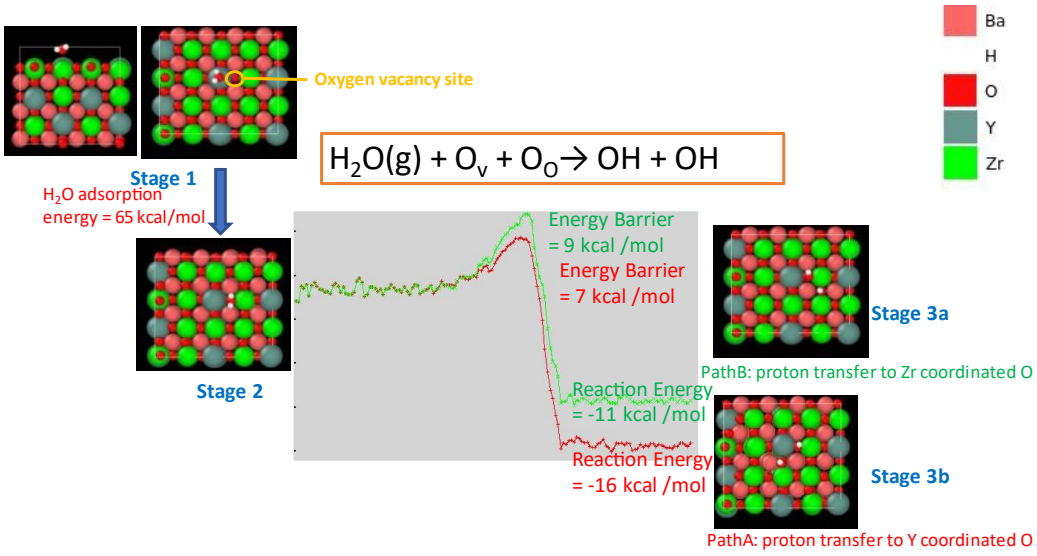

Figure **6-9**: Snapshots of bond restraint simulations and energy barriers and reaction energies associated with water adsorption and water splitting reactions. Color scheme: Ba: pink, H: white, O: red, Y: grey and Zr: green.

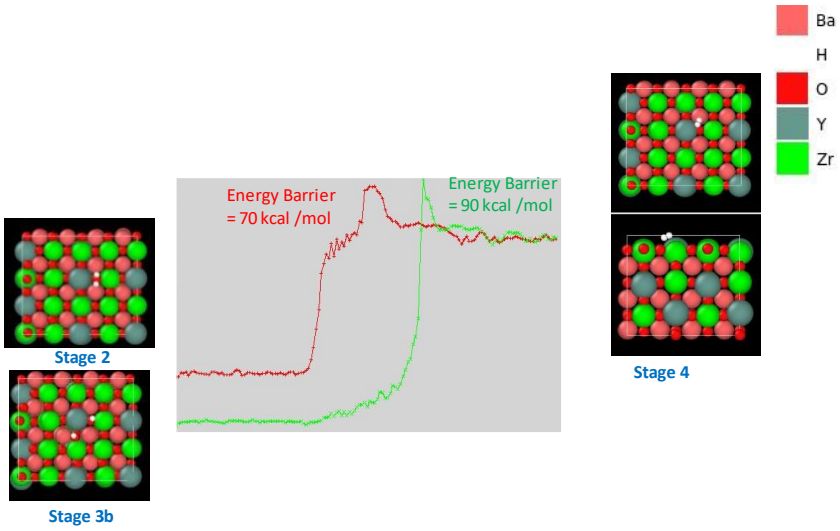

Figure **6-10**: Snapshots of bond restraint simulations and energy barrier associated with hydrogen generation reactions. Color scheme: Ba: pink, H: white, O: red, Y: grey and Zr: green.

Molecular dynamics simulations

In this section we will describe large scale molecular dynamics simulations of steam exposed to BZY20 solid oxide with 12.5% oxygen vacancy between Zr and Y atoms. This gives us 25 vacancy sites on the surface. The density of actual superheated steam at 773 K is 0.00028 g/cm^3, however, in our simulation we are using is a density of 0.0065 g/cm^3 and a temperature of 1000 K in order to enhance the reaction dynamics over the MD simulation time we chose. We have performed MD NVT simulations for 412 ps. Figures **6-11** (a) and (b) show the snapshots at the beginning and end of the simulation, respectively. Throughout the course of the MD simulation, all but one H_2O molecules adsorb at the vacancy sites and the remaining adsorbs at Zr. All adsorbed H_2O molecules split into H and OH and H moves to lattice oxygen sites between Zr and Y, which is a favorable site as we have discussed earlier. Three protons transfer to subsurface oxygens, among them two transfers to the second from the top layer and one transfer to the third layer. This proves the current force field's capability of simulating proton transfer to bulk regions on the solid

oxide. This is a zero-voltage simulation, so as expected, no H_2 generation is observed due to extremely high energy barrier associated with this reaction.

It is expected that, with the implementation of the explicit electron concept in this eReaxFF force field, we would be able to train and simulate no-zero voltage scenarios and expect H_2 generation to occur.

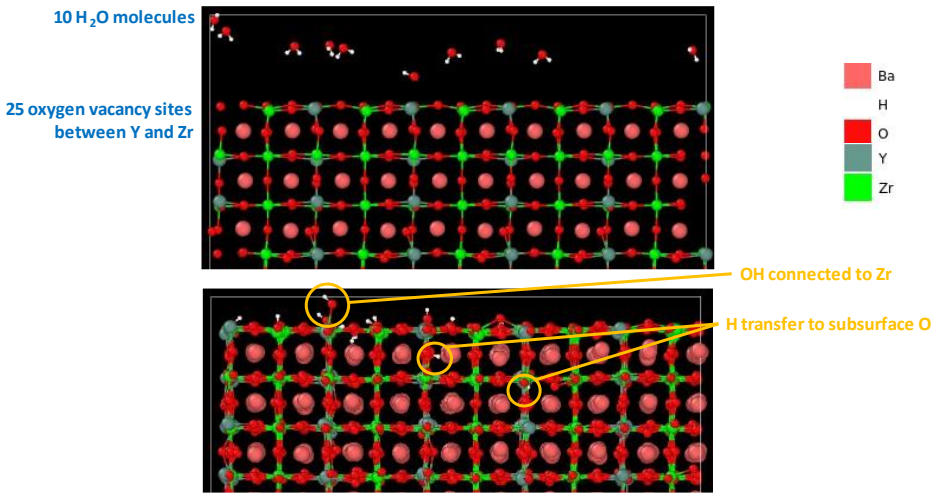

Figure **6-11**: Snapshots of zero-voltage MD simulation of steam adsorption, H_2O splitting, proton transfer reactions at (a) t = 0 and (b) t = 412 ps. Color scheme: Ba: pink, H: white, O: red, Y: grey and Zr: green.

Conclusion

We have successfully developed an initial framework for simulating BZY20 solid oxide electrocatalysis. The newly developed eReaxFF force field reproduces the DFT data it was trained against quite well. The zero voltage simulations of steam adsorption on BZY20 surface with oxygen vacancies conclude that hydrogen generation does not occur at operating temperature of 1000 K. Based on our simulation results, we conclude that this force field sets a stage for the introduction of explicit electron concept by further training the eReaxFF with constrained-DFT data in order to simulate electron conductivity and non-zero voltage effects on hydrogen generation.

Chapter 7

Conclusions and Future Directions

In this dissertation, we studied interfacial physical and chemical phenomena of Li-ion batteries and BZY20 solid oxide electrocatalyst. The following sections summarize the findings and outlook for future directions.

Conclusions

We have developed a ReaxFF force field for Li/ $LiPF_6$/ EC / EMC / VC system to simulate solid electrolyte interphase formation chemistry in the anode/electrolyte interface. We used two separate Li parameter set to distinguish between Li-neutral and Li-cation and their behavior concerning solvation, desolvation, solvent exchange and reactivity with electrolyte molecules that lead to the initiation of the solid electrolyte interphase formation. Our ReaxFF predicted results for the organic electrolyte decomposition reactions and binding energies of Li with electrolyte molecules are in good agreement with the trend of the DFT data it was trained against. Our force field correctly distinguishes between the reactivity of a neutral Li atom and a Li^+ cation. We find that the Li^+ atom type cannot initiate a reduction reaction while a neutral Li atom can. We found that the size of the solvation structure has a significant effect on the reduction decomposition of electrolytes. The reaction barrier increases as the size of the solvation structure increases.

We developed an eReaxFF force field for the description of graphitic anodes using the quasi Drude model which shows the correct trend of quantum chemistry-based electron affinities and equations of state that it was trained against. We trained the force field in way such that it reflects that the in-plane electron diffusivity far outweighs the out-of-plane diffusivity concluding

that graphitic materials are electron conductors in the graphene plane and insulators in the direction perpendicular to the plane. We have also successfully used this force field to simulate both zero and non-zero voltage simulations on pristine and imperfect graphitic materials. Finally, the preliminary results of the simulations on Li^+ ions exposed to graphene and the initiation of Li-metal-plating at applied voltages opens an avenue for future development of Li-graphene interactions and Li-metal plating on graphitic surfaces.

We developed an eReaxFF force field for Yttria doped barium zirconate (BZY20) electrocatalysis. The newly developed eReaxFF force field reproduces the DFT data it was trained against quite reasonably. We utilized the force field to simulate oxygen vacancy migrations, water adsorption, water splitting and hydrogen generation at surfaces at zero applied voltage. This force field sets a stage for the introduction of explicit electron concept by further training the eReaxFF with constrained-DFT data in order to simulate electron conductivity and non-zero voltage effects on hydrogen generation.

Future Directions

The probability of leaked electrons being captured by a Li^+ cation or electrolyte solvent molecule depends on the proximity to the anode and the anode voltage. The newly developed eReaxFF graphene force field can be utilized in obtaining a probability distribution of leaked electrons from a graphitic anode being captured by Li^+ cation. Based on the obtained probability distribution, and using our ReaxFF Li/Li^+-electrolyte force field, some Li^+ cations can be converted to neutral Li in a Monte Carlo type scheme that takes into account proximity to the graphitic anode and the anode voltage and neutral Li eventually can initiate electrolyte reduction decomposition leading to the formation of solid electrolyte interphase.

The eReaxFF graphene force field shows promising results for the initiation of Li-metal plating on the graphene surface. By further re-training the force field we can improve Li properties as well as Li-graphene interactions to correctly capture Li-metal-plating behavior on pristine and imperfect graphene and Li-dendrite formation on graphitic anode materials. High-curvature regions of rippled graphene have a higher charge density than planar ones. We plan to improve our graphene eReaxFF force field to incorporate this behavior by training the force field to compute higher magnitude of electron affinity for curved site than planar site of curved graphene.

We plan to integrate the ReaxFF Li/Li^+-electrolyte force field with a ReaxFF Li-graphite force field to simulate the complete anode half-cell of a Li-ion battery. The ReaxFF Li-graphite has been improved with adding additional DFT data describing Li-graphene interactions at basal planes and edge planes, equation of states for graphite and lithiated graphite. The next step would be to combine the training sets and reparameterize these two force fields to capture the complete anode half-cell.

We plan to add explicit electron description to the BZY20 eReaxFF force field and further train it against constrained-DFT data to study the effects of applied voltage on hydrogen generation. Thereafter, we plan to extend the BZY20 force field to BZCYYb (Yttrium, Cerium and Ytterbium doped barium zirconate) solid oxide to compare the behaviors of oxygen migrations and hydrogen generation and to determine its usefulness in electrocatalysis applications.

Appendix

Supplementary material for additional DFT results, additional ReaxFF force field optimization results and binding energies of solvation structures

The appendix covers the supplementary material for Chapter 4: Lithium-electrolyte solvation and reaction in the electrolyte of a lithium ion battery: A ReaxFF reactive force field study.

Additional DFT results

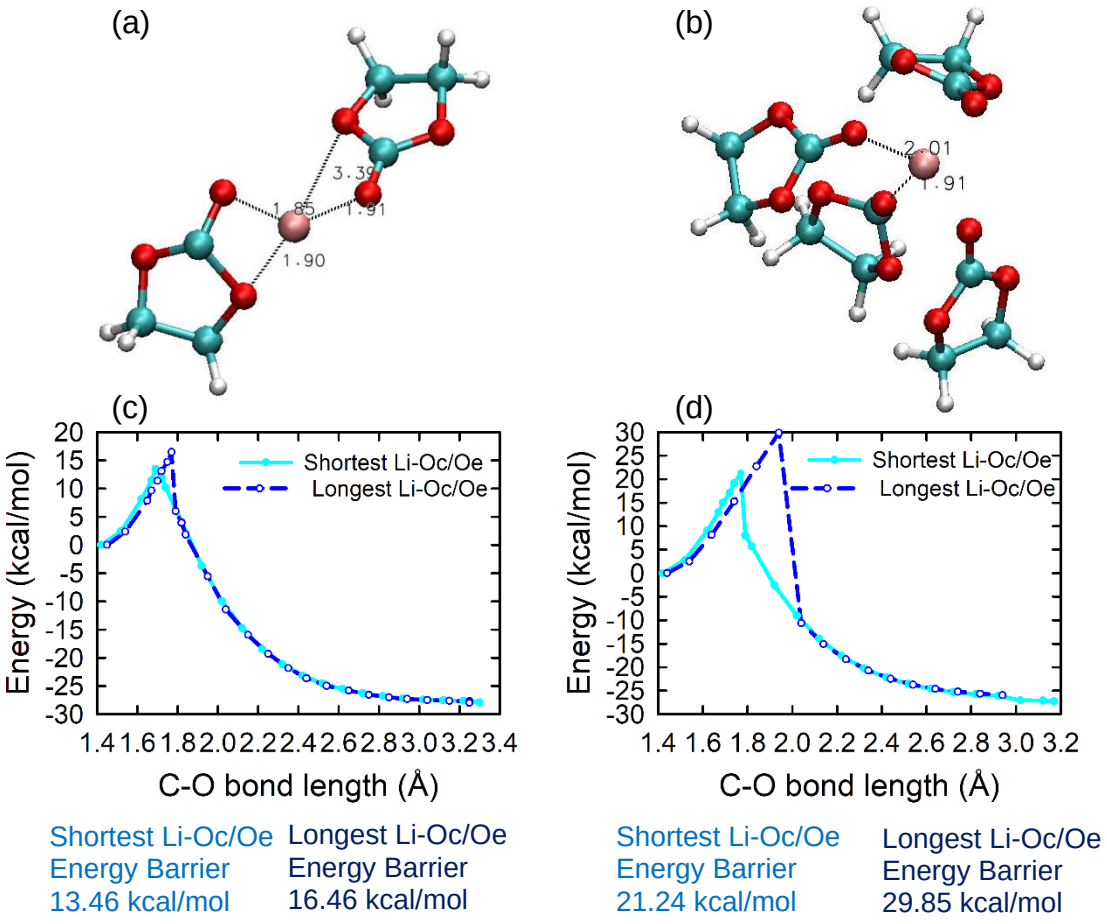

Figure **A-1**: Structures showing shortest and longest Li-Oc (carbonyl O) / Li-Oe (ether O) distance for (a) $Li(EC)_2$ and (b) $Li(EC)_4$, DFT results for ring opening of EC with shortest and longest Li-Oc/Oe distance for (c) $Li(EC)_2$ and (d) $Li(EC)_4$. Atom color scheme: C: cyan, H: white, O: red and Li: pink.

Additional ReaxFF force field optimization results

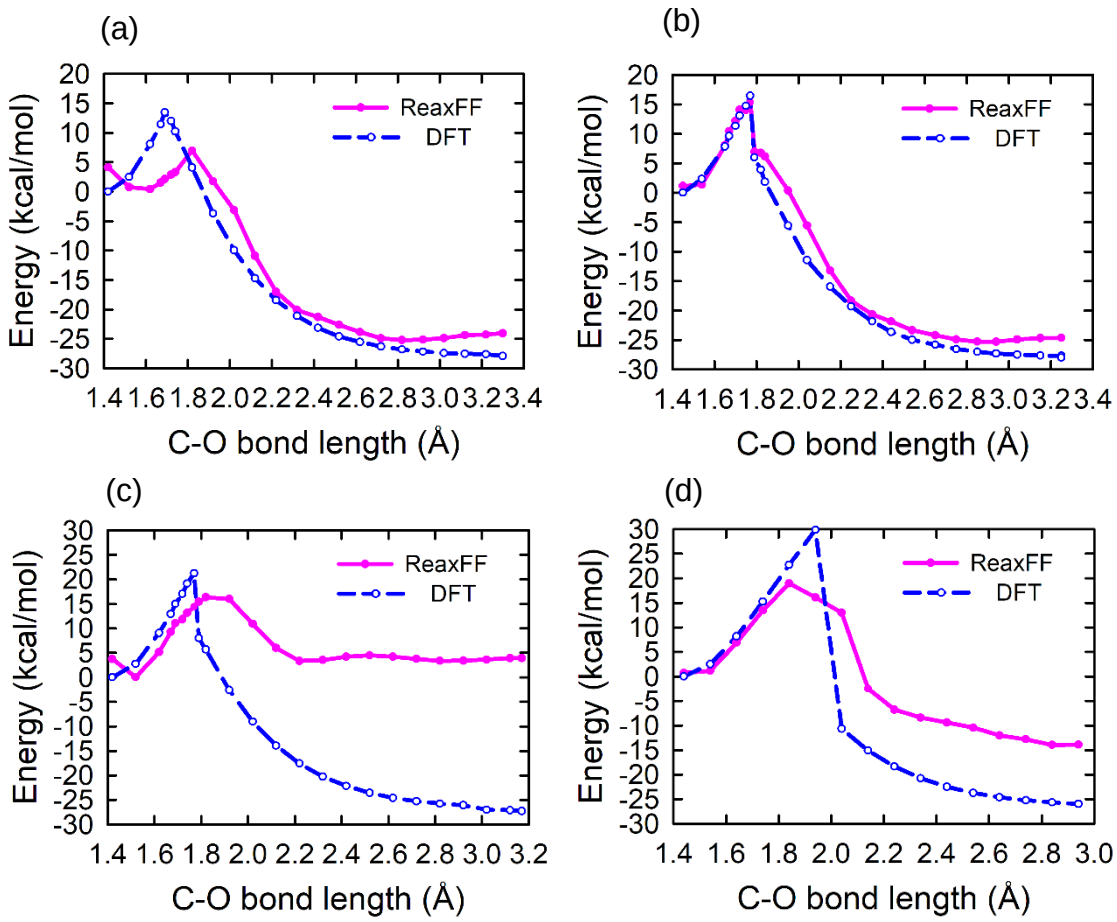

Figure **A-2**: ReaxFF vs DFT results for ring opening of EC with (a) shortest Li-Oc/Oe distance in $Li(EC)_2$, (b) longest Li-Oc/Oe distance in $Li(EC)_2$, (c) shortest Li-Oc/Oe distance in $Li(EC)_4$ and (d) longest Li-Oc/Oe distance in $Li(EC)_4$.

The ReaxFF predicted reaction barriers are somewhat smaller than the DFT barriers since for the single EC case the reaction barrier was intentionally kept smaller. However, ReaxFF produces the trends very well showing that the barrier increases for the increase in solvation structure size as well as Li-Oc/Oe distance. For the short Li-Oc/Oe case of $Li(EC)_4$ (Figure **A-2** (c)), ReaxFF does not produce the exothermicity like the DFT case. This is because the DFT predicts a Li monodentate mode with the Oc of the ring open EC and ReaxFF predicts the monodentate case to be endothermic. ReaxFF requires a Li bidentate mode for exothermicity. The

DFT of the long Li-Oc/Oe case of $Li(EC)_4$ (Figure **A-2** (d)), on the other hand, predicts a Li bidentate mode with Oc and Oe of the ring open EC while pushing away another EC. ReaxFF somewhat gets some exothermicity in this case.

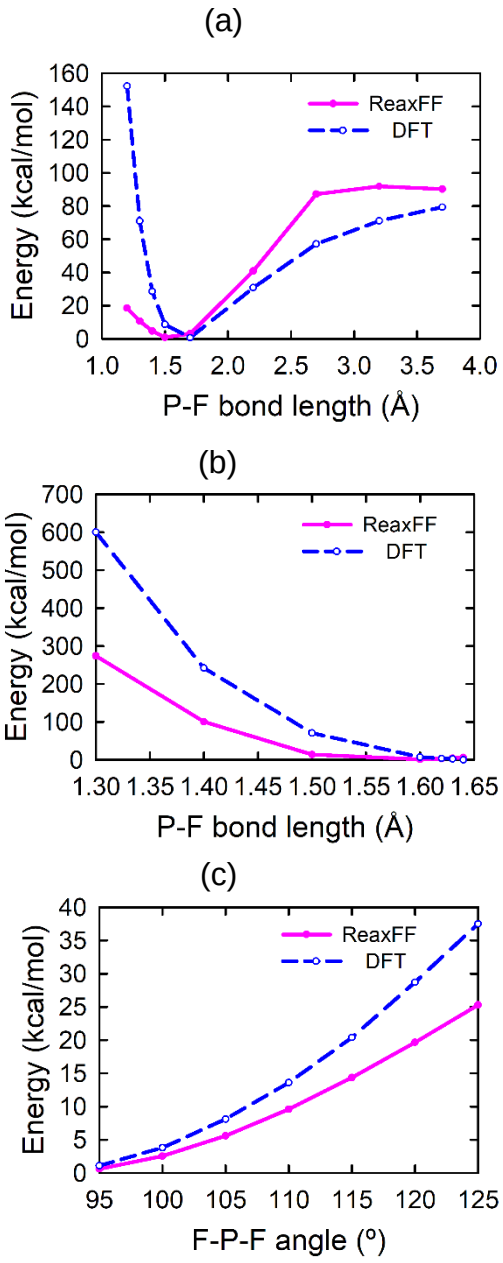

Figure **A-3**: ReaxFF vs DFT results of (a) a single P-F bond compression/stretch in PF_6, (a) all P-F bond compression/stretch in PF_6 and (c) F-P-F angle scan in PF_6.

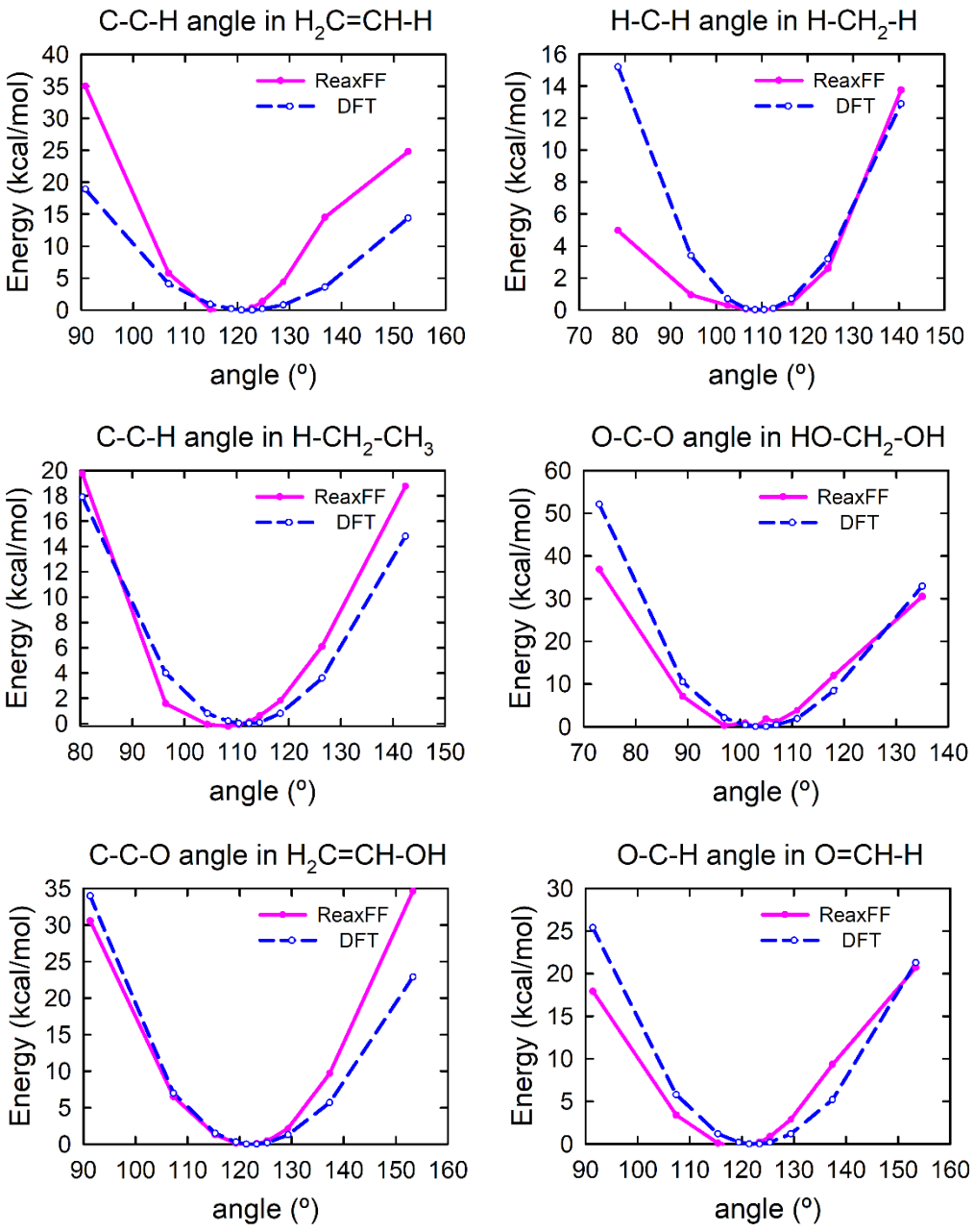

Figure **A-4**: ReaxFF vs DFT results of different angles in various hydrocarbons.

Total binding energies of solvation structures

We have calculated the total binding energies for $Li(EC)_n$ and $Li(EMC)_n$ (n=1~4) using the following expression:

$$\Delta E = E_{Li(EC/EMC)_n} - E_{Li} - nE_{EC/EMC} \quad \text{(A.1)}$$

We have considered both Li neutral and Li^+ ion for the binding energy calculations. The solvation structures with Li^+ was calculated by constraining the whole system of $Li(electrolyte)_n$ as +1.

We have also calculated total binding energies for $PF_6Li(EC)_n$ and $PF_6Li(EMC)_n$ (n=1~3) solvation structures by the following expression:

$$\Delta E = E_{PF_6Li(EC/EMC)_n} - E_{PF_6Li} - nE_{EC/EMC} \quad \text{(A.2)}$$

Table **A-1**: ReaxFF vs DFT results of total binding energies of $Li(EC)_n$ solvation structures.

Solvation structure	Total binding energy (kcal/mol)	
	ReaxFF	DFT
$Li(EC)_1$	-27.29	-14.93
$Li(EC)_2$	-52.87	-33.12
$Li(EC)_3$	-70.36	-49.49
$Li(EC)_4$	-101.13	-57.08

Table **A-2**: ReaxFF, DFT and AEM comparison of total binding energies of $Li^+(EC)_n$ solvation structures.

Solvation structure	Total binding energy (kcal/mol)		
	ReaxFF	DFT	AEM
$Li^+ (EC)_1$	-38.31	-51.56	-52.22
$Li^+ (EC)_2$	-57.23	-90.02	-99.23
$Li^+ (EC)_3$	-64.51	-113.21	-138.46
$Li^+ (EC)_4$	-68.25	-126.77	-167.31

Table **A-3**: ReaxFF vs DFT results of total binding energies of $Li(EMC)_n$ solvation structures.

Solvation structure	Total binding energy (kcal/mol)	
	ReaxFF	DFT
$Li(EMC)_1$	-13.29	-12.80
$Li(EMC)_2$	-35.18	-21.96
$Li(EMC)_3$	-38.04	-30.12

Table **A-4**: ReaxFF, DFT and AEM comparison of total binding energies of $Li^+(EMC)_n$ solvation structures.

Solvation structure	Total binding energy (kcal/mol)		
	ReaxFF	DFT	AEM
$Li^+(EMC)_1$	-37.25	-46.69	-48.81
$Li^+(EMC)_2$	-54.34	-81.84	-96.19
$Li^+(EMC)_3$	-58.71	-101.98	-130.37

Table **A-5**: ReaxFF vs DFT results of total binding energies of $PF_6Li(EC)_n$ solvation structures.

Solvation structure	Total binding energy (kcal/mol)	
	ReaxFF	DFT
$PF_6Li(EC)_1$	-26.60	-23.20
$PF_6Li(EC)_2$	-53.33	-42.46
$PF_6Li(EC)_3$	-78.23	-54.51

Table **A-6**: ReaxFF vs DFT results of total binding energies of $PF_6Li(EMC)_n$ solvation structures.

Solvation structure	Total binding energy (kcal/mol)	
	ReaxFF	DFT
$PF_6Li(EMC)_1$	-30.61	-24.16
$PF_6Li(EMC)_2$	-56.30	-40.48

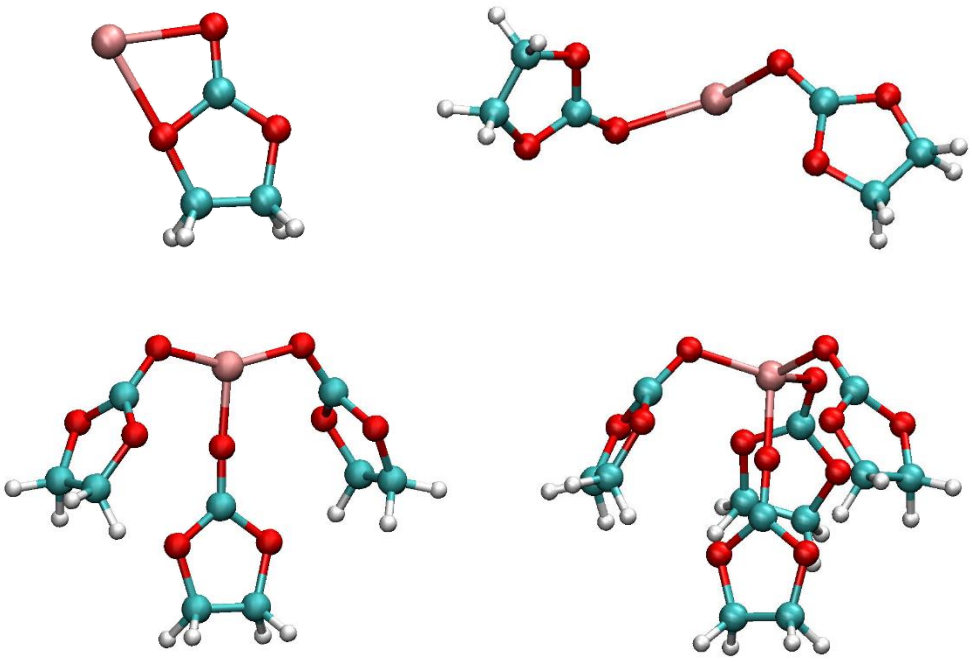

Figure **A-5**: $Li(EC)_n$ (n = 1 ~ 4) solvation structures.

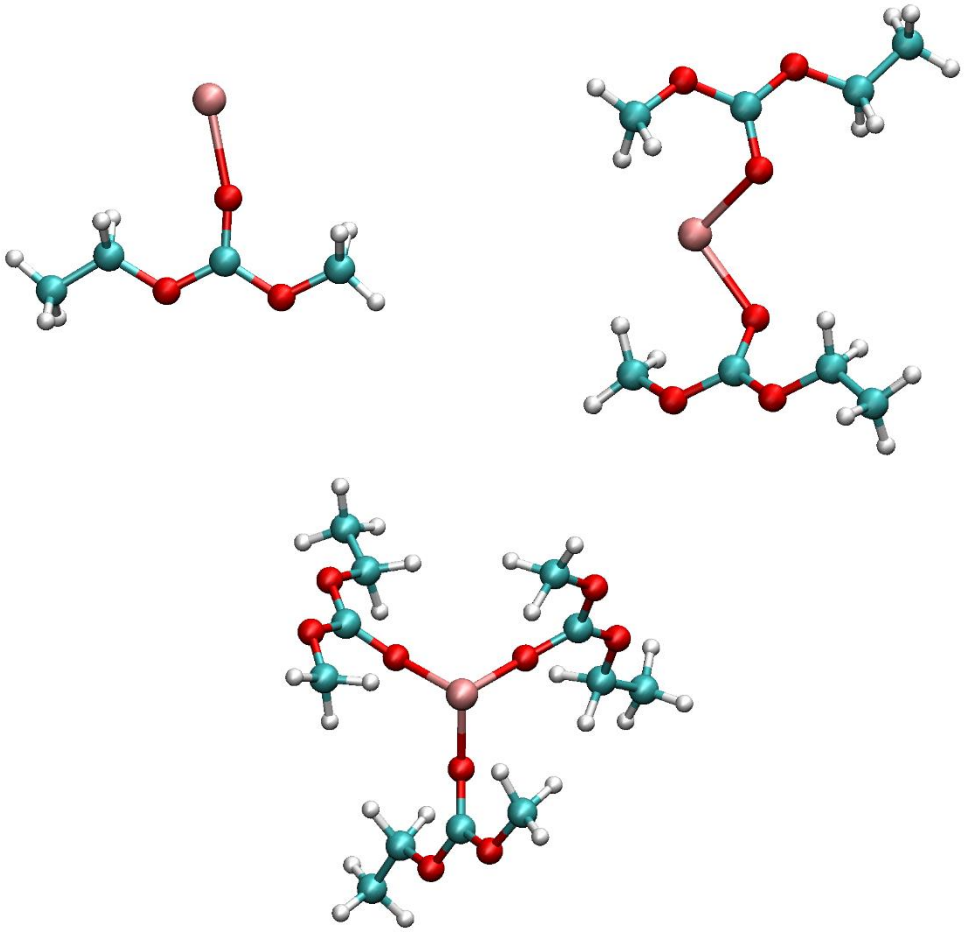

Figure **A-6**: $Li(EMC)_n$ (n = 1 ~ 3) solvation structures

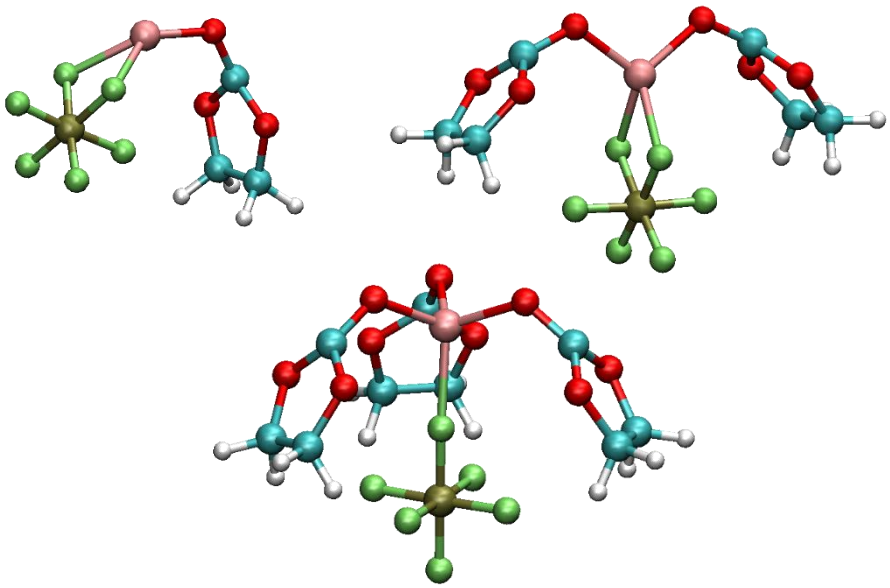

Figure **A-6**: $PF_6Li(EC)_n$ (n = 1 ~ 3) solvation structures. Atom color scheme: C: cyan, H: white, O: red, Li: pink, P: tan and F: lime.

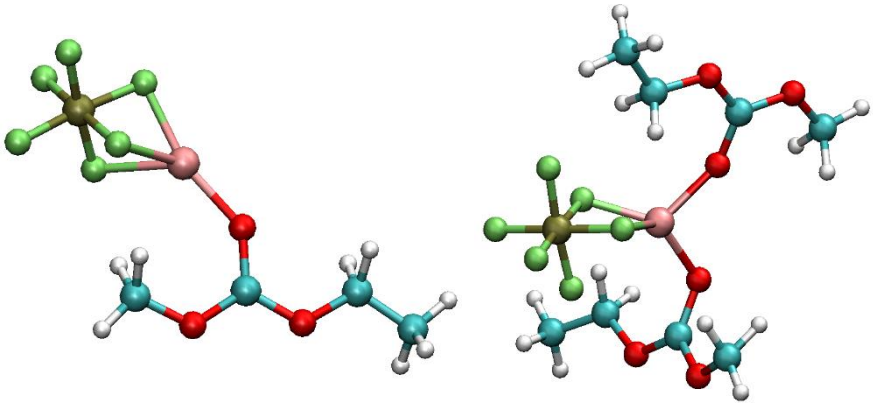

Figure **A-7**: $PF_6Li(EMC)_n$ (n = 1 ~ 2) solvation structures.

References

[1] B. G. Pollet, I. Staffell, and J. L. Shang, “Current status of hybrid, battery and fuel cell electric vehicles: From electrochemistry to market prospects,” *Electrochim. Acta*, vol. 84, pp. 235–249, 2012.

[2] M. R. Palacín and A. de Guibert, “Why do batteries fail?,” *Science (80-.).*, vol. 351, no. 6273, p. 1253292, Feb. 2016.

[3] J. M. Tarascon and M. Armand, “Issues and challenges facing rechargeable lithium batteries,” *Nature*, vol. 414, no. 6861, pp. 359–367, 2001.

[4] E. Peled, “The electrochemical behavior of alkali and alkaline earth metals in nonaqueous battery systems—the solid electrolyte interphase model,” *J. Electrochem. Soc.*, vol. 126, no. 12, pp. 2047–2051, 1979.

[5] C. Daniel and J. O. Besenhard, *Handbook of Battery Materials*. John Wiley & Sons, 2013.

[6] K. MIZUSHIMA, P. C. JONES, P. J. WISEMAN, and J. B. GOODENOUGH, “Lixcoo2 (O Less-Than X Less-Than-or-Equal-To 1) - a New Cathode Material for Batteries of High-Energy Density,” *Solid State Ionics*, vol. 15, no. 6, pp. 783–789, 1980.

[7] M. Lazzari and B. Scrosati, “A cyclable lithium organic electrolyte cell based on two intercalation electrodes,” *J. Electrochem. Soc.*, vol. 127, no. 3, pp. 773–774, 1980.

[8] D. W. Murphy, F. J. Di Salvo, J. N. Carides, and J. V Waszczak, “Topochemical Reactions of Rutile Related Structures with Lithium,” *Mater. Res. Bull.*, vol. 13, no. 12, pp. 1395–1402, 1978.

[9] T. Horiba, “Lithium-ion battery systems,” *Proc. IEEE*, vol. 102, no. 6, pp. 939–950, 2014.

[10] Y. Liang *et al.*, “A review of rechargeable batteries for portable electronic devices,” *InfoMat*, vol. 1, no. 1, pp. 6–32, 2019.

[11] N. Nitta, F. Wu, J. T. Lee, and G. Yushin, “Li-ion battery materials: present and future,” *Mater. today*, vol. 18, no. 5, pp. 252–264, 2015.

[12] K. S. Novoselov *et al.*, “Electric field effect in atomically thin carbon films,” *Science (80-.).*, vol. 306, no. 5696, pp. 666–669, 2004.

[13] K. S. Novoselov *et al.*, “Two-dimensional atomic crystals,” *Proc. Natl. Acad. Sci.*, vol. 102, no. 30, pp. 10451–10453, 2005.

[14] P. Lian, X. Zhu, S. Liang, Z. Li, W. Yang, and H. Wang, “Large reversible capacity of high quality graphene sheets as an anode material for lithium-ion batteries,” *Electrochim. Acta*, vol. 55, no. 12, pp. 3909–3914, 2010.

[15] Z.-S. Wu, W. Ren, L. Xu, F. Li, and H.-M. Cheng, “Doped graphene sheets as anode materials with superhigh rate and large capacity for lithium ion batteries,” *ACS Nano*, vol. 5, no. 7, pp. 5463–5471, 2011.

[16] J. Hassoun *et al.*, “An advanced lithium-ion battery based on a graphene anode and a lithium iron phosphate cathode,” *Nano Lett.*, vol. 14, no. 8, pp. 4901–4906, 2014.

[17] C. Lee, X. Wei, J. W. Kysar, and J. Hone, “Measurement of the elastic properties and intrinsic strength of monolayer graphene,” *Science (80-.).*, vol. 321, no. 5887, pp. 385–388, 2008.

[18] S. Deng and V. Berry, “Wrinkled, rippled and crumpled graphene: an overview of formation mechanism, electronic properties, and applications,” *Mater. Today*, vol. 19, no. 4, pp. 197–212, 2016.

[19] N. Levy *et al.*, “Strain-induced pseudo–magnetic fields greater than 300 tesla in graphene nanobubbles,” *Science (80-.).*, vol. 329, no. 5991, pp. 544–547, 2010.

[20] A. Du Pasquier, I. Plitz, S. Menocal, and G. Amatucci, “A Comparative Study of Li-Ion Battery, Supercapacitor and Nonaqueous Asymmetric Hybrid Devices for Automotive Applications,” *J. Power Sources*, vol. 115, no. 1, pp. 171–178, 2003.

[21] J.-K. Park, *Principles and applications of lithium secondary batteries*. John Wiley & Sons, 2012.

[22] Z. Deng, Y. Mo, and S. P. Ong, "Computational studies of solid-state alkali conduction in rechargeable alkali-ion batteries," *NPG Asia Mater.*, vol. 8, no. 3, pp. e254–e254, 2016.

[23] M. M. Thackeray, L. A. De Picciotto, A. De Kock, P. J. Johnson, V. A. Nicholas, and K. T. Adendorff, "Spinel electrodes for lithium batteries—a review," *J. Power Sources*, vol. 21, no. 1, pp. 1–8, 1987.

[24] K. Leung, "First-principles modeling of the initial stages of organic solvent decomposition on LixMn2O4(100) surfaces," *J. Phys. Chem. C*, vol. 116, no. 18, pp. 9852–9861, 2012.

[25] M. M. Islam *et al.*, "ReaxFF molecular dynamics simulations on lithiated sulfur cathode materials," *Phys. Chem. Chem. Phys.*, vol. 17, no. 5, pp. 3383–3393, 2015.

[26] S. Reddivari, C. Lastoskie, R. Wu, and J. Zhang, "Chemical composition and formation mechanisms in the cathode-electrolyte interface layer of lithium manganese oxide batteries from reactive force field (ReaxFF) based molecular dynamics," *Front. Energy*, vol. 11, no. 3, pp. 365–373, 2017.

[27] Y.-K. Sun, C. S. Yoon, and I.-H. Oh, "Surface structural change of ZnO-coated LiNi0. 5Mn1. 5O4 spinel as 5 V cathode materials at elevated temperatures," *Electrochim. Acta*, vol. 48, no. 5, pp. 503–506, 2003.

[28] T. Kakuda, K. Uematsu, K. Toda, and M. Sato, "Electrochemical performance of Al-doped LiMn2O4 prepared by different methods in solid-state reaction," *J. Power Sources*, vol. 167, no. 2, pp. 499–503, 2007.

[29] Z. Chen and K. Amine, "Capacity Fade of Li1+ x Mn2− x O4-Based Lithium-Ion Cells," *J. Electrochem. Soc.*, vol. 153, no. 2, pp. A316–A320, 2006.

[30] D. Liu and G. Cao, "Engineering nanostructured electrodes and fabrication of film electrodes for efficient lithium ion intercalation," *Energy Environ. Sci.*, vol. 3, no. 9, pp.

1218–1237, 2010.

[31] K. Xu, “Nonaqueous liquid electrolytes for lithium-based rechargeable batteries,” *Chem. Rev.*, vol. 104, no. 10, pp. 4303–4418, 2004.

[32] M. T. Ong, O. Verners, E. W. Draeger, A. C. T. Van Duin, V. Lordi, and J. E. Pask, “Lithium ion solvation and diffusion in bulk organic electrolytes from first-principles and classical reactive molecular dynamics,” *J. Phys. Chem. B*, vol. 119, no. 4, pp. 1535–1545, 2015.

[33] M. Broussely, P. Biensan, and B. Simon, “Lithium insertion into host materials: the key to success for Li ion batteries,” *Electrochim. Acta*, vol. 45, no. 1–2, pp. 3–22, 1999.

[34] T. Tanaka, K. Ohta, and N. Arai, “Year 2000 R&D status of large-scale lithium ion secondary batteries in the national project of Japan,” *J. Power Sources*, vol. 97–98, pp. 2–6, 2001.

[35] N. Terada *et al.*, “Development of lithium batteries for energy storage and EV applications,” *J. Power Sources*, vol. 100, no. 1–2, pp. 80–92, 2001.

[36] D. Aurbach *et al.*, “Design of electrolyte solutions for Li and Li-ion batteries: a review,” *Electrochim. Acta*, vol. 50, no. 2–3, pp. 247–254, 2004.

[37] S. A. Delp, O. Borodin, M. Olguin, C. G. Eisner, J. L. Allen, and T. R. Jow, “Importance of reduction and oxidation stability of high voltage electrolytes and additives,” *Electrochim. Acta*, vol. 209, pp. 498–510, 2016.

[38] Z. Li, “Molecular Dynamics Simulation Studies of Ionic Liquids Electrolytes for Lithium Ion Batteries.” Department of Materials Science and Engineering, University of Utah, 2012.

[39] X.-G. Sun and C. A. Angell, “New sulfone electrolytes for rechargeable lithium batteries.: Part I. Oligoether-containing sulfones,” *Electrochem. commun.*, vol. 7, no. 3, pp. 261–266, 2005.

[40] E. Markervich, G. Salitra, M. D. Levi, and D. Aurbach, “Capacity fading of lithiated graphite electrodes studied by a combination of electroanalytical methods, Raman spectroscopy and SEM,” *J. Power Sources*, vol. 146, no. 1–2, pp. 146–150, 2005.

[41] D. Aurbach, “Review of selected electrode–solution interactions which determine the performance of Li and Li ion batteries,” *J. Power Sources*, vol. 89, no. 2, pp. 206–218, 2000.

[42] D. Aurbach *et al.*, “New insights into the interactions between electrode materials and electrolyte solutions for advanced nonaqueous batteries,” *J. Power Sources*, vol. 81–82, pp. 95–111, 1999.

[43] G. Ferguson and L. A. Curtiss, “Atomic-level modeling of organic electrolytes in lithium-ion batteries,” in *Applications of Molecular Modeling to Challenges in Clean Energy*, American Chemical Society, 2013, pp. 217–233.

[44] K. Xu and A. von Cresce, “Interfacing electrolytes with electrodes in Li ion batteries,” *J. Mater. Chem.*, vol. 21, no. 27, pp. 9849–9864, 2011.

[45] M. Tang, K. Miyazaki, T. Abe, and J. Newman, “Effect of graphite orientation and lithium salt on electronic passivation of highly oriented pyrolytic graphite,” *J. Electrochem. Soc.*, vol. 159, no. 5, pp. A634–A641, 2012.

[46] N. Kumar, K. Leung, and D. J. Siegel, “Crystal Surface and State of Charge Dependencies of Electrolyte Decomposition on LiMn2O4 Cathode,” *J. Electrochem. Soc.*, vol. 161, no. 8, pp. E3059–E3065, 2014.

[47] J. O. Besenhard, M. Winter, J. Yang, and W. Biberacher, “Filming mechanism of lithium-carbon anodes in organic and inorganic electrolytes,” *J. Power Sources*, vol. 54, no. 2, pp. 228–231, 1995.

[48] M. Winter and J. O. Besenhard, “Electrochemical lithiation of tin and tin-based intermetallics and composites,” *Electrochim. Acta*, vol. 45, no. 1–2, pp. 31–50, 1999.

[49] D. Aurbach, M. D. Levi, E. Levi, and A. Schechter, “Failure and stabilization mechanisms of graphite electrodes,” *J. Phys. Chem. B*, vol. 101, no. 12, pp. 2195–2206, 1997.

[50] A. Buttler and H. Spliethoff, “Current status of water electrolysis for energy storage, grid balancing and sector coupling via power-to-gas and power-to-liquids: A review,” *Renew. Sustain. Energy Rev.*, vol. 82, pp. 2440–2454, 2018.

[51] M. Carmo and D. Stolten, “Energy storage using hydrogen produced from excess renewable electricity: Power to hydrogen,” in *Science and Engineering of Hydrogen-Based Energy Technologies*, Elsevier, 2019, pp. 165–199.

[52] S. S. Kumar and V. Himabindu, “Hydrogen production by PEM water electrolysis–A review,” *Mater. Sci. Energy Technol.*, vol. 2, no. 3, pp. 442–454, 2019.

[53] Z. W. Seh, J. Kibsgaard, C. F. Dickens, I. B. Chorkendorff, J. K. Nørskov, and T. F. Jaramillo, “Combining theory and experiment in electrocatalysis: Insights into materials design,” *Science (80-.).*, vol. 355, no. 6321, 2017.

[54] S. Maheshwari, Y. Li, N. Agrawal, and M. J. Janik, “Chapter Three - Density functional theory models for electrocatalytic reactions,” vol. 63, C. B. T.-A. in C. Song, Ed. Academic Press, 2018, pp. 117–167.

[55] C. Wulf, J. Linssen, and P. Zapp, “Power-to-Gas—Concepts, Demonstration, and Prospects,” in *Hydrogen Supply Chains*, Elsevier, 2018, pp. 309–345.

[56] K. Leung and J. L. Budzien, “Ab initio molecular dynamics simulations of the initial stages of solid–electrolyte interphase formation on lithium ion battery graphitic anodes,” *Phys. Chem. Chem. Phys.*, vol. 12, no. 25, pp. 6583–6586, 2010.

[57] P. Ganesh, P. R. C. Kent, and D. Jiang, “Solid–electrolyte interphase formation and electrolyte reduction at Li-ion battery graphite anodes: Insights from first-principles molecular dynamics,” *J. Phys. Chem. C*, vol. 116, no. 46, pp. 24476–24481, 2012.

[58] P. Ganesh, D. Jiang, and P. R. C. Kent, “Accurate static and dynamic properties of liquid

electrolytes for Li-ion batteries from ab initio molecular dynamics," *J. Phys. Chem. B*, vol. 115, no. 12, pp. 3085–3090, 2011.

[59] J. Yu, P. B. Balbuena, J. Budzien, and K. Leung, "Hybrid DFT functional-based static and molecular dynamics studies of excess electron in liquid ethylene carbonate," *J. Electrochem. Soc.*, vol. 158, no. 4, pp. A400–A410, 2011.

[60] K. Leung *et al.*, "Using atomic layer deposition to hinder solvent decomposition in lithium ion batteries: first-principles modeling and experimental studies," *J. Am. Chem. Soc.*, vol. 133, no. 37, pp. 14741–14754, 2011.

[61] K. Leung, "Two-electron reduction of ethylene carbonate: A quantum chemistry re-examination of mechanisms," *Chem. Phys. Lett.*, vol. 568, pp. 1–8, 2013.

[62] K. Leung, "Electronic structure modeling of electrochemical reactions at electrode/electrolyte interfaces in lithium ion batteries," *J. Phys. Chem. C*, vol. 117, no. 4, pp. 1539–1547, 2012.

[63] A. C. T. Van Duin, S. Dasgupta, F. Lorant, and W. A. Goddard, "ReaxFF: a reactive force field for hydrocarbons," *J. Phys. Chem. A*, vol. 105, no. 41, pp. 9396–9409, 2001.

[64] M. M. Islam, V. S. Bryantsev, and A. C. T. van Duin, "ReaxFF Reactive Force Field Simulations on the Influence of Teflon on Electrolyte Decomposition during Li/SWCNT Anode Discharge in Lithium-Sulfur Batteries," *J. Electrochem. Soc.*, vol. 161, no. 8, pp. E3009–E3014, 2014.

[65] M. M. Islam, G. Kolesov, T. Verstraelen, E. Kaxiras, and A. C. T. Van Duin, "EReaxFF: A Pseudoclassical Treatment of Explicit Electrons within Reactive Force Field Simulations," *J. Chem. Theory Comput.*, vol. 12, no. 8, pp. 3463–3472, 2016.

[66] M. M. Islam and A. C. T. Van Duin, "Reductive Decomposition Reactions of Ethylene Carbonate by Explicit Electron Transfer from Lithium: An eReaxFF Molecular Dynamics Study," *J. Phys. Chem. C*, vol. 120, no. 48, pp. 27128–27134, 2016.

[67] D. W. Brenner, “Empirical potential for hydrocarbons for use in simulating the chemical vapor deposition of diamond films,” *Phys. Rev. B*, vol. 42, no. 15, p. 9458, 1990.

[68] S. J. Stuart, A. B. Tutein, and J. A. Harrison, “A reactive potential for hydrocarbons with intermolecular interactions,” *J. Chem. Phys.*, vol. 112, no. 14, pp. 6472–6486, 2000.

[69] J. Tersoff, “New empirical approach for the structure and energy of covalent systems,” *Phys. Rev. B*, vol. 37, no. 12, p. 6991, 1988.

[70] A. C. T. Van Duin, A. Strachan, S. Stewman, Q. Zhang, X. Xu, and W. A. Goddard, “ReaxFFSiO reactive force field for silicon and silicon oxide systems,” *J. Phys. Chem. A*, vol. 107, no. 19, pp. 3803–3811, 2003.

[71] W. J. Mortier, S. K. Ghosh, and S. Shankar, “Electronegativity-equalization method for the calculation of atomic charges in molecules,” *J. Am. Chem. Soc.*, vol. 108, no. 15, pp. 4315–4320, 1986.

[72] T. Verstraelen, P. W. Ayers, V. Van Speybroeck, and M. Waroquier, “ACKS2: Atom-condensed Kohn-Sham DFT approximated to second order,” *J. Chem. Phys.*, vol. 138, no. 7, p. 74108, 2013.

[73] K. Chenoweth, A. C. T. Van Duin, and W. A. Goddard, “ReaxFF reactive force field for molecular dynamics simulations of hydrocarbon oxidation,” *J. Phys. Chem. A*, vol. 112, no. 5, pp. 1040–1053, 2008.

[74] A. C. T. Van Duin, J. M. A. Baas, and B. Van De Graaf, “Delft molecular mechanics: a new approach to hydrocarbon force fields. Inclusion of a geometry-dependent charge calculation,” *J. Chem. Soc. Faraday Trans.*, vol. 90, no. 19, pp. 2881–2895, 1994.

[75] J. T. Su and W. A. Goddard III, “The dynamics of highly excited electronic systems: applications of the electron force field,” *J. Chem. Phys.*, vol. 131, no. 24, p. 244501, 2009.

[76] J. T. Su and W. A. Goddard III, “Excited electron dynamics modeling of warm dense matter,” *Phys. Rev. Lett.*, vol. 99, no. 18, p. 185003, 2007.

[77] S. Kale, J. Herzfeld, S. Dai, and M. Blank, “Lewis-inspired representation of dissociable water in clusters and Grotthuss chains,” *J. Biol. Phys.*, vol. 38, no. 1, pp. 49–59, 2012.

[78] S. Kale and J. Herzfeld, “Pairwise long-range compensation for strongly ionic systems,” *J. Chem. Theory Comput.*, vol. 7, no. 11, pp. 3620–3624, 2011.

[79] S. Ekesan and J. Herzfeld, “Pointillist rendering of electron charge and spin density suffices to replicate trends in atomic properties,” *Proc. R. Soc. A Math. Phys. Eng. Sci.*, vol. 471, no. 2181, p. 20150370, 2015.

[80] P. T. Mikulski, M. T. Knippenberg, and J. A. Harrison, “Merging bond-order potentials with charge equilibration.” AIP, 2009.

[81] R. A. Nistor, J. G. Polihronov, M. H. Müser, and N. J. Mosey, “A generalization of the charge equilibration method for nonmetallic materials,” *J. Chem. Phys.*, vol. 125, no. 9, p. 94108, 2006.

[82] M. T. Knippenberg, P. T. Mikulski, K. E. Ryan, S. J. Stuart, G. Gao, and J. A. Harrison, “Bond-order potentials with split-charge equilibration: Application to C-, H-, and O-containing systems,” *J. Chem. Phys.*, vol. 136, no. 16, p. 164701, 2012.

[83] “eReaxff: classical treatment of the explicit electron.” [Online]. Available: https://www.scm.com/doc/ReaxFF/eReaxFF.html.

[84] J. Cioslowski and B. B. Stefanov, “Electron flow and electronegativity equalization in the process of bond formation,” *J. Chem. Phys.*, vol. 99, no. 7, pp. 5151–5162, 1993.

[85] G. Lee Warren, J. E. Davis, and S. Patel, “Origin and control of superlinear polarizability scaling in chemical potential equalization methods,” *J. Chem. Phys.*, vol. 128, no. 14, p. 144110, 2008.

[86] R. A. Nistor and M. H. Müser, “Dielectric properties of solids in the regular and split-charge equilibration formalisms,” *Phys. Rev. B*, vol. 79, no. 10, p. 104303, 2009.

[87] J. N. Louwen and E. T. C. Vogt, “Semi-empirical atomic charges for use in computational

chemistry of molecular sieves," *J. Mol. Catal. A Chem.*, vol. 134, no. 1–3, pp. 63–77, 1998.

[88] K. Ganeshan, M. J. Hossain, and A. C. T. van Duin, "Multiply accelerated ReaxFF molecular dynamics: coupling parallel replica dynamics with collective variable hyper dynamics," *Mol. Simul.*, vol. 45, no. 14–15, pp. 1265–1272, Aug. 2019.

[89] K. Ohno, K. Esfarjani, and Y. Kawazoe, *Computational materials science: from ab initio to Monte Carlo methods*. Springer, 2018.

[90] K. Chenoweth, A. C. T. Van Duin, and W. A. Goddard, "ReaxFF reactive force field for molecular dynamics simulations of hydrocarbon oxidation," *J. Phys. Chem. A*, vol. 112, no. 5, pp. 1040–1053, 2008.

[91] T. R. Shan, B. D. Devine, T. W. Kemper, S. B. Sinnott, and S. R. Phillpot, "Charge-optimized many-body potential for the hafnium/hafnium oxide system," *Phys. Rev. B - Condens. Matter Mater. Phys.*, vol. 81, no. 12, pp. 1–12, 2010.

[92] S. J. Stuart, A. B. Tutein, and J. A. Harrison, "A reactive potential for hydrocarbons with intermolecular interactions," *J. Chem. Phys.*, vol. 112, no. 14, pp. 6472–6486, 2000.

[93] M. I. Baskes, "Application of the Embedded-Atom Method to Covalent Materials: A Semiempirical Potential for Silicon," *Phys. Rev. Lett.*, vol. 59, no. 23, pp. 2666–2669, 1987.

[94] D. Frenkel, B. Smit, J. Tobochnik, S. R. McKay, and W. Christian, "Understanding Molecular Simulation," *Comput. Phys.*, vol. 11, no. 4, p. 351, 1997.

[95] S. B. Kylasa, H. M. Aktulga, and A. Y. Grama, "PuReMD-GPU: A reactive molecular dynamics simulation package for GPUs," *J. Comput. Phys.*, vol. 272, pp. 343–359, 2014.

[96] M. Zheng, X. Li, and L. Guo, "Algorithms of GPU-enabled reactive force field (ReaxFF) molecular dynamics," *J. Mol. Graph. Model.*, vol. 41, pp. 1–11, 2013.

[97] A. F. Voter, "Parallel replica method for dynamics of infrequent events," *Phys. Rev. B -*

Condens. Matter Mater. Phys., vol. 57, no. 22, pp. R13985–R13988, 1998.

[98] K. L. Joshi, S. Raman, and A. C. T. Van Duin, "Connectivity-based parallel replica dynamics for chemically reactive systems: From femtoseconds to microseconds," *J. Phys. Chem. Lett.*, vol. 4, no. 21, pp. 3792–3797, 2013.

[99] C. Le Bris, T. Lelièvre, M. Luskin, and D. Perez, "A mathematical formalization of the parallel replica dynamics," *Monte Carlo Methods Appl.*, vol. 18, no. 2, pp. 1–21, Jan. 2012.

[100] T. Lelièvre, "Accelerated dynamics: Mathematical foundations and algorithmic improvements," *Eur. Phys. J. Spec. Top.*, vol. 224, no. 12, pp. 2429–2444, 2015.

[101] A. F. Voter and M. R. Sørensen, "Accelerating Atomistic Simulations of Defect Dynamics: Hyperdynamics, Parallel Replica Dynamics, and Temperature-Accelerated Dynamics," *MRS Proc.*, vol. 538, p. 427, Jan. 1998.

[102] A. F. Voter, "Hyperdynamics: Accelerated Molecular Dynamics of Infrequent Events," *Phys. Rev. Lett.*, vol. 78, no. 20, pp. 3908–3911, May 1997.

[103] A. Laio and M. Parrinello, "Escaping free-energy minima," *Proc. Natl. Acad. Sci.*, vol. 99, no. 20, pp. 12562–12566, 2002.

[104] K. M. Bal and E. C. Neyts, "Merging Metadynamics into Hyperdynamics: Accelerated Molecular Simulations Reaching Time Scales from Microseconds to Seconds," *J. Chem. Theory Comput.*, vol. 11, no. 10, pp. 4545–4554, 2015.

[105] E. C. Neyts, Y. Shibuta, A. C. T. Van Duin, and A. Bogaerts, "Catalyzed growth of carbon nanotube with definable chirality by hybrid molecular dynamics-force biased monte carlo simulations," *ACS Nano*, vol. 4, no. 11, pp. 6665–6672, 2010.

[106] T. P. Senftle, A. C. T. Van Duin, and M. J. Janik, "Determining in situ phases of a nanoparticle catalyst via grand canonical Monte Carlo simulations with the ReaxFF potential," *Catal. Commun.*, vol. 52, pp. 72–77, 2014.

[107] T. Cheng, A. Jaramillo-Botero, W. A. Goddard, and H. Sun, “Adaptive accelerated ReaxFF reactive dynamics with validation from simulating hydrogen combustion,” *J. Am. Chem. Soc.*, vol. 136, no. 26, pp. 9434–9442, 2014.

[108] A. Vashisth, C. Ashraf, W. Zhang, C. E. Bakis, and A. C. T. Van Duin, “Accelerated ReaxFF Simulations for Describing the Reactive Cross-Linking of Polymers,” *J. Phys. Chem. A*, vol. 122, no. 32, pp. 6633–6642, 2018.

[109] R. J. Zamora, D. Perez, E. Martinez, B. P. Uberuaga, and A. F. Voter, “Accelerated Molecular Dynamics Methods in a Massively Parallel World,” in *Handbook of Materials Modeling*, Cham: Springer International Publishing, 2018, pp. 1–28.

[110] K. M. Bal and E. C. Neyts, “Direct observation of realistic-temperature fuel combustion mechanisms in atomistic simulations,” *Chem. Sci.*, vol. 7, no. 8, pp. 5280–5286, 2016.

[111] A. F. Voter and T. C. Germann, “Accelerating the Dynamics of Infrequent Events: Combining Hyperdynamics and Parallel Replica Dynamics to Treat Epitaxial Layer Growth,” *MRS Proc.*, vol. 528, p. 221, Jan. 1998.

[112] A. F. Voter, F. Montalenti, and T. C. Germann, “Extending the Time Scale in Atomistic Simulation of Materials,” *Annu. Rev. Mater. Res.*, vol. 32, no. 1, pp. 321–346, 2002.

[113] C. Ashraf, S. Shabnam, A. Jain, Y. Xuan, and A. C. T. van Duin, “Pyrolysis of binary fuel mixtures at supercritical conditions: A ReaxFF molecular dynamics study,” *Fuel*, vol. 235, no. July 2018, pp. 194–207, 2019.

[114] M. M. Islam, G. Kolesov, T. Verstraelen, E. Kaxiras, and A. C. T. Van Duin, “EReaxFF: A Pseudoclassical Treatment of Explicit Electrons within Reactive Force Field Simulations,” *J. Chem. Theory Comput.*, vol. 12, no. 8, pp. 3463–3472, 2016.

[115] M. J. Hossain, G. Pawar, B. Liaw, K. L. Gering, E. J. Dufek, and A. C. T. van Duin, “Lithium-electrolyte solvation and reaction in the electrolyte of a lithium ion battery: A ReaxFF reactive force field study,” *J. Chem. Phys.*, vol. 152, no. 18, p. 184301, May

2020.

[116] M. Winter, “The solid electrolyte interphase–the most important and the least understood solid electrolyte in rechargeable Li batteries,” *Zeitschrift für Phys. Chemie*, vol. 223, no. 10–11, pp. 1395–1406, 2009.

[117] P. Verma, P. Maire, and P. Novák, “A review of the features and analyses of the solid electrolyte interphase in Li-ion batteries,” *Electrochim. Acta*, vol. 55, no. 22, pp. 6332–6341, 2010.

[118] M. Armand and J.-M. Tarascon, “Building better batteries,” *Nature*, vol. 451, no. 7179, pp. 652–657, 2008.

[119] E. Cazzanelli, P. Mustarelli, F. Benevelli, G. B. Appetecchi, and F. Croce, “Raman and NMR analysis of LiClO4 concentrated solutions in ethylene carbonate-propylene carbonate,” *Solid state ionics*, vol. 86–88, pp. 379–384, 1996.

[120] M. Morita, Y. Asai, N. Yoshimoto, and M. Ishikawa, “A Raman spectroscopic study of organic electrolyte solutions based on binary solvent systems of ethylene carbonate with low viscosity solvents which dissolve different lithium salts,” *J. Chem. Soc. Faraday Trans.*, vol. 94, no. 23, pp. 3451–3456, 1998.

[121] Y. Kameda *et al.*, “Solvation structure of Li+ in concentrated LiPF6− propylene carbonate solutions,” *J. Phys. Chem. B*, vol. 111, no. 22, pp. 6104–6109, 2007.

[122] O. Borodin and G. D. Smith, “LiTFSI structure and transport in ethylene carbonate from molecular dynamics simulations,” *J. Phys. Chem. B*, vol. 110, no. 10, pp. 4971–4977, 2006.

[123] J.-C. Soetens, C. Millot, and B. Maigret, “Molecular dynamics simulation of Li+ BF4-in ethylene carbonate, propylene carbonate, and dimethyl carbonate solvents,” *J. Phys. Chem. A*, vol. 102, no. 7, pp. 1055–1061, 1998.

[124] M. Masia, M. Probst, and R. Rey, “Ethylene Carbonate− Li+: A Theoretical Study of

Structural and Vibrational Properties in Gas and Liquid Phases," *J. Phys. Chem. B*, vol. 108, no. 6, pp. 2016–2027, 2004.

[125] K. Tasaki, A. Goldberg, and M. Winter, "On the difference in cycling behaviors of lithium-ion battery cell between the ethylene carbonate-and propylene carbonate-based electrolytes," *Electrochim. Acta*, vol. 56, no. 28, pp. 10424–10435, 2011.

[126] M. D. Bhatt, M. Cho, and K. Cho, "Density functional theory calculations and ab initio molecular dynamics simulations for diffusion of Li+ within liquid ethylene carbonate," *Model. Simul. Mater. Sci. Eng.*, vol. 20, no. 6, p. 65004, 2012.

[127] O. Borodin and G. D. Smith, "Quantum chemistry and molecular dynamics simulation study of dimethyl carbonate: ethylene carbonate electrolytes doped with LiPF6," *J. Phys. Chem. B*, vol. 113, no. 6, pp. 1763–1776, 2009.

[128] A. Wang, S. Kadam, H. Li, S. Shi, and Y. Qi, "Review on modeling of the anode solid electrolyte interphase (SEI) for lithium-ion batteries," *npj Comput. Mater.*, vol. 4, no. 1, pp. 1–78, 2018.

[129] Y. Wang, S. Nakamura, M. Ue, and P. B. Balbuena, "Theoretical studies to understand surface chemistry on carbon anodes for lithium-ion batteries: reduction mechanisms of ethylene carbonate," *J. Am. Chem. Soc.*, vol. 123, no. 47, pp. 11708–11718, 2001.

[130] D. Bedrov, G. D. Smith, and A. C. T. Van Duin, "Reactions of singly-reduced ethylene carbonate in lithium battery electrolytes: a molecular dynamics simulation study using the ReaxFF," *J. Phys. Chem. A*, vol. 116, no. 11, pp. 2978–2985, 2012.

[131] K. Tasaki, "Solvent decompositions and physical properties of decomposition compounds in Li-ion battery electrolytes studied by DFT calculations and molecular dynamics simulations," *J. Phys. Chem. B*, vol. 109, no. 7, pp. 2920–2933, 2005.

[132] K. Ushirogata, K. Sodeyama, Y. Okuno, and Y. Tateyama, "Additive effect on reductive decomposition and binding of carbonate-based solvent toward solid electrolyte interphase

formation in lithium-ion battery," *J. Am. Chem. Soc.*, vol. 135, no. 32, pp. 11967–11974, 2013.

[133] C. Ashraf and A. C. T. Van Duin, "Extension of the ReaxFF combustion force field toward syngas combustion and initial oxidation kinetics," *J. Phys. Chem. A*, vol. 121, no. 5, pp. 1051–1068, 2017.

[134] X. Wang *et al.*, "Glassy Li Metal Anode for High-Performance Rechargeable Li Batteries," *arXiv Prepr. arXiv1910.11513*, 2019.

[135] R. Lotfi, D. E. Yilmaz, L. Vlcek, and A. van Duin, "Molecular Dynamics Simulations of MXenes: Ab Initio, Reactive, and Non-reactive Empirical Force Fields," in *2D Metal Carbides and Nitrides (MXenes)*, Springer, 2019, pp. 137–157.

[136] K. Mondal, T. Maitra, A. K. Srivastava, G. Pawar, M. D. McMurtrey, and A. Sharma, "110th Anniversary: Particle Size Effect on Enhanced Graphitization and Electrical Conductivity of Suspended Gold/Carbon Composite Nanofibers," *Ind. Eng. Chem. Res.*, 2020.

[137] D. Akbarian *et al.*, "Atomistic-scale insights into the crosslinking of polyethylene induced by peroxides," *Polymer (Guildf).*, vol. 183, p. 121901, 2019.

[138] G. Pawar, P. Meakin, and H. Huang, "Reactive molecular dynamics simulation of kerogen thermal maturation and cross-linking pathways," *Energy & Fuels*, vol. 31, no. 11, pp. 11601–11614, 2017.

[139] D. Akbarian *et al.*, "Understanding the influence of defects and surface chemistry on ferroelectric switching: a ReaxFF investigation of BaTiO 3," *Phys. Chem. Chem. Phys.*, vol. 21, no. 33, pp. 18240–18249, 2019.

[140] K. M. Bal and E. C. Neyts, "Direct observation of realistic-temperature fuel combustion mechanisms in atomistic simulations," *Chem. Sci.*, vol. 7, no. 8, pp. 5280–5286, 2016.

[141] K. Ganeshan, M. J. Hossain, and A. C. T. van Duin, "Multiply accelerated ReaxFF

molecular dynamics: coupling parallel replica dynamics with collective variable hyper dynamics," *Mol. Simul.*, vol. 45, no. 14–15, pp. 1265–1272, Oct. 2019.

[142] L. L. C. Schrödinger, "Jaguar, version 9.4." Schrödinger LLC, New York, NY, 2016.

[143] S. G. Srinivasan, A. C. T. Van Duin, and P. Ganesh, "Development of a ReaxFF potential for carbon condensed phases and its application to the thermal fragmentation of a large fullerene," *J. Phys. Chem. A*, vol. 119, no. 4, pp. 571–580, 2015.

[144] K. Leung, "Predicting the voltage dependence of interfacial electrochemical processes at lithium-intercalated graphite edge planes," *Phys. Chem. Chem. Phys.*, vol. 17, no. 3, pp. 1637–1643, 2015.

[145] E. R. Logan, E. M. Tonita, K. L. Gering, and J. R. Dahn, "A critical evaluation of the advanced electrolyte model," *J. Electrochem. Soc.*, vol. 165, no. 14, p. A3350, 2018.

[146] S. C. M. ADF2019, "Theoretical Chemistry, Vrije Universiteit, Amsterdam, The Netherlands." 2019.

[147] H. J. C. Berendsen, J. P. M. van Postma, W. F. van Gunsteren, A. DiNola, and J. R. Haak, "Molecular dynamics with coupling to an external bath," *J. Chem. Phys.*, vol. 81, no. 8, pp. 3684–3690, 1984.

[148] H. Dua, J. Deb, D. Paul, and U. Sarkar, "Twin-graphene as a Promising Anode Material for Na-Ion Rechargeable Batteries," *ACS Appl. Nano Mater.*, vol. 4, no. 5, pp. 4912–4918, May 2021.

[149] E. Yoo, J. Kim, E. Hosono, H. Zhou, T. Kudo, and I. Honma, "Large Reversible Li Storage of Graphene Nanosheet Families for Use in Rechargeable Lithium Ion Batteries," *Nano Lett.*, vol. 8, no. 8, pp. 2277–2282, Aug. 2008.

[150] Q. Cheng, Y. Okamoto, N. Tamura, M. Tsuji, S. Maruyama, and Y. Matsuo, "Graphene-Like-Graphite as Fast-Chargeable and High-Capacity Anode Materials for Lithium Ion Batteries," *Sci. Rep.*, vol. 7, no. 1, p. 14782, 2017.

[151] H. Murata *et al.*, “Multilayer Graphene Battery Anodes on Plastic Sheets for Flexible Electronics,” *ACS Appl. Energy Mater.*, vol. 3, no. 9, pp. 8410–8414, Sep. 2020.

[152] M. R. Al Hassan, A. Sen, T. Zaman, and M. S. Mostari, “Emergence of graphene as a promising anode material for rechargeable batteries: a review,” *Mater. Today Chem.*, vol. 11, pp. 225–243, 2019.

[153] M. M. Atabaki and R. Kovacevic, “Graphene composites as anode materials in lithium-ion batteries,” *Electron. Mater. Lett.*, vol. 9, no. 2, pp. 133–153, 2013.

[154] F. Banhart, J. Kotakoski, and A. V Krasheninnikov, “Structural Defects in Graphene,” *ACS Nano*, vol. 5, no. 1, pp. 26–41, Jan. 2011.

[155] M. Raju, P. Ganesh, P. R. C. Kent, and A. C. T. Van Duin, “Reactive force field study of Li/C systems for electrical energy storage,” *J. Chem. Theory Comput.*, vol. 11, no. 5, pp. 2156–2166, 2015.

[156] B. Evangelisti, K. A. Fichthorn, and A. C. T. van Duin, “Development and initial applications of an e-ReaxFF description of Ag nanoclusters,” *J. Chem. Phys.*, vol. 153, no. 10, p. 104106, Sep. 2020.

[157] D. Akbarian, K. Ganeshan, W. H. H. Woodward, J. Moore, and A. C. T. van Duin, “Atomistic-scale insight into the polyethylene electrical breakdown: An eReaxFF molecular dynamics study,” *J. Chem. Phys.*, vol. 154, no. 2, p. 24904, 2021.

[158] X.-B. Wang, C.-F. Ding, and L.-S. Wang, “High resolution photoelectron spectroscopy of C 60−,” *J. Chem. Phys.*, vol. 110, no. 17, pp. 8217–8220, 1999.

[159] M. L. Tiago, P. R. C. Kent, R. Q. Hood, and F. A. Reboredo, “Neutral and charged excitations in carbon fullerenes from first-principles many-body theories,” *J. Chem. Phys.*, vol. 129, no. 8, p. 84311, 2008.

[160] G. Malloci, G. Mulas, G. Cappellini, V. Fiorentini, and I. Porceddu, “Theoretical electron affinities of PAHs and electronic absorption spectra of their mono-anions,” *Astron.*

Astrophys., vol. 432, no. 2, pp. 585–594, 2005.

[161] R. Yan *et al.*, “Determination of graphene work function and graphene-insulator-semiconductor band alignment by internal photoemission spectroscopy,” *Appl. Phys. Lett.*, vol. 101, no. 2, p. 22105, 2012.

[162] K. Bhaskaran-Nair, K. Kowalski, J. Moreno, M. Jarrell, and W. A. Shelton, “Equation of motion coupled cluster methods for electron attachment and ionization potential in fullerenes C60 and C70,” *J. Chem. Phys.*, vol. 141, no. 7, p. 74304, 2014.

[163] J. C. Rienstra-Kiracofe, C. J. Barden, S. T. Brown, and H. F. Schaefer, “Electron affinities of polycyclic aromatic hydrocarbons,” *J. Phys. Chem. A*, vol. 105, no. 3, pp. 524–528, 2001.

[164] N. Driver and P. Jena, “Electron affinity of modified benzene,” *Int. J. Quantum Chem.*, vol. 118, no. 4, p. e25504, 2018.

[165] T. Heinis, S. Chowdhury, and P. Kebarle, “Electron affinities of naphthalene, anthracene and substituted naphthalenes and anthracenes,” *Org. mass Spectrom.*, vol. 28, no. 4, pp. 358–365, 1993.

[166] L. Crocker, T. Wang, and P. Kebarle, “Electron affinities of some polycyclic aromatic hydrocarbons, obtained from electron-transfer equilibria,” *J. Am. Chem. Soc.*, vol. 115, no. 17, pp. 7818–7822, 1993.

[167] G. Chen and R. G. Cooks, “Electron affinities of polycyclic aromatic hydrocarbons determined by the kinetic method,” *J. Mass Spectrom.*, vol. 30, no. 8, pp. 1167–1173, 1995.

[168] G. Chen, R. G. Cookscor, E. Corpuz, and L. T. Scott, “Estimation of the electron affinities of C 60, corannulene, and coronene by using the kinetic method,” *J. Am. Soc. Mass Spectrom.*, vol. 7, no. 7, pp. 619–627, 1996.

[169] R. V Khatymov, M. V Muftakhov, and P. V Shchukin, “Negative ions, molecular electron

affinity and orbital structure of cata-condensed polycyclic aromatic hydrocarbons," *Rapid Commun. Mass Spectrom.*, vol. 31, no. 20, pp. 1729–1741, 2017.

[170] R. Banerjee *et al.*, "Strain modulated superlattices in graphene," *Nano Lett.*, vol. 20, no. 5, pp. 3113–3121, 2020.

[171] R. Li and C. Li, "Chapter One - Photocatalytic Water Splitting on Semiconductor-Based Photocatalysts," vol. 60, C. B. T.-A. in C. Song, Ed. Academic Press, 2017, pp. 1–57.

[172] P. Majumdar, M. K. Bera, D. Pant, and S. Patra, "Enzymatic Electrocatalysis of CO2 Reduction," K. B. T.-E. of I. C. Wandelt, Ed. Oxford: Elsevier, 2018, pp. 577–589.

[173] A. Groß, "Computational Modeling of Electrocatalytic Reactions," K. B. T.-E. of I. C. Wandelt, Ed. Oxford: Elsevier, 2018, pp. 455–465.

[174] Y. Jiao, Y. Zheng, M. Jaroniec, and S. Z. Qiao, "Design of electrocatalysts for oxygen- and hydrogen-involving energy conversion reactions," *Chem. Soc. Rev.*, vol. 44, no. 8, pp. 2060–2086, 2015.

[175] J. D. Benck, T. R. Hellstern, J. Kibsgaard, P. Chakthranont, and T. F. Jaramillo, "Catalyzing the Hydrogen Evolution Reaction (HER) with Molybdenum Sulfide Nanomaterials," *ACS Catal.*, vol. 4, no. 11, pp. 3957–3971, Nov. 2014.

[176] J. Zhu, L. Hu, P. Zhao, L. Y. S. Lee, and K.-Y. Wong, "Recent Advances in Electrocatalytic Hydrogen Evolution Using Nanoparticles," *Chem. Rev.*, vol. 120, no. 2, pp. 851–918, Jan. 2020.

[177] E. Fabbri, D. Pergolesi, S. Licoccia, and E. Traversa, "Does the increase in Y-dopant concentration improve the proton conductivity of BaZr1− xYxO3− δ fuel cell electrolytes?," *Solid State Ionics*, vol. 181, no. 21–22, pp. 1043–1051, 2010.

[178] A. C. T. Van Duin, B. V Merinov, S. S. Jang, and W. A. Goddard, "ReaxFF reactive force field for solid oxide fuel cell systems with application to oxygen ion transport in yttria-stabilized zirconia," *J. Phys. Chem. A*, vol. 112, no. 14, pp. 3133–3140, 2008.

VITA

Md Jamil Hossain

EDUCATION

Doctor of Philosophy in Mechanical Engineering
The Pennsylvania State University, University Park, PA-16802, USA
Graduation: Dec 2021
GPA: **4.00**/4.00

Master of Science in Mechanical Engineering
Bangladesh University of Engineering and Technology (BUET), Dhaka, Bangladesh
Graduation: June 2016
GPA: **4.00**/4.00

Bachelor of Science in Mechanical Engineering
Bangladesh University of Engineering and Technology (BUET), Dhaka, Bangladesh
Graduation: March 2012
GPA: **3.94**/4.00

SELECTED PUBLICATIONS

2021 R. Banerjee, T. Granzier-Nakajima, A. Lele, J. A. Schulze, **M. J. Hossain**, W. Zhu, L. Pabbi, M. Kowalik, A. C. T. van Duin, M. Terrones, and E. W. Hudson, **On the origin of non-classical ripples in draped graphene sheets**. Submitted Manuscript.

2021 I. Leven, H. Hao, S. Tan, X. Guan, K. A. Penrod, D. Akbarian, B. Evangelisti, **M. J. Hossain**, M. M. Islam, J. Koski, S. Moore, H. M. Aktulga, A. C. T. van Duin, T. Head-Gordon, **Recent Advances for Improving the Accuracy, Transferability and Efficiency of Reactive ForceFields** Journal of Chemical Theory and Computation 17 (2021) 3237-3251; doi.org/10.1021/acs.jctc.1c00118

2021 M. Kowalik, **M. J. Hossain**, A. Lele, W. Zhu, R. Banerjee, T. Granzier-Nakajima, M. Terrones, E. W. Hudson, and A. C. T. van Duin, **Atomistic-scale simulations on graphene bending near a copper surface**. Catalysts 11 (2021) 208 :doi.org/10.3390/catal11020208

2020 Y. Gao, D. Wang, Y. K. Shin, Z. Yan, Z. Han, K. Wang, **M. J. Hossain,** S. Shen, A. AlZahrani, A. C. T. van Duin, T. E. Mallouk, and D. Wang, **Stable metal anodes enabled by a labile organic molecule bonded to a reduced graphene oxide aerogel**. Proceedings of the National Academy of Sciences, 117.48 (2020) 30135-30141; doi.org/10.1073/pnas.2001837117

2020 **M. J. Hossain**, G. Pawar, B. Liaw, K. L. Gering, E. J. Dufek and A. C. T. van Duin, **Lithium-electrolyte solvation and reaction in the electrolyte of a lithium ion battery: A ReaxFF reactive force field study**, The Journal of Chemical Physics 152 (2020) 184301; doi.org/10.1063/5.0003333

2019 K. Ganeshan, **M. J. Hossain** and A. C. T. van Duin, **Multiply accelerated ReaxFF molecular dynamics: coupling parallel replica dynamics with collective variable hyper dynamics**, Molecular Simulation 45 (2019), 1265-1272; doi.org/10.1080/08927022.2019.1646911.